CHARACTERIZATION OF BRAIN TISSUE MICROSTRUCTURES WITH DIFFUSION MRI

by

Dan Wu

A dissertation submitted to Johns Hopkins University in conformity with the requirements for the degree of Doctor of Philosophy

Baltimore, Maryland

March, 2015

Abstract

Diffusion MRI is a useful medical imaging tool for noninvasive mapping of the neuroanatomy and brain connectivity. In this dissertation, we worked on developing diffusion MRI techniques to probe brain tissue microstructures from various perspectives.

Spatial resolution of the diffusion MRI is the key to obtain accurate microstructural information. In Chapter 2 and 3, we focused on developing high-resolution *in vivo* diffusion MRI techniques, such as 3D fast imaging sequence and a localized imaging approach using selective excitation RF pulses. We demonstrated the power of the superior resolution in delineating complex microstructures in the live mouse brain. With the high resolution diffusion MRI data, we were able to map the intra-hippocampal connectivity in the mouse brain, which showed remarkable similarity with tracer studies (Chapter 4). Using the localized fast imaging technique, we were the first to achieve in utero diffusion MRI of embryonic mouse brain, which revealed the microstructures in the developing brains and the changes after inflammatory injury (Chapter 5).

The second half of the dissertation explores the restricted water diffusion at varying diffusion times and microstructure scales, using the oscillating gradient spin-echo (OGSE) diffusion MRI. We showed in the live normal mouse brains that unique tissue contrasts can be obtained at different oscillating frequency. We demonstrated in a neonatal mouse model of hypoxia-ischemia, that in the edema brain tissues, diffusion MRI signal changed much faster with oscillating frequency compared to the normal tissue, indicating significant changes in cell size associated with cytotoxic edema (Chapter 6). In the mild injury mice, OGSE showed exquisite sensitivity in detecting subtle injury in the hippocampus, which

may relate to microstructural changes in smaller scales, such as the subcellular organelles (Chapter 7). Finally, we addressed the technical issues of OGSE diffusion MRI, and proposed a new hybrid OGSE sequence with orthogonally placed pulsed and oscillating gradients to suppress the perfusion related pseudo-diffusion (Chapter 8).

In conclusion, we developed *in vivo* high-resolution diffusion techniques, and time-dependent diffusion measurements to characterize brain tissue microstructures in the normal and diseased mouse brains. The knowledge gained from this dissertation study may advance our understanding on microstructural basis of diffusion MRI.

First reader and advisor: Dr. Jiangyang Zhang, Ph.D

Associate Professor of Radiology, Johns Hopkins University School of Medicine

Second reader: Dr. Frances J Northington, MD

Professor of Pediatrics, Johns Hopkins University School of Medicine

Preface

Acknowledgement

First of all, I would like to give my highest gratitude to my advisor Dr. Jiangyang Zhang, who has been an extraordinary advisor and great friend throughout the four years of my PhD life. The continuous and unconditonal supports from him on every step of my way, made me from an absolute beginner to a trained researcher with professional expertise. Not to mention the numerous helps on my research projects, his encouragements and positive attitudes always intriguer my passion in perusing academia, and his consideration on my personal development is well-beyond a research advisor but a life mentor. None of my achievements would ever take place without his guidance and contributions.

I am deeply grateful to my advisor, Dr. Frances Northington, for being extremely encouraging and supportive on my thesis projects, and providing an important bridge between biomedical engineering and the real clinical needs. I sincerely appreciate the mentoring from Dr. Susumu Mori, who has offered many constructing and expertise advices on my thesis study and also supports on my career development. I am very thankful to Dr. Daniel Herzka, who provided me solid training in MR physics as course instructor, and also promoted my research from basic science to clinical applications.

The PhD program at Hopkins BME has provided me tremendous opportunities to collaborate with experts in various fields. I would like to send many thanks to Dr. Irina Burd from Department of Gynecology and Obstetrics, Dr. Lee Martin from Department Pathology and Neuroscience, Dr. Peter van Zijl and Dr. Jiadi Xu from the Kennedy Krieger Institute. It has been my greatest honor and pleasure to work with them and publish our

works. I am also very grateful to my Graduate Board Committee, Dr. Steve Hsiao from Department of Neuroscience and Dr. Nam Lee from Department of Applied Mathematics, who have willingly provided me valuable advices both in and outside the course materials.

I am heartily thankful my labmates, Zhipeng Hou, Qiang Li, Yajing Zhang, Aggy Djamanakova, Shoko Yashida, and colleagues from the Kennedy Krieger Institute: Kazi Akhter, Guanshu Liu, Qinqin, Xiaolei Song, Ying Cheng, Ann Choi, Haifeng Zeng, and many others. I really appreciate your contribution and supports, both technically and mentally, throughout these years. You have made my PhD life enjoyable and productive.

I would like to share my happiness with my friends in and outside Hopkins, who have helped me through every weary and frustrating moments during my study in the US, especially my fiancé, Yi Zhang, with whom I shared four years of happy memory and grew stronger together. Finally, I want to express special thanks to my dearest parents in China. Their supports, advices, and unconditional love have always been the internal impetus in me.

Despite all the help and contributions from others, I am solely responsible for the content in this dissertation. I apologize for any possible errors or omissions.

Thesis Committee

Dr. Jiangyang Zhang

Associate Professor, Department of Radiology

Johns Hopkins University School of Medicine

Dr. Frances J Northington

Professor, Department of Pediatrics

Johns Hopkins University School of Medicine

Dr. Susumu Mori

Professor, Departments of Radiology

Johns Hopkins University School of Medicine

Dr. Daniel Herzka

Assistant Professor, Department of Biomedical Engineering

Johns Hopkins University School of Medicine

Table of Contents

List of Figures

List of Tables

Chapter 1 Fundamentals of Diffusion MRI

1.1 Basics of Magnetic Resonance Imaging (MRI)

Magnetic resonance imaging (MRI) utilizes the main magnetic field, radiofrequency (RF) field, and magnetic gradients to map the spatial distributions and other properties of several nuclei in biological tissues. In this thesis, I am working exclusively with MRI of water proton (^{1}H), so MRI here refers to proton MRI. Basic image contrasts provided by MRI include proton density, longitudinal magnetization (T1), and transverse magnetization (T2). It is an important medical imaging technique to visualize the anatomy and physiology of the brain and other organs.

1.1.1 MR Physics

In most medical applications of MRI, protons (hydrogen atoms) in water molecules are the source of MR signal, which have well-known magnetic properties and behave as the nuclear spins. When proton spins are subjected a main magnetic field (B_0 field, in unit of Tesla), the spins tend to align in the direction of the magnetic field at equilibrium, giving

rise to a net magnetization. At the same time, the spins precess about the axis of the B_0 field at a well-defined frequency, the Larmor Frequency (ω_0):

$$\omega_0 = \gamma \cdot B_0 \qquad \text{Equation 1.1}$$

where γ is the nuclear specific gyromagnetic ratio, which is 42.576 x 10^6 Hz/tesla for proton (^{1}H) (1).

When an electromagnetic radiofrequency (RF) pulse is applied at the same Larmor frequency, the nuclear spins absorb the electromagnetic energy and the equilibrium state is disturbed, called the excitation. From a macroscopic view, the net magnetization vector rotates in a spiral movement from the direction of B_0 field (Z axis), down to the direction of the RF field (XY plane, perpendicular to Z). In a rotating frame of reference, the net magnetization vector tips down during excitation, and the flip angle depends on the strength and duration of the RF pulse.

Shortly after the excitation, the spins will return from the excited states to thermal equilibrium. This process is called relaxation, which follows two different mechanisms:

1) Longitudinal relaxation is due to energy exchange between the spins and surrounding lattice (spin-lattice relaxation). The longitudinal component (along Z axis) of the magnetization (Mz) recovers according to

$$\frac{dM_z}{dt} = -\frac{M_z - M_0}{T1} \qquad \text{Equation 1.2}$$

where T1 is the spin-lattice time constant and characterize the tissue-specific relaxation time when the longitudinal magnetization returns to 63 % of its equilibrium value. T1 values increase with increasing B_0. M0 is …

2) Transverse relaxation results from spins getting out of phase. As spins move together, their magnetic fields interact (spin-spin interaction), slightly modifying their precession rate, which causes a cumulative loss in phase and transverse magnetization (Mxy, in the XY plane,) decay.

$$\frac{dM_{xy}}{dt} = -\frac{M_{xy}}{T2} \qquad \text{Equation 1.4}$$

where T2 is the spin-spin time constant and characterize the tissue-specific relaxation time when then transverse magnetization losses 63% of its original value. T2 values decrease with increasing B_0, and T2 ≤ T1.

Combining Equation 1.4 and 1.5, the dynamics of the nuclear magnetization can be described by the Block equation (2):

$$\frac{d\overline{M}}{dt} = \overline{M} \times \gamma \overline{B} - \frac{(M_x - M_0)\overline{k}}{T1} - \frac{M_x \overline{i} + M_y \overline{j}}{T2} \qquad \text{Equation 1.5}$$

which describes the precessional behavior (first term), as well as the exponential relaxation of both the longitudinal (second term) and the transverse (third term) components.

1.1.2 Imaging principles

Decoding of the spatial distribution of the spins relies on application of magnetic field gradients, which is the time derivation of the magnetic field $G = \frac{dB}{dt}$ along three dimensions. The different gradients used to perform spatial localization are applied at distinct moments and in different directions. For example, the frequency encoding (FE) gradient, the phase encoding (PE) gradient, and the slice selection (SS) gradient are along three orthogonal directions.

By solving Block equation for an inhomogeneous object with time-varying gradients, the received MR signal from an excited location at (x, y, z) can be simplified as

$$s(t) = \int_x \int_y \int_z m(x, y, z) e^{-i2\pi\left[k_x(t)x + k_y(t)y + k_z(t)z\right]} dx dy dz \qquad \text{Equation 1.6}$$

where $m(x,y,z)$ is a function of the spin magnetization properties, such as density $\rho(x,y,z)$, $T_1(x,y,z)$, and $T_2(x,y,z)$, and $k_x(t)$, $k_y(t)$, and $k_z(t)$ are the time integrals of the gradient waveforms along x, y, and z, respectively: $k_x(t) = \frac{\gamma}{2\pi}\int_0^t G_x(\tau)d\tau$, $k_y(t) = \frac{\gamma}{2\pi}\int_0^t G_y(\tau)d\tau$, and $k_z(t) = \frac{\gamma}{2\pi}\int_0^t G_z(\tau)d\tau$. What is Gx, etc?

Equation 1.6 states that the MR signal can be interpreted as the spatial Fourier transformation of the spin magnetization. Therefore, the readout signal directly recorded from the MR receiver coil resides in a Fourier space of the MR image, called the *k*-space. By increasing or decreasing the FE and PE gradients, MR signals will fill up the k-space, whose 2D or 3D Fourier transform gives an MR image of the spin distribution. This is known as the spin warping method (3), and so far the most common MR reconstruction method.

By manipulating the timing, duration, and strength of MR gradients and RF pulses, various MR pulse sequences can be generated, which give rise to a large reservoir of MR image contrasts with rich anatomical and functional information. Basic MR pulse sequences include the gradient echo sequence and spin echo sequence (Figure 1.1) and their derivations, such as the steady state fast precession (SSFP), inversion recovery (IR), echo planar imaging (EPI), fast spin echo (FSE), etc (1).

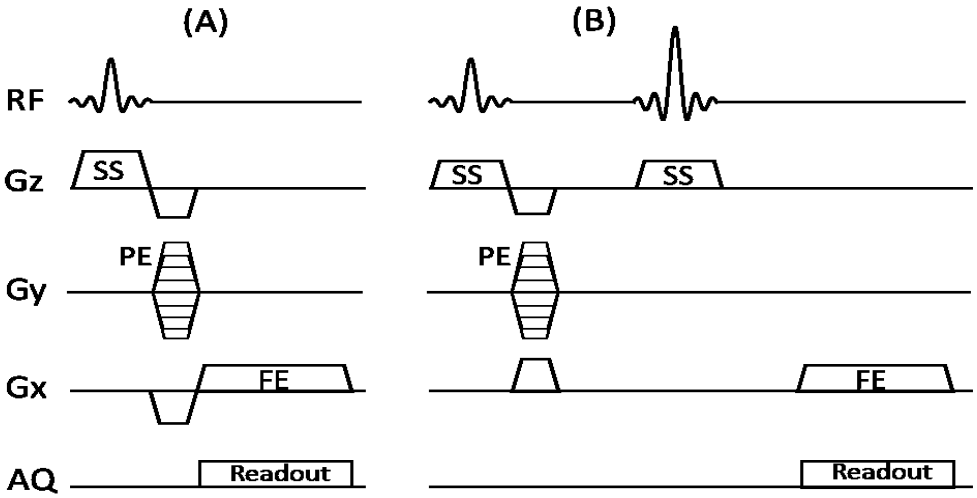

Figure 1.1: Pulse sequence diagrams of (A) gradient echo sequence and (B) spin echo sequence, which consist of the radiofrequency (RF) pulse, slice selection gradient (SS), phase encoding (PE) gradient, frequency encoding (FE) gradient, and signal readout.

1.1.3 Applications of MRI in Biomedicine

Since the first NMR-based image by Dr. Paul Lauterbur in 1973 (4), MRI has come a long way to become a major medical imaging tool for diagnosis of a variety of neurological diseases. Compared to computer tomography (CT) and optical imaging, MRI can generate rich image contrasts adapted for different diagnostic purposes, especially in the brain (Figure 1.2). For example, the T2-weighted image contrast from a fluid attenuated inversion recovery (FLAIR) sequence is widely used for detection of periventricular lesions in patients with multiple sclerosis (MS); MR angiography (MRA) enhances the arteries to evaluate them for stenosis (vessel wall narrowing) or aneurysms (vessel wall

dilatations); MR spectroscopy (MRS) is used to measure the levels of different metabolites in brain tissues; Functional MRI (fMRI) measures blood-oxygen-level dependent (BOLD) signal changes in the brain that is related to neural activity; diffusion MRI utilizes water diffusion to probe tissue microstructure and is particular useful for early detection of stroke and delineation of white matter structures, which will be described in detail in the following section.

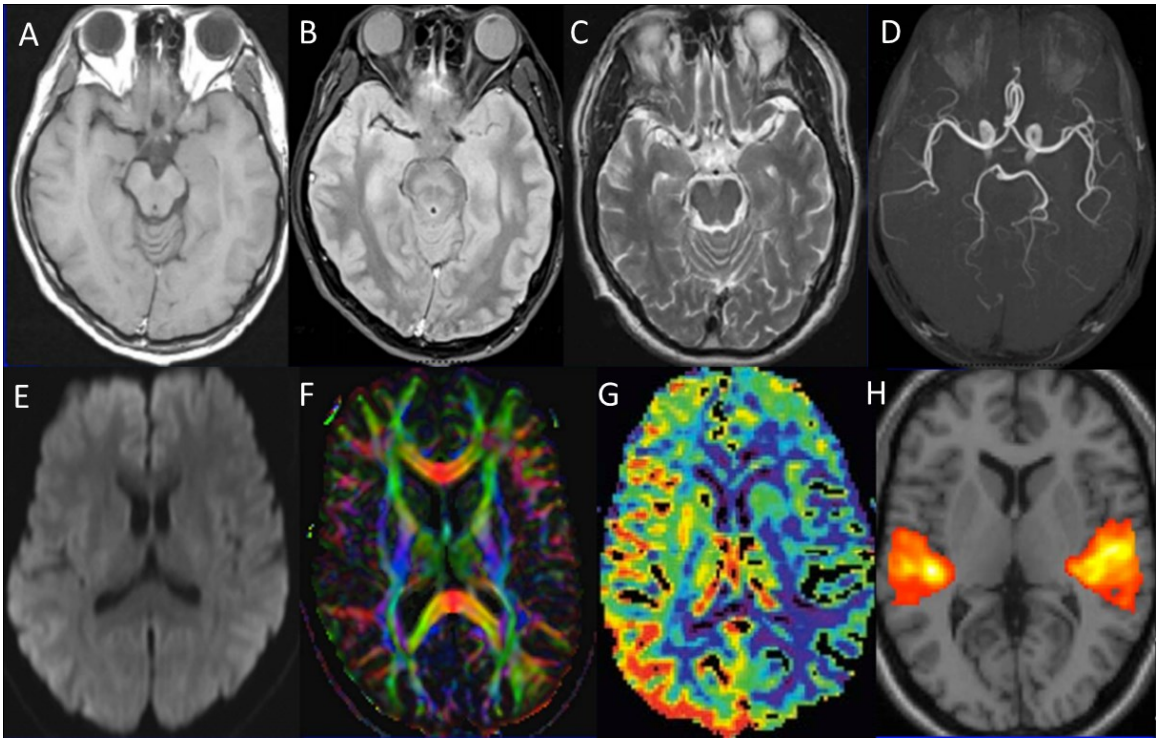

Figure 1.2: A range of MRI modalities that embodies rich anatomical and functional information, such as the proton density imaging (A), T2-weighted imaging (B), T1-weighted imaging (C), angiography (D), diffusion-weighted imaging (E), diffusion tensor imaging (F), perfusion imaging (G), and functional MRI (H).

1.2 Diffusion MRI

Diffusion MRI (dMRI) came into existence in the mid-1980s (5-7), which allows the mapping of the behavior of water molecule diffusion in biological tissues. Water molecules in tissues do not diffuse freely as they do in a bottle of water, but interact with many obstacles, such as macromolecules, cell membrane and myelin sheath (8). Therefore, by examining the behavioral of water molecule diffusion, dMRI can potentially reveal microscopic details about tissue microstructure, in normal or pathological states.

1.2.1 Physics of Diffusion

The equation that characterize the Brownian motion of the molecules was first described by Albert Einstein in 1905, known as the Einstein equation for diffusion

$$<(x' - x)^2> = 2Dt \qquad \text{Equation 1.7}$$

where x is the displacement of molecules during diffusion time t, and D is the diffusion coefficient, characteristic of the molecule and its diffusion environment. This relation leads to the definition of diffusion coefficient

$$D = \lim_{t\to\infty} \int_0^t \langle v(\tau)v(0)\rangle d\tau \qquad \text{Equation 1.8}$$

where $<v(\tau)v(0)>$ is the autocorrelation function of the molecular velocity.

In 1956, Torrey modified Bloch's original description of transverse magnetization to include diffusion terms (9), called the Bloch-Torrey equation:

$$\frac{d\overline{M}}{dt} = \overline{M} \times \gamma \overline{B} - \frac{M_x \bar{i} + M_y \bar{j}}{T2} - \frac{(M_x - M_0)\bar{k}}{T1} + \nabla \cdot D\nabla \overline{M} \qquad \text{Equation 1.9}$$

1.2.2 Diffusion weighted imaging

Diffusion MRI utilizes diffusion sensitization gradients to examine the behavior of water diffusion in biological tissues. The dMRI sequence, in its simplest form, originated from the Stejskal-Tanner experiment (10) to measure the water diffusion. As illustrated in Figure 1.3, a pair of pulsed gradients was applied before and after the 180° pulse. If the water molecules are stationary, the spin dephasing induced by the first diffusion gradient will be rephrased by the second diffusion gradient. If the water molecules move during the applications of the first and second diffusion gradient, the dephasing will not be fully refocused by the rephasing gradient, and therefore, the magnitude of the MR signal is attenuated as described in Equation 1.9.

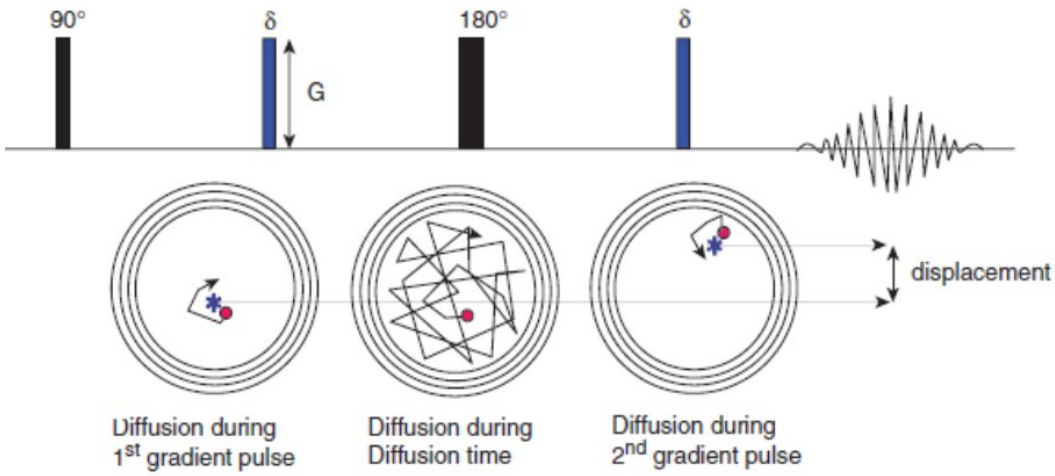

Figure 1.3: A schematics of the Stejskal-Tanner experiment to measure molecular displacement during application of the dephasing and rephasing gradient (adapted from (11) Chapter 9.

The amount of diffusion attenuation depends on the shape, strength, and timing of the diffusion gradients, characterized by so called "*b*-value".

$$S/S_0 = exp(-b \cdot D) \qquad \text{Equation 1.10}$$

where $$b = \gamma^2 \int_0^{TE} \left[\int_0^t G(t')dt'\right]^2 dt \qquad \text{Equation 1.11}$$

D denotes the diffusion coefficient and *G* denotes the diffusion gradient. In a pulsed gradient spin echo sequence (Figure 1.3), the *b*-value can be simplified as (10)

$$b = \gamma^2 G^2 D \delta^2 (\Delta - \delta/3) \qquad \text{Equation 1.12}$$

where δ is the duration of the diffusion gradients, and Δ is the diffusion separation time, which include the time from the beginning of the first gradient to the beginning of the

second gradient. When the diffusion gradients are applied simultaneously along several directions, the *b*-value can be generalized to a *b*-matrix and $S/S_0 = exp(-\Sigma\Sigma b_{ij} \cdot D_{ij})$ with $i = x,y,z$ and $j = x,y,z$.

Later, it was realized the in a complex media, the molecular diffusion behavior no longer follows self-diffusion as described in Equation 1.8. To address this deficiency, Tanner introduced the notion of the apparent diffusion coefficient (ADC) (12), defined as the diffusivity one would calculate using the Stejskal and Tanner formula (10), if the displacement distribution were Gaussian.

1.2.3 Diffusion tensor MRI and other advanced dMRI

The ADC in anisotropic tissue varies depending on the direction in which it is measured, e.g., ADC measured along an axon is higher than ADC measured perpendicularly to it. In order to measure the direction-depend diffusion, application of a series of gradients with distinct directions is required. A more general description of water diffusion uses a three-dimensional (3D) Gaussian model of molecular displacements, which introduces diffusion tensor of water (13-15), $\boldsymbol{D}$ as matrix in place of a scalar ADC to describe the orientation dependence of water diffusion. With diffusion-weighted signals

from ≥ six independent directions, the diffusion tensor ***D*** can be estimated by multivariate linear regression from Equation 1.10, along with several tensor-derived parameters, such as fractional anisotropy (FA), radial diffusivity, and axial diffusivity. These scalar measurements are widely used for evaluation of white matter integrity such as axonal damage and demyelination (16,17).

However, the diffusion tensor model is based on a Gaussian description of displacement distribution function and over-simplifies the water diffusion in complex biological tissues. To address these limitations, advanced diffusion acquisition and reconstruction schemes were established. For example, diffusion spectrum imaging (DSI) provides a model-free approach that directly relates the diffusion signal decay with a 3D displacement distribution function via a Fourier transform (18). Compared to DTI, DSI is sensitive to intra-voxel heterogeneities in diffusion directions caused by crossing fiber tracts, but requires a large set of diffusion directions and high diffusion attenuation. Along this line, variations of DSI with varying diffusion direction sampling schemes were developed, such as the high angular resolution diffusion imaging (HARDI) or Q-ball imaging (19), and multi-shell Q-ball imaging (20).

On the other hand, sophisticated diffusion models were investigated to extract specific geometric information of microstructures, such as the AxCaliber model (21), the NODDI model (22), the diffusion basis spectrum model (23) and many other compartment models. Higher order diffusion models such as the diffusion kurtosis imaging (DKI) (24), and other non-Gaussian diffusion MRI (25) are also explored. Furthermore, different diffusion sensitization gradients were also used to probe unique microstructural information at varying scales, such as the double pulsed field gradient MRI (26) and the oscillating gradient diffusion MRI (27).

1.2.4 Diffusion MRI tractography

Advances in diffusion MRI provides non-invasive ways of mapping the white matter fiber tracts in the brain. Since 1999, DTI based fiber tracking (28,29) has been recognized as a valuable tool to visualize and evaluate the 3D organization of the WM pathways, to perform tract-specific measurements or tract-based brain parcellation, and even assist real-time neurosurgical planning.

Over the last decade, various diffusion tractography algorithms have emerged, along with specific software packages to facilitate the implementation. In addition to the original

deterministic streamline tracking that propagate the trajectory according to the direction of the major eigenvector of the tensor, probabilistic tracking algorithms (30-32) were proposed to incorporate the orientation uncertainty to reduced systematic errors during tracking. In order to address the issue of crossing fibers within voxels that commonly present in the brain, advanced diffusion models are used to provide orientation distribution function (ODF) or fiber orientation distribution (FOD) basis for fiber tracking, such as the Q-ball reconstruction (33) and spherical decomposition (34) using Q-ball or HARDI data. However, a recent study (35) showed that although emphasizing the crossing fibers improve the sensitivity in fiber tracking, it reduced the specificity at the same time.

Diffusion tractography of the brain connectivity has attracted wide attentions in recently years, such as the investments in the north American human connectome project (36,37) and the European human brain project (https://www.humanbrainproject.eu/), while the validity of the *in vivo* tractography is still under investigation (38-41).

1.2.5 Applications of diffusion MRI and its limitations

Ever since its first use in detecting cerebral ischemia in the cat brain (42), diffusion MRI has become the major clinical diagnostic tool for acute stroke (43-46), which is

important for early administration of therapeutic interventions. The subsequent pseudonormalization of ADC at subacute stages and the further increase of ADC at chronic stages (47-50), help to identify the transition from acute cytotoxic edema to vasogenic edema due to the breakdown of the blood-brain barrier and cell membrane damage. Although the empirical knowledge is well established about ischemic stroke and its demonstration in diffusion MRI, the mechanism of the underlying pathology that give rise to the diffusion signal change is not yet clear (42,51-54).

Besides its wide application in stroke, diffusion MRI is frequently used to detect demyelination diseases and axon loss, such as that in multiple sclerosis (55-57). Moreover, the unique contrasts from diffusion MRI is particularly useful in studying the brain development. Compare to the conventional T1 and T2 weighted imaging, dMRI is able to delineate the unmyelinated microstructures in the developing brains (58,59) and to detect fetal brain injuries (60-63).

Although diffusion MRI have shown to be important tool in delineating neuroanatomy and detecting neurological diseases, limitations of this technique are recognized, regarding its acquisition and reconstruction procedures and the inclusive relation between the diffusion MRI signal and the underlying microstructure. For example, imaging artifacts

results from the eddy currents, EPI distortion, and motion are still hampering the image quality of *in vivo* dMRI; the spatial resolution of *in vivo* dMRI on current scanner systems is limited compared to the scale of tissue microstructures; histological validation of the reconstructed microstructures and tractography is insufficient; and the interpretation of dMRI diagnosis is still ambiguous. In this dissertation, we attempted to address some of these issues and proposed our solutions.

Chapter 2 *In vivo* high-resolution diffusion tensor imaging of the mouse brain

2.1 Introduction

Diffusion tensor imaging (DTI) (64) is a useful tool for studying brain anatomy and pathology. Based on a three-dimensional (3D) Gaussian model of water molecule diffusion, DTI provides several unique image contrasts that can reveal the spatial arrangement and structural integrity of major white matter tracts in the brain (65-69). Besides its utility in the clinic, DTI has also been frequently applied in basic research to examine the laboratory mouse brain (70). It has been widely used to characterize white matter injuries in mouse models of neurological disease, e.g., traumatic brain injury (71), multiple sclerosis (72), and stroke (73). DTI has also been used to study brain development and its genetic control mechanisms through various mutant mouse models (74-76), as the macroscopic information about neuro-anatomy provided by DTI complements the cellular and molecular information from histology. The wide applicability of DTI to studies on mouse brain anatomy and pathology makes it useful to have DTI based mouse brain atlases to assist structure delineation and lesion detection in DTI data. To fulfill this demand, several

ex vivo DTI based mouse brain atlases have been established, which provided exquisite anatomical details within the mouse brain (77-79). However, currently no high-resolution *in vivo* atlas is available.

While *in vivo* mouse brain DTI can now be routinely performed, its application to a broader range of mouse models is still limited by the available imaging resolution and speed. The reason is that several complex structures in the mouse brain, e.g., the small white matter tracts in the thalamus, can only be visualized properly with high-resolution imaging (80,81). Such high-resolution DTI of the live mouse brain, however, requires lengthy acquisition times, which limits the throughput and makes it challenging to use DTI to examine neonatal or injured mice that may not survive long MRI scans. Even though *ex vivo* DTI can be used to acquire high-resolution images from postmortem samples (80-82), it cannot substitute for *in vivo* DTI when longitudinal monitoring is necessary. Recent reports have also shown that *ex vivo* DTI is less sensitive to certain white matter injuries than *in vivo* DTI due to changes in tissue microstructure associated with death and chemical fixation (83-86).

Because signal-to-noise ratio (SNR) is the main factor dictating the available resolution and speed in MRI, improvement in SNR can be translated into improvements in

imaging resolution and speed. In the past few years, high-field magnets and sensitive radio frequency coils in combination with fast imaging sequences have greatly enhanced our ability to use DTI to examine the mouse brain (74,80,87-89). The recent advent of the cryogenic probes (cryoprobes), which can significantly improve SNR by reducing the thermal noise of the electronics, has opened new opportunities to further improve the resolution and speed of *in vivo* mouse brain DTI. Several recent reports have shown that a cryoprobe can improve SNR by a factor of 2-3 over similar room temperature coils under comparable experimental conditions (90,91). The use of fast imaging sequence is also critical for *in vivo* mouse imaging. Compared to conventional diffusion-weighted spin-echo (DW-SE) or echo-planar (DW-EPI) sequences, the diffusion-weighted gradient-spin-echo (DW-GRASE) sequence (80) provides imaging speed comparable to multi-shot DW-EPI but with reduced image distortion. In this study, we demonstrate high-resolution *in vivo* DTI of the mouse brain using a transmit-receive cryoprobe and the DW-GRASE sequence at 11.7 Tesla. Based on the results, an *in vivo* group-averaged DTI atlas of the adult mouse brain with structural segmentation was developed, together with a detailed analysis of the differences in structural morphology and tissue contrasts between the *in vivo* atlas and a previous *ex vivo* atlas.

2.2 Material and methods

2.2.1 Animals and experimental setup

All experimental procedures were approved by the Animal Use and Care Committee at the Johns Hopkins University School of Medicine. Both adult (C57BL/6, two-month old, female, n = 8, from three litters) and neonatal (postnatal day 7, 11 and 14, n = 3) C57Bl/6 mice were used.

2.2.2 Image acquisition

In vivo imaging was performed on a horizontal 11.7 Tesla MR scanner (Bruker Biospin, Billerica, MA, USA) with a triple-axis gradient (maximum gradient strength = 74 Gauss/cm) and a quadrature surface transmit/receive cryogenic probe with a size of 20 mm x 16 mm for each of two RF elements. The surface temperature of the cryoprobe was maintained at 37 ^{o}C. During imaging, mice were anesthetized with isoflurane (1%) together with air and oxygen mixed at 3:1 ratio via a vaporizer and positioned in an animal holder (Bruker Biospin, Billerica, MA, USA). Custom-designed mouse beds with different sizes were built for positioning the neonatal mice. Respiration was monitored via a pressure

sensor (SAII, Stony Brook, NY, USA) and maintained at 40-60 breaths per minute. After imaging, animals recovered within 5 minutes.

In vivo DTI of the adult mouse brains was performed using a modified 3D diffusion-weighted gradient and spin echo (DW-GRASE) sequence (80) with the following parameters: TE/TR = 33/500 ms, 2 signal averages, 20 imaging echoes (4 spin echoes distributed along the phase encoding direction and 16 gradient echoes distributed along the slice selection direction) after each excitation with twin navigator echoes in the end for motion and phase corrections, 12 diffusion directions, $b = 1000$ s/mm^2, field of view (FOV) = 16 mm x 16 mm x 17.6 mm, a matrix size of 128 x 128 x 140, and a native imaging resolution = 0.125 mm x 0.125 mm x 0.125 mm. BIR4 adiabatic pulses (92) were used to achieve uniform excitation and refocusing over the 3D volume of interest. With respiratory gating, the total imaging time was approximately 2-2.5 hours. The same protocol was used for 3D DTI of the neonatal mouse brains, except that the FOV was reduced to 16 mm x 13 mm x 15 mm and the matrix size was reduced to 128 x 104 x 120. The total imaging time was within 1.5 hours with respiration gating. In each experiment, the point spread functions (PSFs) due to T2 and T2* decays were measured along the phase encoding and slice selection directions, and the average FWHM (full width at half maximum) of the PSFs

were approximately 0.082 mm and 0.098 mm respectively. The SNR was evaluated as the ratio of the mean signal intensity against the standard deviation of noise, where signals were averaged from 1 mm^2 boxes within the regions of interest (ROIs) and the noise was chosen from the background of the image in an area of about 4 mm^2.

2.2.3 Data processing

The 3D images acquired using the DW-GRASE sequence were reconstructed from raw data in MATLAB (www.mathworks.com) with navigator-based motion and phase correction (93). Using the log-linear fitting method implemented in DTIStudio (http://www.mristudio.org) (94), diffusion tensor was calculated at each pixel along with the apparent diffusion coefficient (ADC), fractional anisotropy (FA), primary eigenvector, axial diffusivity ($\lambda_{\parallel}$, the primary eigenvalue), and radial diffusivity ($\lambda_{\perp}$, the average of the secondary and tertiary eigenvalues). The adult mouse brain images were rigidly aligned to *ex vivo* mouse brain images in our MRI based mouse brain atlas (78) using the landmark based rigid transformation implemented in the DiffeoMap software (www.mristudio.org). 3D reconstruction of white matter tracts was performed in DTIStudio using the multi-ROI fiber assignment by continuous tracking (FACT) method (69,95,96).

Based on the 3D adult mouse brain images (n = 8), group-averaged mouse brain images were generated using the iterative procedure described in (78,97) , first using intensity based linear affine transformation (98) and then dual-channel (ADC+FA) large deformation diffeomorphic metric mapping (LDDMM) (99) implemented in Diffeomap. ADC and FA maps were used for image registration because they provide complimentary contrasts that define the brain and ventricular boundaries (from the ADC image) and internal white matter tracts (from the FA image) and are not directly affected by the inhomogeneous intensity profile associated with the transceiver (91). Sixty brain structures were manually segmented in the group-averaged mouse brain images as described in (78), following the Paxino's mouse brain atlas (100,101). The group-averaged mouse brain images and structural segmentation together formed the *in vivo* group-averaged adult mouse brain atlas.

For comparisons between *in vivo* and *ex vivo* mouse brain DTI data, a previously published *ex vivo* DTI based mouse brain atlas (78) and datasets (C57BL/6, 2-3 months old female, n = 10) were used. Using dual-channel (ADC+FA) LDDMM, *in vivo* and *ex vivo* diffusion tensor images of each mouse brain were registered to the *in vivo* and *ex vivo* mouse brain atlases, respectively. Using the maps derived in this process, the structural

segmentations in the atlases were transformed to the rigidly aligned individual mouse brain data and refined by manual segmentation. Based on these segmentation results, volumes and diffusion parameters (ADC, FA, $\lambda_{\parallel}$, and $\lambda_{\perp}$) of major structures were obtained from both datasets. Differences in structural volume and diffusion parameters between the *in vivo* and *ex vivo* datasets were tested using the nonparametric Wilcoxon test. To further quantify the morphological differences between the *in vivo* and *ex vivo* mouse brain atlases, a mapping between the two atlases was also generated using the dual channel (ADC+FA) LDDMM. By concatenating this mapping with the mapping from individual *ex vivo* mouse brain to the *ex vivo* template, a combined mapping from individual *ex vivo* mouse brain to the *in vivo* atlas was obtained. Based on the mappings from individual *in vivo* and *ex vivo* mouse brains to the *in vivo* mouse brain atlas, Jacobian maps (102) were calculated, and voxel-wise comparisons of the Jacobian maps from the *in vivo* and *ex vivo* datasets were performed (Matlab, Mathworks, www.mathworks.com) after correction for multiple comparisons with a false discovery rate of 0.05 to locate regions with significant changes in local tissue volume. A tissue displacement map was also calculated between the group-average *in vivo* and *ex vivo* mouse brain images to characterize morphological differences.

2.3 Results

In vivo high-resolution DTI enhanced our ability to non-invasively examine microstructures in the mouse brain. As is shown in Figs. 2.1(A-B), when an isotropic resolution of 0.125 mm is used, small white matter structures in the adult mouse brain (e.g., the stria medullaris, stria terminalis, and fasciculus retroflexus) could be delineated in the *in vivo* DTI data. As is also shown in Fig. 2.1(D-E), complex 3D trajectories of these white matter tracts could be reconstructed and visualized with high spatial resolution in all three dimensions. Certain gray matter regions that possess unique DTI contrast patterns, e.g., the axon-rich layers in the hippocampus and the cerebellar cortex, could also be resolved. The *in vivo* data, however, showed a small but noticeable loss of sharpness attributed to T2/T2* decay and physiological motions when compared to our previous *ex vivo* 3D DTI data (Fig. 2.1(C)), which were acquired at the same spatial resolution using a diffusion-weighted spin echo sequence for over 20 hours (78).

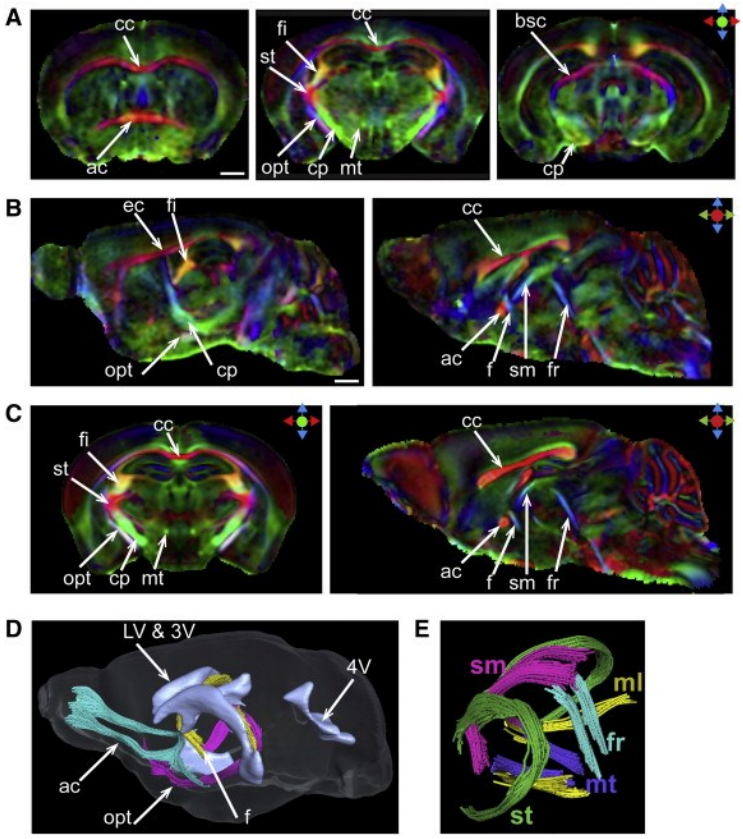

Figure 2.1: *In vivo* 3D high-resolution DTI and tractography of a representative adult mouse brain at 0.125 mm isotropic resolution. Direction-encoded colormaps (DECs) at several coronal slices (A) and sagittal slices (B) of the mouse brain are compared to matching images from our previous *ex vivo* data (C) of the same resolution after rigid alignment of the two datasets. The high resolution of the *in vivo* data allows reconstruction of both major and small white matter tracts (D & E) in the brain. The red-green-blue color scheme used in the DEC images is: red: left-right axis; green: rostral-caudal axis; blue: superior-inferior axis. Abbreviations: ac – anterior commissure; bsc: brachium sup colliculus; cp– cerebral peduncle; opt – optical tract; fi – fimbria; f – fornix; ml: medial lemniscus; sm – stria medullaris; st – stria terminalis; fr– fasciculus retroflexus; LV – lateral ventricle; 3V – third ventricle; 4V – fourth ventricle. Scale bar = 1 mm.

The relatively short acquisition time and high resolution made it possible to acquire *in vivo* DTI data from neonatal mouse brains. Fig. 2.2 shows high-resolution 3D DTI data

acquired from normal P7, P11 and P14 mouse brains. Even though the sizes of the neonatal mouse brains were significantly smaller than the size of the adult mouse brain, the high-resolution 3D DTI data allowed us to delineate immature white matter (e.g., the corpus callosum and stria medularis) and gray matter structures (e.g., cerebellar cortex) in the neonatal mouse brain. It is necessary to note that due to the geometry of the cryoprobe (dual surface coil quadrature setup), the *in vivo* data have decreasing SNR along the dorsal-ventral axis of the brain (Table 2.1).

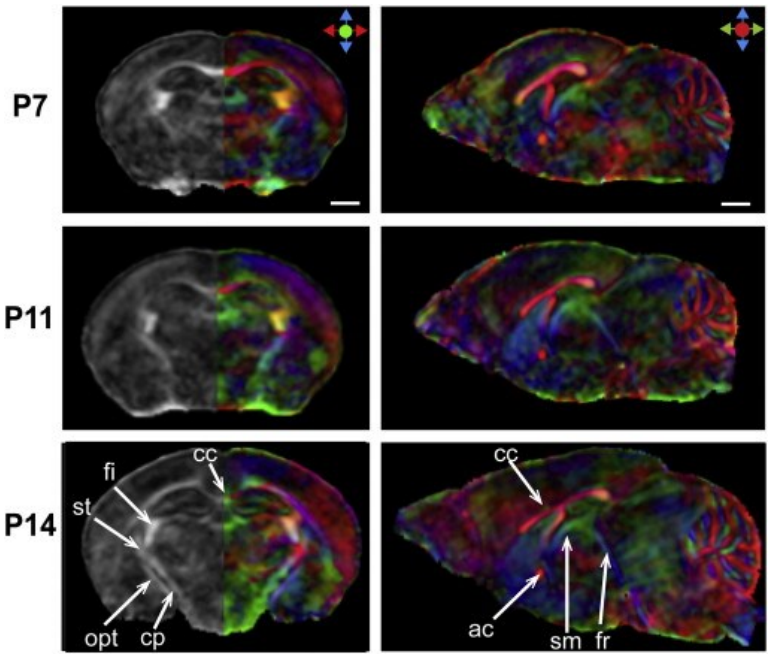

Figure 2.2: *In vivo* DTI of normal neonatal mouse brains at 0.125mm isotropic resolution. Coronal and sagittal FA and DEC images at postnatal day 7 (P7), 11 (P11), and 14 (P14). Abbreviations: cc –corpus callosum; ac – anterior commissure; cp– cerebral peduncle; opt – optical tract; fi – fimbria; sm – stria medullaris; st – stria terminalis; fr– fasciculus retroflexus. Scale bar = 1 mm.

Table 2.1: SNR values in five dorsal to ventral brain regions of *in vivo* (n = 8) and *ex vivo* (n = 10) mouse brain DTI images. The mean SNR values and standard deviations were measured on the non-diffusion-weighted images.

Structures	*In vivo*	*Ex vivo*
Cortex	161.5±8.8	175.8±21.3
Hippocampus	133.3±11.9	203.1±21.3
Thalamus	90.3±12.1	148.5±12.9
Hypothalamus	73.3±10.5	199.8±30.7
Amygdala	69.8±9.4	196.4±24.4

A group-averaged *in vivo* high-resolution DTI dataset of the adult mouse brain was created to study group-averaged morphological features and tissue contrasts (Fig. 2.3). Although a loss in image sharpness due to residual mismatch after registration among the subject images could be observed in the averaged images, small white matter tracts in the thalamus and cerebellar cortex/white matter remained well defined. A segmentation map of 60 brain structures of the *in vivo* mouse brain atlas was generated (Fig. 2.3, superimposed on direction-encoded colormap images). The group-averaged atlas and datasets can be downloaded at (http://cmrm.med.jhmi.edu).

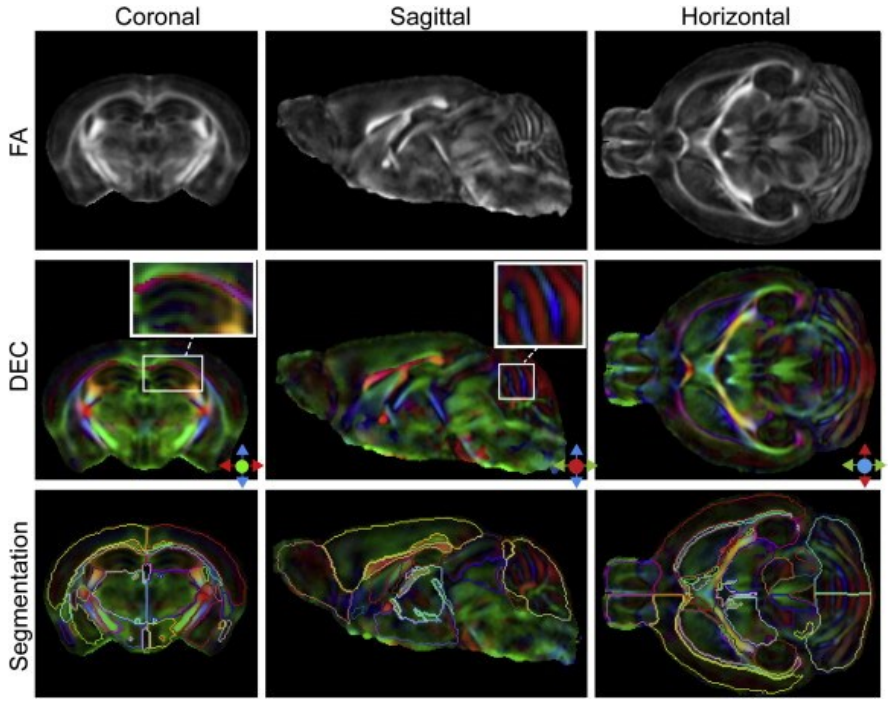

Figure 2.3: Group-averaged FA and DEC images and structural segmentations in the *in vivo* mouse brain DTI atlas. Average FA and DEC images from eight adult mouse brains are shown in coronal and horizontal views. Inset figures magnify complex structures from the hippocampus and cerebellum. Outlines of structural segmentations are overlaid on the DEC images.

Several differences were observed in structure morphology and tissue water diffusion properties between the *in vivo* and *ex vivo* mouse brain DTI data. Although the volumes of major brain structures did not change significantly between *in vivo* and *ex vivo* data (Table 2.2), the 60% reduction in the ventricular volumes after death and fixation was accompanied by large deformations in its neighboring structures. For example, in the tissue displacement and Jacobian maps (Fig. 2.4), the hippocampus showed a large displacement

accompanied by significant ($p < 0.05$) expansion at its caudal portion (indicated by the white arrows in Fig. 2.4) in the *ex vivo* mouse brains (n = 10). The dorsal cortex also showed relatively a large tissue displacement and significant expansion in local tissue volume (indicated by the yellow arrows in Fig. 2.4).

Table 2.2: ROI-based measurements in gray matter structures of the *in vivo* and *ex vivo* mouse brain DTI datasets. The volume (mm^3), ADC (mm^2/s) and FA in several major gray matter structures are presented as mean ± standard deviation from *in vivo* (n=8) and *ex vivo* (n=10) DTI data. Gray matter segmentations defined in the *in vivo* atlas were transformed to individual mouse brain data and used as ROIs. * $p < 0.01$, ** $p < 0.005$.

Structures	Volume (mm^3)		ADC ($x10^{-3}$ mm^2/s)		FA	
	In vivo	*Ex vivo*	*In vivo*	*Ex vivo*	*In vivo*	*Ex vivo*
Cortex	100.4±5.1	99.5±4.9	0.55±0.02	0.45±0.10	0.21±0.01**	0.19±0.01
Hippocampus	25.0±1.4	26.5±2.4	0.56±0.03**	0.45±0.10	0.25±0.02	0.25±0.02
Striatum	21.0±0.9*	23.0±1.8	0.52±0.03*	0.41±0.10	0.27±0.02**	0.18±0.01
Thalamus	20.6±0.9	20.7±1.4	0.53±0.03**	0.39±0.07	0.37±0.03**	0.27±0.01
Septum	1.6±0.1	1.8±0.2	0.63±0.05**	0.41±0.10	0.35±0.03**	0.25±0.01
Cerebellum	54.9±3.0	55.0±1.6	0.50±0.03**	0.37±0.09	0.35±0.02**	0.29±0.02
Ventricles	8.42±0.71	3.36±0.47	NA	NA	NA	NA

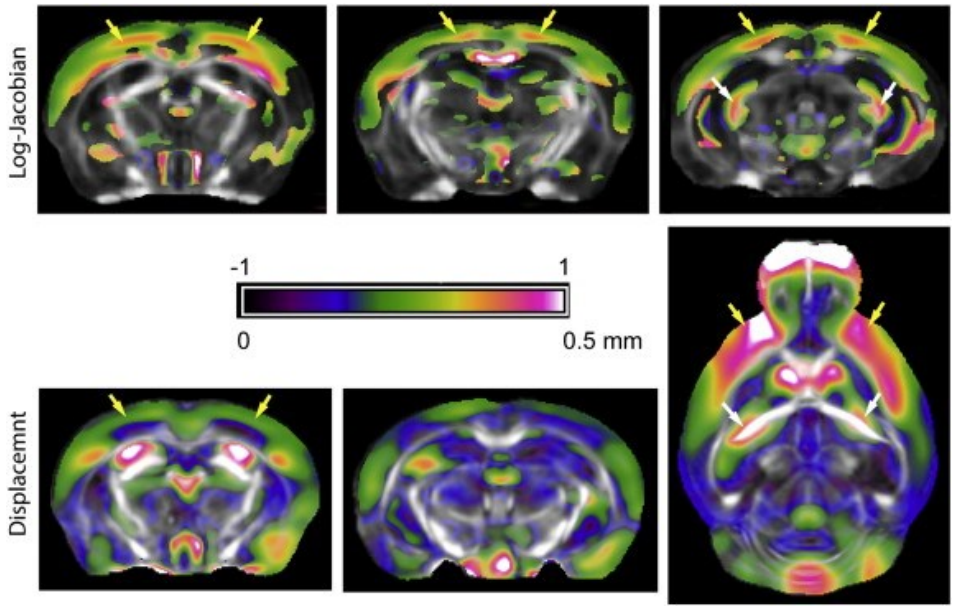

Figure 2.4: Morphological differences between the *in vivo* (n = 8) and *ex vivo* (n = 10) mouse brains. (Top row) Color-coded Log-Jacobian maps of the transformation between the *in vivo* and *ex vivo* mouse brains superimposed on average *in vivo* FA maps). Only the voxels with significant changes in Log-Jacobian values ($p < 0.05$ after corrections for multiple comparisons) are shown. A Log-Jacobian value greater than 0 indicates expansion of the *ex vivo* mouse brains with respect to the *in vivo* mouse brains, and shrinkage otherwise. (Bottom row) Color-coded maps of estimated tissue displacement between the average *ex vivo* and *in vivo* mouse brain images superimposed on average *in vivo* FA maps. Cortical and hippocampal regions that show large morphological changes between the *in vivo* and *ex vivo* images are indicated by the yellow and white arrows, respectively.

While the FA changed significantly in gray matter (Table 2.2), FA values measured in major white matter tracts *in vivo* and *ex vivo* show no apparent difference (Table 2.3), which agrees with previous reports (86). ADC measured in major white matter tracts were significantly reduced in the *ex vivo* data (Fig. 2.5(A) and Table 2.3), with both axial diffusivity and radial diffusivity reduced proportionally with ADC (Table 2.3). In major

gray matter structures, ADC values were also reduced in the *ex vivo* data, but less than white matter structures (e.g., approximately 20% reduction in the cortex vs. 47% reduction in the corpus callosum, Tables 2.2 and 2.3), and FA also showed significant reduction, e.g., in the cortex, cerebellum, and thalamus (Table 2.2). As a result of these changes, the ADC images of the *in vivo* and *ex vivo* mouse brains showed different contrasts, with the *ex vivo* ADC image showed stronger contrast between the white and gray matter structures than *in vivo* ADC image (Fig 2.5(A)). In the axial diffusivity images, the contrast between the cortex and corpus callosum observed *in vivo* mostly disappeared *ex vivo*, whereas in the radial diffusivity images, the contrast was preserved (Fig. 2.5(B)). The standard deviations of ADC measured in the *ex vivo* mouse brains (n = 10) were larger than those measured *in vivo* (n = 8), whereas standard deviations of FA measured *ex vivo* were mostly less than those measured *in vivo* (Fig. 2.5(C)).

Table 2.3: ROI-based comparison of white matter diffusion properties in the *in vivo* and *ex vivo* mouse brains. The FA, ADC (mm^2/s), parallel diffusivity ($\lambda_{//}$, mm^2/s) and radial diffusivity ($\lambda_{\perp}$, mm^2/s) of several white matter tracts are presented as mean ± standard deviation from *in vivo* (n=8) and *ex vivo* (n=10) DTI data. White matter segmentations defined in the *in vivo* atlas were transformed to individual mouse brain data and used as ROIs. * $p < 0.01$, ** $p < 0.005$ Abbreviations: cc –corpus callosum; ac –anterior commissure; opt –optical tract; ic –internal capsule; fi –fimbria; fx –fornix.

Structures	FA		ADC (x10^{-3} mm^2/s)		$\lambda_{//}$ (x10^{-3} mm^2/s)		$\lambda_{\perp}$ (x10^{-3} mm^2/s)	
	In vivo	*Ex vivo*	*In vivo*	*Ex vivo*	*In vivo*	*Ex vivo*	*In vivo*	*Ex vivo*
cc	0.52±0.02	0.53±0.02	0.58±0.03**	0.31±0.08	0.95±0.04**	0.52±0.11	0.79±0.05**	0.44±0.10
ac	0.57±0.03	0.54±0.02	0.56±0.03**	0.32±0.09	0.97±0.05**	0.56±0.13	0.70±0.06**	0.44±0.10
opt	0.66±0.04	0.64±0.03	0.63±0.04**	0.31±0.06	1.22±0.12**	0.61±0.10	0.67±0.05**	0.34±0.05
ic	0.60±0.03	0.57±0.02	0.55±0.04**	0.33±0.07	0.98±0.06**	0.59±0.10	0.66±0.08**	0.42±0.07
fi	0.68±0.02**	0.64±0.02	0.69±0.05**	0.26±0.06	1.33 ±0.06**	0.47±0.10	0.73±0.08**	0.31±0.06
f	0.49±0.04	0.44±0.03	0.52±0.04**	0.30±0.07	0.83±0.06**	0.46±0.10	0.74±0.08**	0.45±0.09

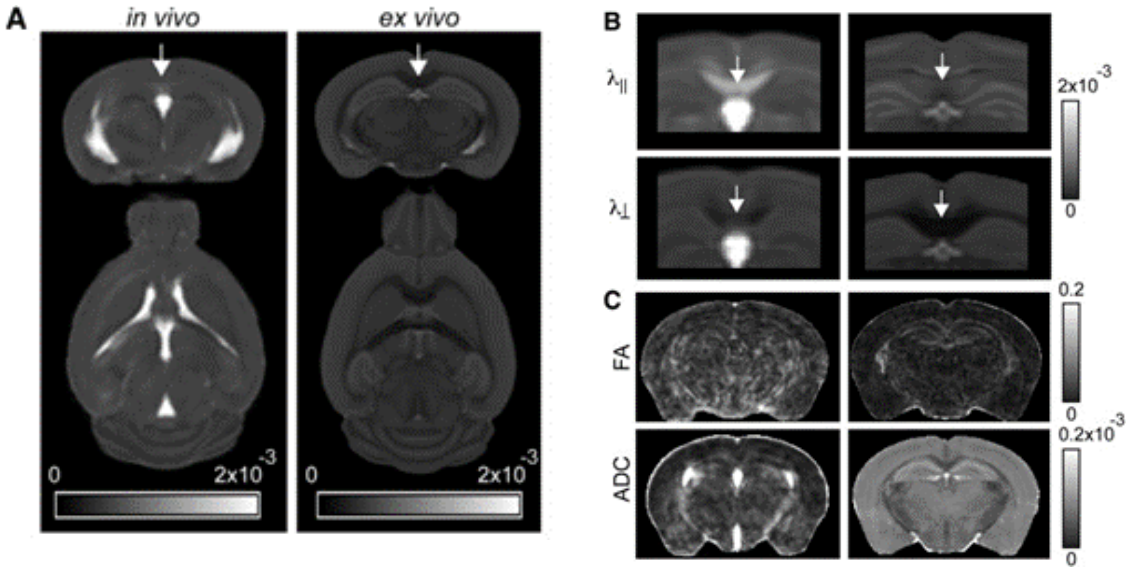

Figure 2.5: Morphological and diffusion properties differ between the average *in vivo* and *ex vivo* mouse brains. (a) ADC measured in the *in vivo* mouse brain (left) is much higher than that in the *ex vivo* mouse brain (right). (b) Parallel diffusivity ($\lambda_{//}$) and radial diffusivity ($\lambda_{\perp}$) show different white matter – gray matter contrasts in the *in vivo* and *ex vivo* mouse brains. (c) Standard deviation of ADC and FA maps in the *in vivo* (n=8) and *ex vivo* (n=10) groups.

2.4 Discussion

In this study, high-resolution DTI data were acquired using a 3D imaging sequence, while previous *in vivo* DTI studies mostly used multi-slice sequences, e.g., multi-slice spin echo or multi-slice EPI. Multi-slice DTI is more time efficient than 3D DTI, and has been commonly used to study the structural integrity of major white matter pathways, such as the corpus callosum, in mouse models (89,103). With four-segment EPI acquisition, Harsan et al., reported *in vivo* mouse brain DTI (30 diffusion directions) with an in-plane resolution of 0.156 mm x 0.156 mm and 0.5 mm slice thickness (88). Multi-slice DTI, however, has limited through-plane resolution (~0.5 mm) depending on available gradient strength and SNR. The partial volume effect due to this limitation makes it difficult to delineate complex white matter or gray matter structures along the slice direction. The limited through-plane resolution also is not ideal for co-registering images from multiple animals, as interpolations in the slice direction can often cause visible degradation in image resolution. Compared to multi-slice acquisition, 3D acquisition allows high spatial resolution along all three dimensions at the cost of longer acquisition times, which often limits its application for imaging live mice. Previous studies using 3D DTI were mostly *ex vivo* anatomical studies (80,81,104). Recently, Cai et al. demonstrated *in vivo* 3D DTI of

the neonatal rat brain using a 3D diffusion weighted fast spin echo sequence with a spatial resolution of 0.15 mm x 0.15 mm x 0.2 mm in 3 hours (87).

By using a cryoprobe, we were able to speed up 3D acquisition by reducing the repetition time while still maintaining an acceptable SNR. Two recent reports demonstrated high-resolution *in vivo* mouse brain DTI using a cryoprobe and multi-slice sequences (105,106). With 11.7 T cryoprobe and a 3D DW-GRASE imaging sequence, we were able to acquire 3D images from the adult and neonatal mouse brain with an isotropic resolution of 0.125 mm within 2-2.5 hours. Even though the *in vivo* 3D DTI results shown here still could not match our previous *ex vivo* 3D DTI in term of SNR or image sharpness (Table 2.1 and Fig. 2.1), the results nonetheless showed considerable improvements in our ability to resolve small structures in the live mouse brain. The spatial resolution in this study was chosen so that the *in vivo* mouse brain data could be compared to our previous *ex vivo* mouse brain data at similar levels of partial volume effects. In practice, if a reduced resolution is deemed satisfactory to delineate the target structures or lesions, the acquisition time can be shortened to increase screening throughput. While the cryoprobe offers significant advantages over conventional room temperature coils for imaging the mouse brain at high resolution, it also has its own technical constraints. The cryoprobe used in this

study operated in transceiver mode. As a result, the intensity profile of the diffusion-weighted images and the SNR measured in different parts of the brain were not uniform (Table 2.1), which may affect the quantification of the measured diffusion parameters, e.g., FA and diffusivities (107,108) . The non-uniform excitation and refocusing profiles can also result in imaging artifacts for multiple RF sequences such as the GRASE sequence used here. To resolve this problem, we applied adiabatic excitation and refocusing pulses to achieve near uniform excitation and refocusing profiles at the expense of high radio-frequency power deposition. Improved coil design such as discussed in (90) or the use of room temperature body coil transmission with phased array cryocoil receive is expected to offer more uniform excitation profiles in the future.

Using the high-resolution *in vivo* mouse brain DTI data, we constructed a group-averaged DTI atlas of the live mouse brain. Mouse brain atlases are important resources for basic neuroscience research because they contain useful anatomical information for identifying brain structures and understanding their spatial relationships. While there are several histology-based mouse brain atlases (e.g., (100)), whose structural definitions are commonly used as the gold standard, MR-based atlases have been established in recent years, with increasing resolution and sophistication (i.e., multiple MR contrasts, detailed

structural segmentation, and creation of population averaged and multi-modality brain atlases) (77-79,109-118). Compared to histology-based atlases, MR-based atlases are inherently three-dimensional, and the ability to construct group-averaged atlas makes it possible to present group-averaged anatomical features and quantify inter-subject variability. MR-based mouse brain atlases are useful in analyzing MRI data acquired from mouse brains, for example, automatic structural segmentation and volume measurements (109,119-121). They can also be used as templates to perform voxel-based analysis to examine changes in structural morphology and tissue properties (122-126). Many of these MR-based atlases, especially DTI based mouse brain atlases, were previously generated from post-mortem brain specimens in order to achieve high spatial resolution and image quality. Post-mortem data, however, may not accurately capture the properties of the brain under normal physiological conditions as death and chemical fixation can alter structural morphology and tissue properties (83-86,111). By comparing *in vivo* T2-weighted images with *ex vivo* T2*-weighted images acquired from brain specimens dissected out of the skull, Ma et al. (111) reported significant differences in structural volume and surface areas between *in vivo* and *ex vivo* data. Keeping the brain inside the skull could reduce but not completely remove the structural deformation associated with death and fixation (77). In

terms of tissue diffusion characteristics, Sun et al (86) showed significant differences in tissue ADC values after death and fixation but no apparent change in white matter FA values. For studies that involve *in vivo* monitoring of structural morphology and pathology using DTI and perform atlas or voxel-based image analysis of *in vivo* mouse brain DTI data, it is beneficial to have an *in vivo* mouse brain atlas and a good understanding of the differences between *in vivo* and *ex vivo* DTI-based outcome measures.

In this study, using the structural segmentation embedded in the atlas, differences between the *in vivo* and *ex vivo* mouse brain datasets were systematically characterized. Compared to previous studies based on T2-weighted images (77,111), the rich DTI contrasts allowed accurate registration for white matter structures (99), which in turn improved the overall image registration quality and enhanced our ability to detect subtle morphological differences between *in vivo* and *ex vivo* mouse brain images. In addition to the well-documented collapse of the ventricles in post-mortem samples and deformations of surrounding structures, voxel-based analysis revealed additional regions with significant morphological differences between the two datasets, mainly located in the dorsal part of the brain. In term of changes in diffusion parameters after death and fixation, changes in gray and white matter contrasts in ADC maps, and to a lesser degree, in FA maps (Tables

2.2-2.3, and Fig. 2.5) suggest that the effects of death and chemical fixation on tissue ADC values were not uniform throughout the brain. As expected, FA values measured *in vivo* showed larger variability, both inter-subject and inter-scan, than FA measured *ex vivo*, because the *ex vivo* DTI data had higher SNR than the *in vivo* data and were free of motion-related artifacts. Interestingly, we found that the ADC values measured *in vivo* showed less variability than the ADC values measured *ex vivo*. Potential causes of this difference include variations due to perfusion fixation, e.g., differences in fixation related changes in cell membrane permeability and the ratio between intracellular and extracellular space, and precision of temperature control during *ex vivo* imaging. Even though the number of animals studied here is limited, these results suggest that the *in vivo* mouse brain atlas provides a more accurate representation of brain morphology and diffusion properties of the adult mouse brain under normal physiology condition than existing *ex vivo* atlases.

2.5 Conclusions

In summary, our study demonstrates the use of a cryoprobe in combination with 3D DW-GRASE sequence to achieve *in vivo* 3D high-resolution DTI of the mouse brain. The high resolution and relatively short acquisition time allowed detailed examination of

neuroanatomy and anatomical connectivity in the mouse brain. A high-resolution DTI atlas of the live mouse brain was developed with structure segmentations. Detailed analysis showed volumetric and contrast differences between *in vivo* and *ex vivo* DTI of the mouse brains, indicating the importance of the *in vivo* DTI atlas.

Chapter 3 Localized micro-imaging of the live mouse brain with HARDI

3.1 Introduction

Along with the many new and exciting technical advances in diffusion MRI (dMRI) as discussieed in Chapter 1.2.3, further developments of diffusion MRI (dMRI) hinge on our understanding of the relationships between dMRI signals and the underlying brain microstructure (22,23,39,127-129). Such knowledge can only be obtained through studying the relationships between dMRI signals and histopathological findings in experimental animal models. The laboratory mouse brain is an ideal subject for examining the microstructural basis of dMRI signals, because there is a wealth of histology-based information on its microstructure. In addition, there are many well-established mouse models that mimic various pathological conditions in patients with neurological diseases. Knowledge gained through studying the mouse brain using dMRI may be readily translated to study the anatomy and pathology of the human brain. dMRI of the mouse brain, however, faces many technical challenges (130) . The lengthy acquisition required by high-resolution dMRI to resolve mouse brain structures had essentially limited its application to post-

mortem specimens. Several recent studies on post-mortem rodent (80-82,131) have demonstrated that dMRI can be used to visualize complex microstructure in the mouse brain. *Ex vivo* dMRI, while offering superior image quality and high spatial resolution, has its own limitations, as death and chemical fixation can significantly alter the microstructural properties of brain tissues and the diffusion of water in those tissues, resulting in major differences in dMRI contrast between *in vivo* and *ex vivo* dMRI as demonstrated in the Chapter 2 and in (85,86,132). It is, therefore, important to develop *in vivo* high-resolution mouse brain dMRI techniques to investigate the potential of dMRI under physiological conditions.

In this work, we demonstrate that *in vivo* DTI and HARDI of the mouse brain can be performed at approximately 100 μm isotropic resolution using spatially selective RF pulses and a 3D gradient and spin echo (GRASE) imaging sequence (80,133). By selectively exciting a portion of the brain that contains the structures of interest, a dramatic reduction in imaging volume, and therefore, imaging time, was possible. Further acceleration was achieved using the 3D GRASE sequence, which, in this study, obtained images twenty times faster than conventional spin echo sequences. High-resolution dMRI data of the cerebellum, hippocampus, and several cortical regions of the mouse brain were compared

to histology, focusing on the capability of dMRI to resolve microstructures and connectivity in these regions.

3.2 Material and methods

3.2.1 Experimental animals

All experimental procedures were approved by the Animal Use and Care Committee at the Johns Hopkins University School of Medicine. Five adult mice (C57BL/6, three-month old, female) were used in this study.

3.2.2 RF pulse design

The 90˚ localized excitation RF pulses used in this study were designed based on a linear class of large tip-angle (LCLTA) pulses (134), with spiral *k*-space trajectories that start and end at the origin. Under the "incoherently refocused" condition (134), a two-dimensional spatially selective 90˚ RF pulse can be derived by inverse Fourier transform of the desired excitation profile. Although B1 field weighting can be incorporated in the Fourier kernel, we assumed a homogeneous B1 field across the mouse brain because the mouse brains were always positioned near the center of a large volume coil, and the inner

diameter (72 mm) of the volume coil was far larger than the size of the mouse brain (10-12 mm in diameter). The pulse length was set at 2.5 ms, and the pulse amplitudes ranged from 15 to 20 μT, depending on the size, position, and shape of the desired field of excitation (FOE) (134). The typical waveform of an RF pulse to excite a square region in the mouse brain is shown in Fig. 3.1(A-B). We chose an eight-turn spiral-in excitation k-space trajectory (Fig. 3.1(C-D)), which resulted in an excitation resolution of 1 x 1 mm in the x-y plane, with a maximum gradient strength of about 21 Gauss/cm. The imaging field of view (FOV) was chosen to be slightly larger than the field of excitation (FOE) to accommodate the transition area between the excited region and the suppressed region (approximately 1/10 of the FOE). The performance of the spatially selective RF pulses was tested using the standard, double flip-angle B1 mapping (135). While the FOE in the x-y plane was controlled by the selective excitation pulses, a slab-selective refocusing pulse (Mao pulse (136)) was applied to restrict the imaging slab in the z direction.

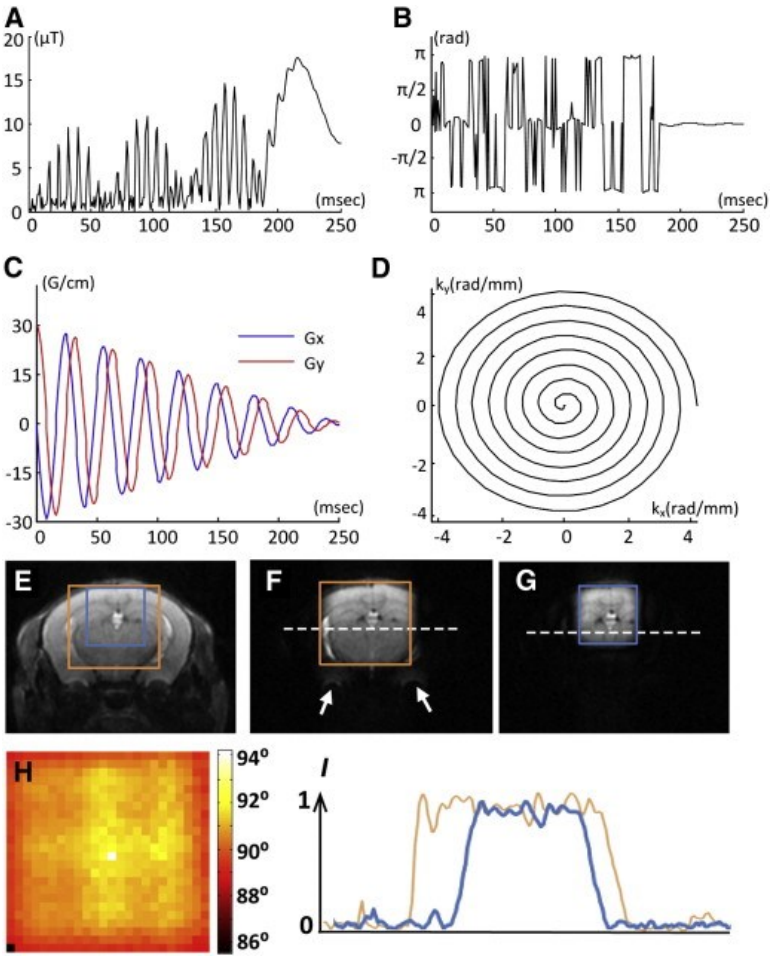

Figure 3.1: Spatially selective excitation RF pulse and its experimental validation. A-B: The pulse amplitude and phase of a typical 90° selective excitation pulse. C-D: an eight-turn spiral-in gradient waveform and excitation k-space trajectory in the x-y plane. The gradient waveform was synchronized with the RF waveform to achieve selective excitation. F-G: the results of selective excitation with 8 mm x 8 mm and 6 mm x 6 mm fields of excitation (FOEs), respectively. H: the measured flip angle map of the excited region (corresponding to the FOE in F). I: the normalized (with respect to the maximal value) intensity profiles along the dashed lines in F and G.

3.2.3 Image acquisition

In vivo imaging was performed on a horizontal 11.7 Tesla MR scanner (Bruker Biospin, Billerica, MA, USA) with a triple-axis gradient (maximum gradient strength = 74 Gauss/cm). The selective excitation pluses were transmitted though a quadrature volume excitation coil (72 mm diameter, Bruker Biospin, Billerica, MA, USA), and signal was acquired using a 10 mm diameter, planar surface receive-only coil (with active decoupling). Animal anesthetization and monitoring was the same as described in Chapter 2.2.1.

Before each dMRI experiment, a multi-slice, T_2-weighted image (echo time (TE) = 50 ms, repetition time (TR) of 2000 ms) was first acquired as an anatomical reference and was used to identify the FOE. Typical FOEs used in this study included the anterior brain FOE (approximately from the bregma 2 mm to -2 mm, covering the motor and sensory cortex); middle brain FOE (approximately from the bregma 0 mm to -4 mm, covering part of the sensory cortex, visual cortex, and hippocampus); and the posterior brain FOE (approximately from the bregma -5 mm to -9 mm, covering the cerebellum) as the main structures of interest (Table 3.1). The anterior and middle FOEs were designed to cover only half the brain, assuming relative symmetry in normal brains. For each FOE, the planar receive surface coil was placed immediately above the specific FOE to ensure optimal

sensitivity. Data were acquired with a modified 3D diffusion-weighted GRASE sequence (80), which acquired 40 echoes in each repetition. A double-sampled EPI readout (137), which samples the same *k*-space line twice, with both positive and negative gradients, was incorporated into the GRASE sequence to enhance SNR, as well as to reduce artifacts from imperfect read-out gradients. A twin-navigator (93) was implemented to correct motion-induced phase errors, and no respiration trigger was used. Using the Fieldmap method (138-140), B0 homogeneity in a region containing the FOE was optimized using the first and second order shim to reduce image distortion and a T_2* signal decay during the double-sampling EPI readout. A water line width of less than 30 Hz could be routinely achieved within the FOE. The imaging parameters of the HARDI protocol were: TE/TR = 21/500ms; two signal averages; 30 diffusion directions (141); b = 2335 s/mm^2; 63 minutes scan time for 0.1 x 0.1 x 0.1 mm resolution; and 102 minutes for 0.08 x 0.08 x 0.08 mm resolution. *Ex vivo* whole brain HARDI data were acquired from a postmortem C57BL/6 mouse brain specimen, which was perfusion fixed with 4% paraformaldehyde (PFA), and later transferred to phosphate buffered saline with 2 mM gadopentetate dimeglumine (Magnevist, Berlex Imaging, Wayne, NJ) (78) to enhance MR signals. Specimens were scanned using a vertical 11.7 Tesla NMR spectrometer (Bruker Biospin, Billerica, MA,

USA) and a birdcage volume coil (15 mm inner diameter). The same imaging sequence as that used *in vivo* MRI with whole-brain coverage was used, but with slightly different parameters: TE/TR = 27/1000ms; two signal averages; 30 diffusion directions; b = 4000 s/mm^2; 0.1 x 0.1 x 0.1 mm resolution. The total scan time was about 20 hours.

Table 3.1: Definition of the anterior, middle and posterior brain fields of excitation (FOEs), and the SNR of non-diffusion weighted images from these FOEs.

Field of Excitation (FOE)	Anterior	Middle	Posterior
FOE width & height (mm)	8 x 5	8 x 5	8 x 5
FOV size (mm) (readout x phase x slice)	9.6 x 5.6 x 4	9.6 x 5.6 x 4	9.6 x 5.6 x 4
Readout direction	Superior-inferior	Superior-inferior	Left-right
Slice position with respect to Bregma (mm)	+2 to -2	0 to -4	-5 to -9
Structures of interest	Motor/Sensory cortex Striatum (right hemisphere)	Sensory/visual cortex Hippocampus (right hemisphere)	Cerebellum
SNR	42 ± 0.6 (n=5)	44 ± 2 (*n*=5)	42 ± 2.6 (*n*=3)

3.2.4 Data processing

Images were reconstructed from k-space data using Matlab (Mathworks) and processed using MRtrix (142), which used the constrained spherical deconvolution (CSD) method to reconstruct fiber orientation distribution (FOD). FOD-based probabilistic streamline tracking was performed to generate super-high-resolution track density images

(TDI) (143,144). Fiber-tracking was performed using a step size of 0.01 mm and a maximum angle of 45° between steps. Tracking terminated when the FOD amplitude became less than 0.01, or when fibers exited the specific brain regions. Probabilistic streamlines with a length between 0.4 - 1 mm were selected (131), and about one million such streamlines were tracked to generate TDI at a grip size of 10 μm isotropic resolution.

3.2.5 Immunohistochemistry

Mice were anesthetized and perfused with 0.1M phosphate-buffered saline (PBS), followed by 4% paraformaldehyde in 0.1M PBS, and then were post-fixed with 4% paraformaldehyde for 12-18 hours. Brains were cryo-protected in a 30% sucrose solution in 0.1M PBS. The forebrain was cryostat-sectioned at 40 μm coronally and the cerebellum was sectioned at 20 μm parasagitally. Representative sections were mounted and adjacent slides were used for immunohistochemical stainings with different antibodies. Endogenous peroxidase was quenched using 3% hydrogen peroxide in 0.1M PBS. Antigen-retrieval was performed with 0.01 M citrate buffer containing 0.05% Tween-20 (pH 6). Slides were then incubated in blocking solution, followed by primary antibody incubation at 4°C overnight: Anti-Pan-Axonal Neurofilament Marker (SMI312R, Covance, Princeton, NJ, USA, 1:2000)

and Anti-Parvalbumin antibody (ab11427, Abcam, MA, USA, 1:4000) for the detection of large GABAergic neurons and their processes (e.g., Purkinje-Neurons of the cerebellum); Anti-Glial Fibrillary Acidic Protein antibody (Anti-GFAP Z0334, Dako, Richmond, VA, USA, 1:2500) for the detection of astrocytes; and Anti-Microtubule-associated Protein 2 (Anti-MAP2, M1406, Sigma-Aldrich, St.Louis, MO, USA, 1:1000) for the detection of neuronal dendrites. Negative control slides were put in blocking solution. Slides were rinsed and visualized using the ABC ELITE kit (Vector Labs, Burlingame, CA, USA) and 3,3′-Diaminobenzidine (DAB, Sigma-Aldrich, St. Louis, MO, USA). Images were acquired using a Zeiss Observer.Z1 microscope equipped with an AxioCam MRc camera at 20X.

3.3 Results

The 90° spatial excitation RF pulse designed in this study produced satisfactory 2D excitation profiles using a conventional quadrature volume coil at 11.7 Tesla. Images acquired with an 8 mm x 8 mm FOE and a 6 mm x 6 mm FOE are shown in Fig. 3.1(F-G). The residual outer-volume signal intensity was less than 6% of the average inner-volume signal intensity (Fig. 3.1(I)). For large FOEs that include air-tissue interfaces, e.g., the area

close to the ear canal, which have severe B0 inhomogeneity and thereby distort the excitation k-space trajectory, residual signals outside the FOE could be observed near the air-tissue interfaces (indicated by the white arrows in Fig. 3.1(F)). The artifact disappeared when the FOE fell completely within the brain (Fig. 3.1(G)). Within the selected region, the measured flip angles were relatively uniform (90°±2.2°, Fig. 3.1(H)).

Using selective excitation, high-resolution dMR images of local brain regions could be acquired within a relatively short time period. Figure 3.2(A) shows three sagittal direction-encoded colormap (DEC) images acquired separately with the anterior, middle, and posterior FOEs at 100 μm isotropic resolution. Figures 3.2(B-D) compare DEC images acquired at 80 μm isotropic resolution with images acquired at 100 μm and 125 μm isotropic resolution. With the standard 30-direction diffusion-encoding scheme, the imaging time ranged from 40 minutes for the 125 μm resolution data to two hours for the 80 μm resolution data in a local FOE (indicated by the cubic frame in Fig. 3.2(F)). Major white matter tracts, e.g., the corpus callosum, and several small white matter structures could be resolved in the high-resolution data (Fig. 3.2(A-B)). For example, the alveus of the hippocampus, a thin sheet of axonal fibers (indicated by the blue arrows in Fig. 3.2(B-E)), could be distinguished from the neighboring corpus callosum/external capsule and

hippocampus in the DEC image at 80 μm resolution (Fig. 3.2(B)). Tensor-based fiber-tracking results based on the 80 μm data could separate the alveus from the corpus callosum (Fig. 3.2(F-G)). In comparison, images acquired at 100 and 125 μm resolutions (Fig. 3.2(C-D)) showed the alveus with reduced FA and a loss of clearly defined diffusion orientation, due to partial volume effects. In order to reliably resolve small white matter tracts and crossing fibers, it is necessary to use more sophisticated approaches than the conventional diffusion tensor model. Figure 3.2(H) demonstrates that fiber orientation distribution (FOD) estimated from the dMRI data, using spherical deconvolution, could resolve the fibers in the alveus (blue FOD surface) and corpus callosum/external capsule (red FOD surface) at 100 and 125 μm resolution.

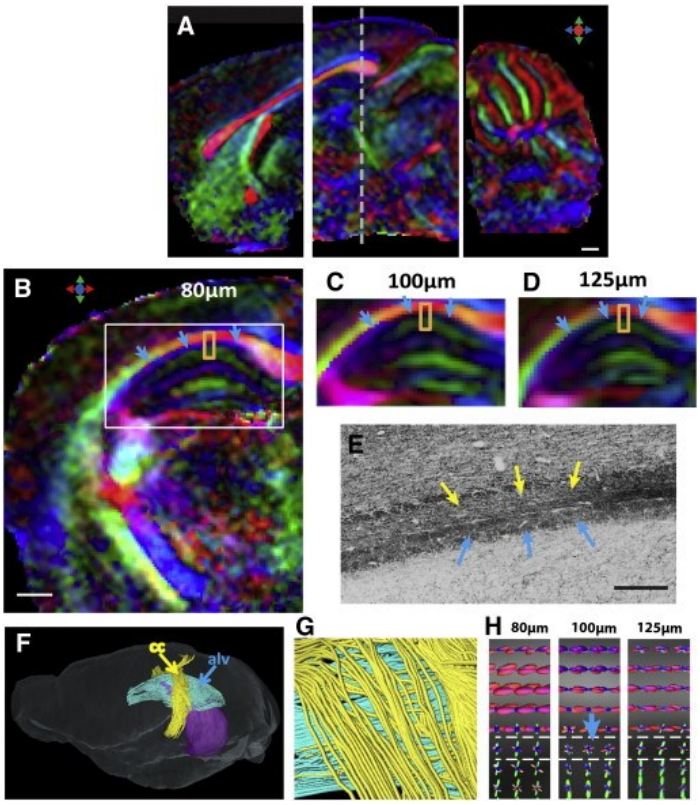

Figure 3.2: High spatial resolution diffusion MRI of the live mouse brain. A: Sagittal views of the DTI colormaps taken from the anterior, middle, and posterior FOEs used in this study. B-D: Axial direction-encoded colormaps of the hippocampus at 80 μm, 100 μm, and 125 μm isotropic resolutions, respectively. The axial location of these images is indicated by the dashed line in A. E: A Pan-Neurofilament-stained section that shows the alveus (alv) of the hippocampus (indicated by the blue arrows) and the corpus callosum (indicated by the yellow arrows). F-G: Fiber-tracking results at 80 μm isotropic resolution, where the corpus callosum fibers (yellow) and the alv fibers (blue) can be separated. The purple frame in F indicates the actual imaging volume. H: The fiber orientation distribution (FOD) maps of the selected regions (orange squares in B-D) at three resolutions. Scale bars in A and B are 500 μm, and the scale bar in E is 200 μm.

Figure 3.3 compares localized *in vivo* dMRI data with *ex vivo* whole-brain dMRI data, both acquired at 100 μm resolution. For white matter structures, the *in vivo* and *ex vivo*

DEC images (Fig. 3.3(A-B)) showed similar tissue contrasts, and several small white matter tracts, e.g., the dorsal hippocampal commissure and optic tracts, could be delineated in both datasets. In the hippocampus, the *in vivo* and *ex vivo* data both showed the radiating pattern (indicated by the orange arrows) reported previously (131,145). This is further illustrated using the track-density imaging (TDI) technique (Fig. 3.3(B-E)), which renders fiber tracking results at a resolution higher than the native imaging resolution, and provides an intuitive way to visualize tissue microstructures. This pattern was in good agreement with the spatial arrangement of small axons and dendrites in the hippocampus, as shown by the Parvalbumin-stained histological sections (Fig. 3.3(C-F)). Small differences in gray matter tissue contrasts, however, could be observed in several regions. For example, the *in vivo* data showed more prominent radially organized structures near the surface of the visual cortex (Fig. 3.3(D), indicated by the yellow arrows) and higher diffusion anisotropy in a region immediately above the dentate gyrus (Fig. 3.3(D), indicated by the blue arrows) than the *ex vivo* data.

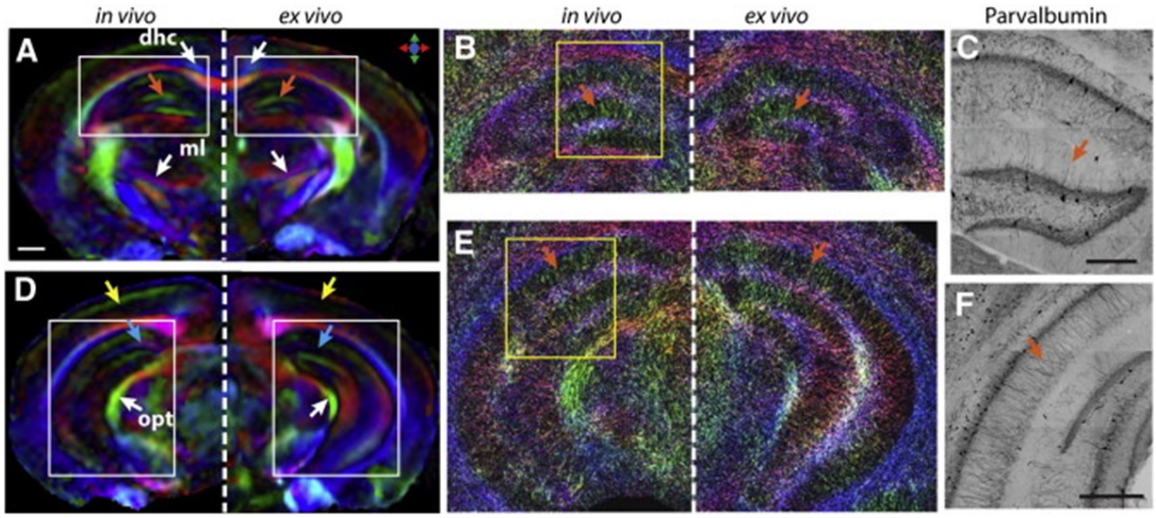

Figure 3.3: Comparison of the localized *in vivo* dMRI of the mouse hippocampus with the *ex vivo* results from a whole-brain scan. A-B: DTI colormaps (scale bar 500 μm) and TDI maps from the anterior hippocampus from the *in vivo* (left) and *ex vivo* (right, mirrored) dMRI experiments. C: Parvalbumin-stained section of a selected area in the anterior hippocampus. D-F: DTI colormaps, TDI map, and Parvalbumin-stained section of the posterior hippocampus, following the same order as in A-C. Abbreviations: dhc— dorsal hippocampal commissure; ml—medial lemniscus; opt— optical tract. Scale bars in C and F are 200 μm.

The *in vivo* high resolution HARDI data could provide detailed tissue microstructural information in the mouse brain. As shown in Figure 3.4(A), individual cerebellar folium and white matter tracts in the mouse cerebellum could be delineated in the DEC image based on the *in vivo* HARDI data. While the DEC image shows only the dominant structural components in each pixel, e.g., parallel fibers in the cerebellar cortex (indicated by the white arrow in Fig. 3.4(A)), spherical deconvolution of the HARDI data revealed additional structural components (represented by the blue FOD surfaces in Fig. 3.4(D)) that were

arranged perpendicular to the parallel fibers (represented by the red FOD surfaces in Fig. 3.4(D)). Neurofilament (NF)-, Glial Fibrillary Acidic Protein (GFAP)-, and Parvalbumin-stained sections (Fig. 3.4(C, E-G)) showed that the secondary structural components might include small axons, dendrites, and processes of glial cells in the cerebellar cortex, as they all run orthogonal to the parallel fibers (perpendicular to these sections). The high-resolution TDI of the cerebellum (Fig. 3.4(B)) demonstrated the spatial arrangement of axonal fibers as they fanned out near the end of the cerebellar folia, as shown by the neurofilament staining (Fig. 3.4(E))).

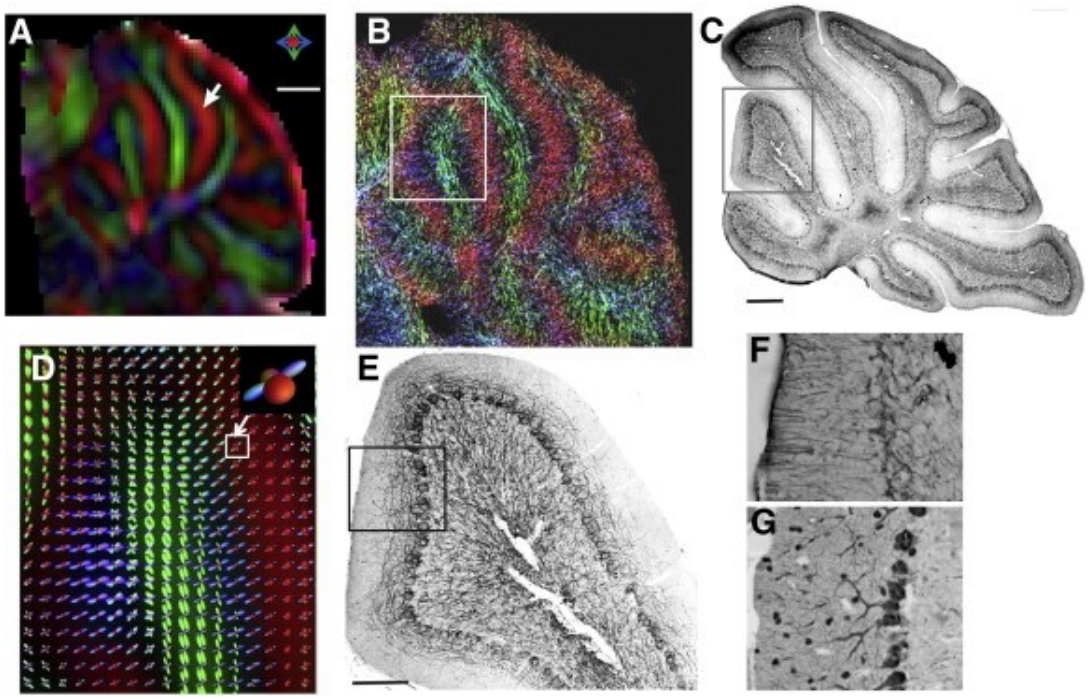

Figure 3.4: Localized HARDI of the mouse cerebellum. A-B: DTI colormap and TDI of the mouse cerebellum on a mid-sagittal view. C: Neurofilament-stained section corresponding to B. D: Fiber orientation distribution (FOD) map of the selected area

indicated in B. The inset plot indicates two groups of crossing fiber coexisting in the cerebellar cortex. E: Neurofilament-stained section corresponding to D. F-G: Glial fibrillary acidic protein (GFAP)- and Parvalbumin-stained sections of the cerebellar cortex. Scale bars in A and C are 500 μm, and the scale bar in E is 200 μm.

Figure 3.5 compares MRI and histological images of the mouse motor, sensory, and visual cortices. In all three cortical regions, MAP2-stained sections showed radially oriented long-running apical dendrites in the cortex. In comparison, NF-stained sections showed radially oriented axons in the outer layer of the cortex and densely populated axons with no clear dominant orientation in the inner layer. FOD maps derived from the *in vivo* HARDI data showed predominantly radially oriented FODs in the outer layer of the three cortices and both radially and tangentially oriented FODs in the inner layer of the cortices. Compared to the motor cortex, TDI-generated images showed that the inner layer of the sensory and visual cortices have a large amount of axons running tangentially to the cortical surface, and the estimated FOD maps showed these tangential fibers, especially in the visual cortex. In all three cortices, the outer layers had higher FA values than the inner layers, with most significant difference in the visual cortex (Table 3.2).

Table 3.2: FA values measured from the outer and inner layers of the motor, sensory, and visual cortices.

Regions of interest	FA	p-value

Motor cortex	Outer	0.143 ± 0.016	0.07
	Inner	0.136 ± 0.015	
Sensory cortex	Outer	0.142 ± 0.018	0.02
	Inner	0.122 ± 0.009	
Visual cortex	Outer	0.159 ± 0.009	9.5×10^{-5}
	Inner	0.090 ± 0.005	

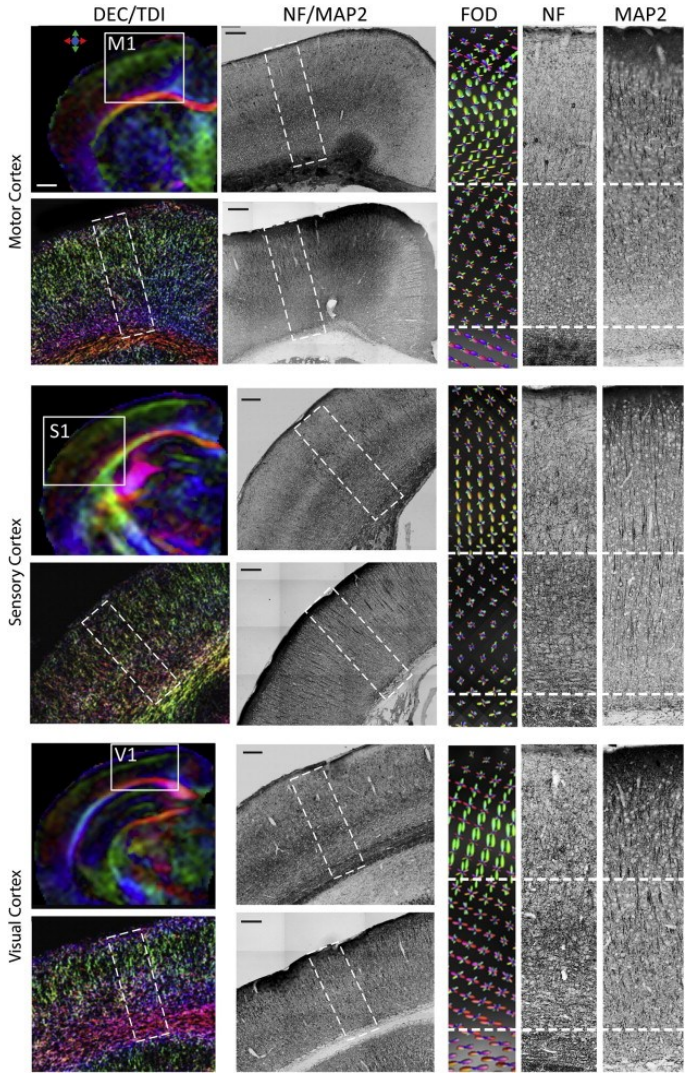

Figure 3.5: *In vivo* HARDI of the mouse motor (M1), sensory (S1), and visual (V1) cortices and corresponding neurofilament (NF) and microtubule-associated protein 2 (MAP2)-stained sections. Images in the left-most column are DTI colormaps of localized anterior / middle / posterior mouse brain FOEs and high-resolution TDI maps of the M1 / S1 / V1

cortices in selected areas, as indicated on the colormaps. The right-most three columns show FOD maps estimated from the HARDI data from each cortex and matching NF- and MAP2-stained sections. The regions shown in the FOD maps are indicated by the dashed rectangular boxes in the NF and MAP2 sections. The dashed lines in the right-most three columns separate the cortex into outer and inner layers. Scale bar in A is 500 μm, and all the other scale bars are 200 μm.

3.4 Discussion

Spatially localized imaging is a tried-and-true approach to obtain high-resolution images from a target region within a reasonable time. Even though imaging with whole-brain coverage is important for examining the overall anatomy or neuropathology, many studies that focus on a particular brain region, e.g., the mouse cortex and hippocampus, may benefit from the increased imaging resolution or speed provided by localized imaging techniques. Several techniques have been utilized to achieve spatial localization. For example, 2D localized imaging can be achieved by using a slice-selective 90° RF pulse and a 180° RF pulse in an orthogonal fashion (146,147), or by using direct 2D RF pulses as demonstrated by Finsterbusch et al. (148,149). While the former requires no specially designed RF pulses, the latter offers more flexibility in terms of pulse sequence design and shape of the region to be excited. The LCLTA pulses used in this study achieved satisfactory in-volume homogeneity (90° ± 2.2°) and outer-volume suppression within a

relatively short duration (2.5 ms), which was ideal for our experiments, as tissue T_2s shorten at a high magnetic field. Moreover, the LCLTA method provides an analytical approach to pulse design and is compatible with parallel transmission. For example, Xu, et al. (150) extended the LCLTA framework to an eight-channel parallel transmitter and achieved about a four-fold acceleration for 2D selective excitation profiles in a phantom experiment. Ullman et al. (151) demonstrated 3D localized imaging of the live rat brain based on a numerical optimization of small tip-angle pulses (152,153). In this study, the single-channel LCLTA pulse was integrated with our DW-GRASE sequence to improve the spatial and angular resolutions of *in vivo* dMRI experiments. Simple rectangular FOEs were sufficient here, given that the imaging volume is rectangular with conventional Cartesian k-space acquisition. Using the FOEs in our experiments, the imaging volumes were reduced to approximately one-sixth of the whole-brain volume, and the scan time was reduced proportionally. To mitigate the SNR loss associated with high spatial resolution, heavy diffusion attenuation, and short scan time, we placed a sensitivity surface receive coil as close to the FOE as possible. This, however, is only effective when the target regions are close to the head surface, such as the cortex, whereas the deep brain structures, e.g., the thalamus and the hypothalamus, still suffer from low SNR.

Localized high-resolution dMRI, using selective excitation and fast imaging sequences, allowed us to examine the live mouse brain in greater detail than ever before. While ultra-high resolution (<50 μm) *ex vivo* dMRI of the mouse brain has been reported (80-82), spatial and diffusion angular resolutions of the live mouse brain dMRI have been hindered by SNR and lengthy imaging time. Recently, Harsan et al. reported *in vivo* mouse brain HARDI (30 diffusion directions, b-value = 1000 s/mm^2) with an in-plane resolution of 0.156 mm x 0.156 mm and a 0.5 mm slice thickness in 99 minutes (154), and we have reported 125 μm isotropic resolution *in vivo* DTI (10 directions) of the mouse brain in three hours using a cryo-genic probe (132). In this study, we were able to acquire *in vivo* HARDI (30 diffusion directions, b-value = 2335 s/mm^2) of the mouse hippocampus at 80-100 μm isotropic resolution within one to two hours, and the level of microstructural details available in the *in vivo* high-resolution data were comparable to *ex vivo* data acquired at the same resolution (Fig. 3.3). We further tested the capability of the technique to resolve microstructures in the mouse cerebellum, which has been well documented. In the mouse cerebellar cortex, the *in vivo* data showed two orthogonally arranged groups of fibers: one parallel to the surface of the cerebellar cortex (represented by the red FOD surfaces in Fig. 3.4(D)), and the other perpendicular to the cerebellar cortex (represented by the blue FOD

surfaces in Fig. 3.4(D)), similar to previous reports based on post-mortem mouse brain specimens (155). The first group may reflect the densely packed parallel fibers in the cerebellar cortex, and the second group may reflect axons/dendrites of the cerebellar Purkinje cells (Fig. 3.4(G)) and processes of glia cells (Fig. 3.4(F)).

We then examined the microstructural organization of the mouse neo-cortex. There have been several reports on imaging cortical microstructures in the human brain. Diffusion anisotropy in the cortex was revealed in *in vivo* DTI studies of both developing (156) and mature (157) human brains. Several recent studies showed that different cortical regions have unique microstructural signatures. For example, McNab et al. showed that the human motor cortex contained mostly radially organized structures, whereas part of the sensory cortex showed tangentially organized structures (158). High-resolution HARDI of postmortem brain samples further delineated the layered patterns in the human cortex, e.g., Dyrby et al. separated the cortex into two depth layers based on the different fiber orientations in the inner and outer rims of the cortex (159); Leuze et al. divided the visual cortex into four layers using the FOD patterns and tractography feature (160). Other studies have attempted to parcellate cortical regions using raw diffusion signals (161) or FOD-derived contrasts (162,163). These post-mortem studies demonstrated that high-resolution

HARDI signals could be used to characterize the neo-cortical microstructure, especially the layered organization with radial or tangential patterns. It is not clear whether *in vivo* high-resolution data will show consistent cortical tissue contrasts and how the contrasts correlate with microstructures. As the human and mouse neocortex, despite their differences, share a similar columnar organization (164), high-resolution studies on the mouse cortex could bring insight into these questions. In this study, high-resolution dMRI of the mouse cortex showed contrast patterns similar to those seen in postmortem human brain specimens. For example, the observation that radially arranged structures dominate the outer layer of the visual cortex, while tangentially arranged structures dominate in the inner layer (Fig. 3.5), is similar to the observations reported by previous post-mortem human brain studies (159,160). A comparison between HARDI results and histological data suggested that multiple structural components could contribute to these unique patterns. MAP2-stained histological sections displayed relatively uniform radiating dendritic fibers in all three cortices, whereas neurofilament-stained sections showed a layered axonal organization, with the inner layer of the cortex more densely stained than the outer layer. While it is still difficult to quantitatively measure the contribution of each

structure's components, the results demonstrate the potential of our technique in assisting future detailed analysis.

3.5 Conclusions

In summary, we demonstrate that high spatial resolution and angular resolution dMRI of the live mouse brain is now feasible with localized imaging, in combination with fast imaging sequences. The dMRI contrast derived from the *in vivo* high-resolution data revealed complex microstructures in both the gray matter and white matter. The techniques presented in this study could be potentially used to investigate longitudinal changes in local neuroanatomy and connectivity under normal or diseased states.

Chapter 4 *In vivo* Mapping of the Mouse Intra-hippocampal connectivity

4.1 Introduction

Structural connectivity of the brain, from individual synapses to large white matter tracts, forms the fabric that supports brain functions, and often provides important clues that lead to deeper understanding of its structural and functional organization. Because of this, significant efforts have been made to construct a comprehensive map of the brain connectivity, and an array of imaging techniques have been utilized to map connectivity from the synaptic level using electron micrograph up to the system level using magnetic resonance imaging (MRI).

Diffusion MRI (70,165,166) based tract reconstruction, or tractography (167-169), has been increasingly used to map brain connectivity in terms of major white matter pathways, and is a major technical component of the Human Connectome Project (HCP) (36,37,170). While exciting new findings are emerging, most of them focus on large white matter tracts, while there exist a large amount of small white matter tracts that connect several functionally unique units within a brain region. Characterization of these tracts will

lead to better understanding of the structural organization of these units. Only recently, several groups started to use diffusion MRI to exam these tracts (171-173). At this level, the proximity of these small bundles of axons to neurons, astrocytes, and their processes, makes it challenging to determine their trajectories or microstructural properties as the current diffusion MRI technique cannot distinguish their contributions to the measured signals from other structures in the same pixel. Even with sophisticated diffusion modeling and tractography techniques recently proposed for this scenario, the fact that diffusion MRI only provides limited and indirect information on tissue microstructure at limited spatial resolution (~ 2 mm isotropic in human diffusion MRI) remain the main obstacles on our ways to solve the problem.

Given that diffusion MRI is the main non-invasive technique to study structural connectivity, spatial resolution is the key to study small white tracts in the brain. Recent high-resolution diffusion MRI studies of post-mortem human brain specimens have demonstrated unique sensitivity in identifying small white matter tracts. On one hand, the results from post-mortem specimens may not be directly translated to *in vivo* studies due to the significant microstructural changes associated with death and chemical fixation (174-176). On the other hand, it is not known the tractography obtained in *ex vivo* studies can be

replicated *in vivo* due to the limitations with *in vivo* imaging techniques, such as imaging resolution, motion artifacts, and signal-to-noise ratio. On existing MR instruments, *in vivo* imaging of the entire brain at exquisite high resolutions is so far impractical, due to the prolonged time it requires.

In this study, we used 3D high-resolution diffusion MRI to examine small fiber tracts in the live mouse brain, with a focus on the intra-hippocampal connectivity. The hippocampus is a prominent component of the nervous system that mediates memory, spatial navigation, and motion (177,178), and the anatomical and functional organizations of the mouse hippocampus have been investigated in depth as a model system (179-183). Besides its extensive connections to the rest of the brain, it contains an intrinsic network between its subfields that form distinct functional units (184-186). In the Allen Mouse Brain Connectivity Atlas (187), extensive tracer-based connectivity data in the mouse brain, including hippocampus, became readily available. Recently, we developed a localized dMRI technique that can "zoom-in" a region of interest in the mouse brain to acquire diffusion MRI data up to 0.08 mm isotropic resolution (188). Direct comparison of *in vivo* high-resolution diffusion MRI data of the mouse hippocampus with the Allen Mouse Brain Connectivity Data provided a unique opportunity to examine the capability of diffusion

MRI-based in reconstructing the intra-hippocampal network and allowed us to integrate the rich connectivity information obtained from the two vastly different modalities. This baseline mouse brain connectivity from histological and microscopic scale to *in vivo* and macroscopic scales also offers translational knowledge for human connectome research.

4.2 Methods

4.2.1 *In vivo* high resolution diffusion magnetic resonance imaging

Twelve adult mice (C57BL/6, three-month old, female) from the Jackson Laboratory (Bar Harbor, ME) were used in this study. *In vivo* MRI was performed on a horizontal 11.7 Tesla MR scanner, with the same setup and similar imaging procedures (selective excitation RF pulses and 3D DW-GREASE sequence) as described in Chapter 3.2.3.

In this study, the region for localized imaging, or field of excitation (FOE), had a spatial dimension of 8 mm (dorsal-ventral, the x axis) x 5 mm (mid-sagittal to lateral, the y axis) x 5 mm (from bregma 0 to -5 mm, the z axis). The FOE was set to cover the right hippocampus and surrounding regions. The imaging field of view (FOV) was chosen to be slightly larger than the FOE to accommodate the signal drop-off at the transition band of

FOE. The imaging parameters of the diffusion MRI protocol were: TE/TR = 21/500ms; two signal averages; FOV = 9.6 mm x 5.6 mm x 5 mm, resolution = 0.1 mm x 0.1 mm x 0.1 mm; four non-diffusion weighted image (b_0); 30 (n = 5) or 60 (n=7) diffusion directions (141); and b = 2500 s/mm^2. The diffusion imaging parameters were selected based on the recommendations in (189). It took less than 2 minutes to acquire a single diffusion-weighted image. It took 63 and 118 minutes to obtain a 30 and 60-direction HARDI datasets, respectively. Raw data from the scanner were Fourier transformed after zero-padding (to 50 μm isotropic resolution) with navigator-based phase correction (Matlab, Mathworks.com).

4.2.2 Histology

Immunohistochemical processing of the mouse brain samples followed the protocol described in Chapter 3.2.5. Coronal brain slices at the level hippocampus were stained with Anti-Pan-Axonal Neurofilament Marker (SMI312R, Covance, Princeton, NJ, USA, 1:2000) for axons and Anti-Microtubule-associated Protein 2 (Anti-MAP2, M1406, Sigma-Aldrich, St. Louis, MO, USA, 1:1000) for the detection of neuronal dendrites.

4.2.3 Registration of dMRI to Allen Mouse Brain Atlas

Projection mapping images from multiple subjects (n = 8 with injection sites in the hippocampus) were downloaded from the Allen mouse brain connectivity atlas. These images were labeled using injected recombinant deno-associated virus (AAV) tracers and acquired using serial two-photon microscopy with minimal tissue damage and deformation (190). A series of image registration procedures were taken to co-register the dMRI data and projection data, as shown in the pipeline in supplementary Fig. S1B. Since the high-resolution HARDI data acquired in this study only covered partial brain volume, a DTI-based *in vivo* whole mouse brain atlas from our previous study (176) was used as a link between the HARDI datasets and the Allen mouse brain reference atlas (191). First, the whole brain DTI-based mouse atlas was aligned to the Allen mouse brain reference atlas down-sampled to 50 μm isotropic resolution, using landmark-based rigid transformation (Diffeomap, www.mristudio.org) followed by intensity-based 12-degree affine transformation and large deformation diffeomorphic metric mapping (LDDMM) (99) utilizing the similar tissue contrasts between the reference atlas and dMRI images (Fig. 4.1(A)). Second, the HARDI datasets were aligned to the transformed whole brain DTI-based atlas (obtained from the previous step and cropped to match the localized volume in

the HARDI datasets) through landmark-based affine transformation and LDDMM. The registration accuracy between the down-sampled Allen reference atlas and the aligned HARDI datasets were evaluated using 15 landmarks manually placed throughout the hippocampus by three independent raters (75). The average registration error was 0.28 ± 0.14 mm in all three dimensions (Fig. 4.1(B)). After the registration steps, structural segmentations in the Allen mouse brain reference (678 structures including 17 hippocampal subfields) can be transferred into the HARDI datasets (Fig. 4.1(C)).

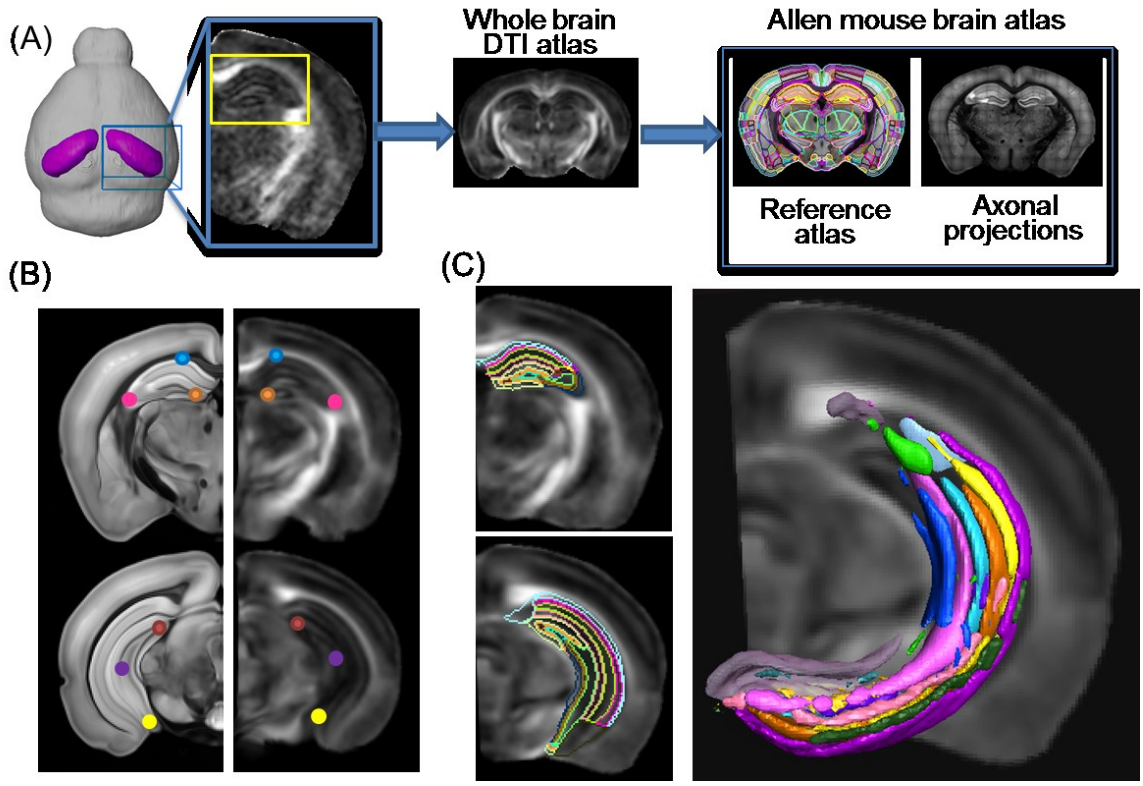

Figure 4.1: Coregistration of the diffusion MRI and the Allen mouse brain reference atlas (AMBA). (A) The image registration pipeline: the localized HARDI images were aligned to a whole brain mouse brain atlas, which was first aligned to the AMBA data through a

series of linear and nonlinear image registration procedures. (B) The registration accuracy was evaluated by manually placed landmarks on AMBA and the HARDI images. (C) After the coregistration, the brain segmentation from AMBA can be transferred to the HARDI data for quantitative analysis. Only the 17 hippocampal subfield segmentation was shown here, in anterior and posterior coronal sections as well as in 3D.

4.2.4 dMRI-based tractography

The hippocampus was manually segmented using ROIEditor (www.mristudio.org). In order to obtain tractography results that best resemble the viral tracing data, we tested several approaches. Using MRtrix (142), fiber orientation distribution (FOD) at each pixel was estimated using the constrained spherical deconvolution (CSD) method (34). Both deterministic and probabilistic fiber-tracking was performed, with a step size of 0.005 mm, a minimal length of 0.5mm, and a maximum angle of 45° between steps. Tracking terminated when the FOD amplitude became less than 0.1 or 0.01, respectively, or when fibers exited the manually segmented hippocampal region. Whole hippocampus tract density images (TDIs) at a grid size of 10 μm isotropic were generated based on short streamlines (0.4 – 1 mm in length) from random seed points throughout the hippocampal region to visualize the microstructural organization in the hippocampus (131). The fiber streamlines started from specific region of interests (ROIs) as seed region, which were

defined closed to the viral tracer injection sites in the corresponding tracer experiments. The resulting seed-based probabilistic streamlines were used to generate TDIs at a grid size of 50 μm isotropic. TDIs generated from individual hippocampus were also registered to the Allen brain reference image using the same transformations used to align the HARDI datasets. The aligned TDIs were then averaged to obtain group-averaged TDIs for each particular injection site.

For each of the 17 hippocampal subfield structural delineations in the Allen brain atlas, the tracer-based projection density is defined as the fraction of tracer-projected pixels to the total number of pixels in the division. Similarly, dMRI-based projection density was calculated as the fraction of voxel with tract density greater than 0.005 to the total number of voxels in each structural regions.

4.2.5 Statistical analysis

For each injection site, dMRI-based tract density values from each hippocampal subfield structures were compared with tracer projection density metadata, which was defined as sum of detected pixels / sum of all pixels in division. Linear regression between the TDI density and tracer density was analyzed in GraphPad (http://graphpad.com), and

the goodness of fit is evaluated by R^2 and *p*-value from an F-test of the regression. The cross correlation between the 2D connectivity maps was also calculated.

4.3 Results

4.3.1 High-resolution diffusion MRI revealed microstructural organization in the mouse hippocampus

Within a localized imaging volume (as defined in Fig. 4.2(A)), *in vivo* HARDI data of the mouse hippocampus at 0.1 mm isotropic resolution displayed distinct layered organization, and the contrasts in the direction-encoded colormaps reflected the spatial arrangement of axons and dendrites in the subfields (Fig. 4.2(B-C)). These were better visualized in the track density maps (Fig. 4.2(B'-C')), such as the radiating dendritic processes in CA1- stratum radiatum (CA1-sr) and molecular layer of the dentate gyrus (DG-mo). The 3D high-resolution also facilitated reconstruction of microstructures in three dimensions simultaneously (Fig. 4.2(D-E)).

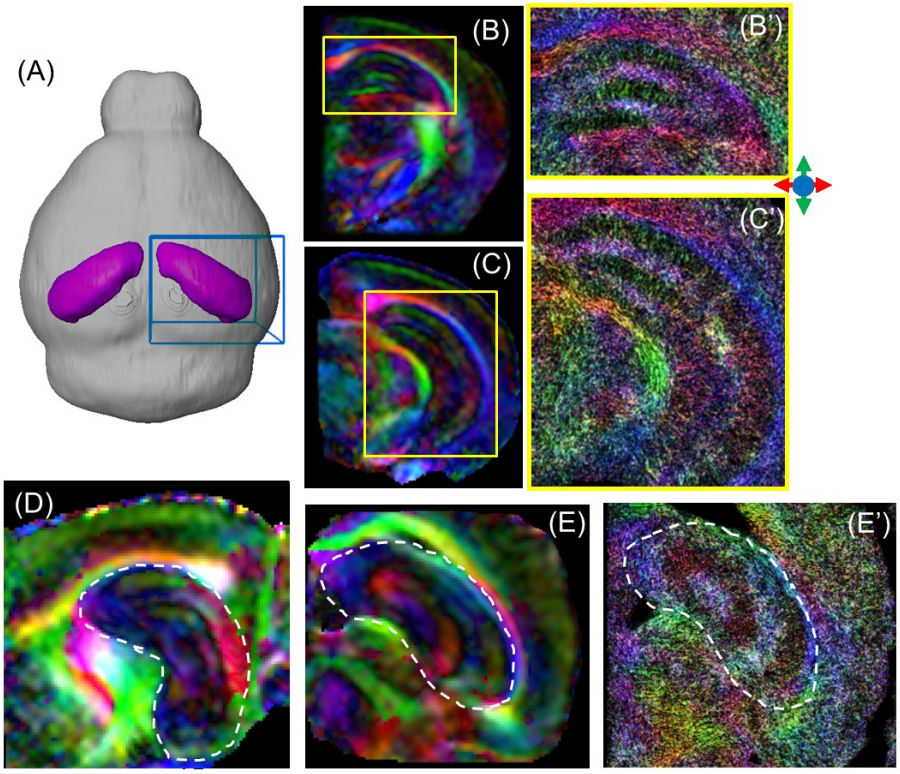

Figure 4.2: Localized 3D high-resolution diffusion MRI of the mouse hippocampus. (A) Illustration of the localized imaging volume of unilateral hippocampal field in the mouse brain. (B-C) Coronal slices of the direction encoded colormap (DEC) from diffusion tensor reconstruction showing the laminar structures in the anterior and posterior hippocampus. (B'-C') Corresponding whole brain tract-density images (TDI) showing detailed microstructures, such as the dendritic spreading in the hippocampal layers. (D-E) DEC and TDI in sagittal and horizontal views of the hippocampus, respectively.

Comparisons between fiber orientation distribution (FOD) maps computed from the HARDI data using constrained spherical deconvolution (CSD) and MAP2 and neurofilament stained histological sections further demonstrated the capability of high-resolution diffusion MRI in reconstructing the complex axonal and dendritic networks in

the mouse hippocampus (Fig. 4.3). For example, in the CA1-sr region, the radially orientated (green) FOD lobes coincided with the densely populated dendritic processes there,and the smaller mediolateral orientated (red) FOD lobes agreed with axons within the Schaffer collaterals that project inputs from CA3 to CA1. At lower spatial resolution (0.2 mm ~ 0.3 mm isotropic resolution, Fig. 4.3), the ability of diffusion MRI to resolve different network components was reduced, as the FODs became less well defined (e.g., the red FOD lobes in CA1-sr) or lost (e.g., green FOD lobes in ventral DG-mo, indicated by white arrows) at lower resolution.

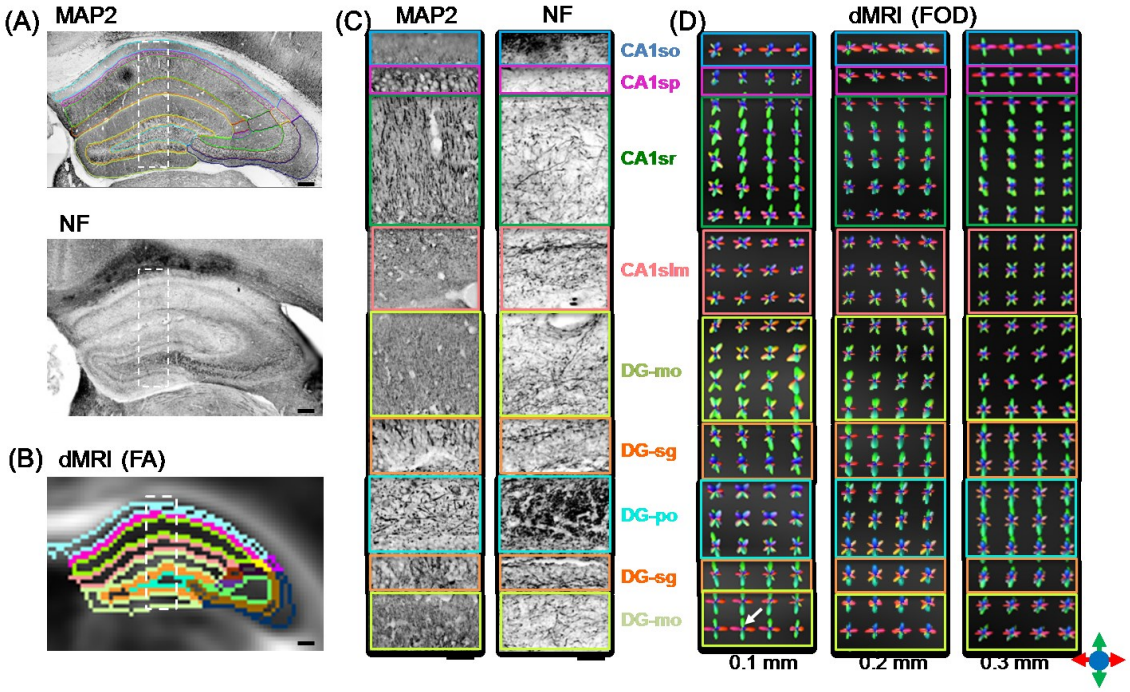

Figure 4.3: dMRI can reconstruct the organization of axons and dendrites in the mouse hippocampus. (a) Microtubule-associate protein 2 (MAP2) and neurofilament (NF) stained coronal sections (20X) of the mouse hippocampus. Scale bars = 200 um. (b) The

corresponding dMRI-derived FA image overlaid with structural boundaries in the hippocampus transferred from the Allen Mouse Brain Atlas after registration. Scale bar = 200 um. (c) Enlarged MAP2 and NF stained images from the rectangular box in (a), with various layers delineated based on the Allen Mouse Brain Atlas. Scale bars = 50 um. (d) Fiber orientation distribution (FOD) maps derived from dMRI data acquired at resolution of 0.1, 0.2, and 0.3 mm isotropic resolution (interpolated to 0.05 mm isotropic resolution for comparison). At each pixel, the size and orientation of the lobes reflects the probability of water molecule diffusion along this orientation. The color represents orientation with red for the left-right axis, green for the superior-infereior axis, and blue for the anterior-posterior axis, as illustrated by the color arrows in the lower right corner.

4.3.2 Comparison of tractography and tracer based reconstruction of the intra-hippocampal network

Comparison between tracer-labeled projection mapping images from the Allen connectivity atlas and probabilistic tractography results from the tracer injection sites showed remarkable similarity in their spatial distributions within the hippocampus. For example, tractography results generated from a CA1 seed region showed connectivity along the rostrocaudal axis within the CA1 region, which agreed with the tracer projection images (Fig. 4.4(A)). Tractography results from a CA3 seed region showed connectivity between the CA3 region and the dentate gyrus and CA1 region, as the tracer results, but less connections in the caudoventral portion. Population averaged tractography results showed that these results were consistent among different subjects (n = 7). However,

certain connections (e.g., sparsely distributed fibers in the U-shaped connections from CA3 to CA1) became attenuated after averaging, probably due to individual variations in the trajectories of these connections and residual mismatch in the registration process. The similarity was visualized in 3D (Fig. 4.4(B)) showing the probabilistic tractography performed better than deterministic tractography based on the same data and it results mostly captured the spatial distributions of tracers. At lower resolution, we found increasing mismatch between the tracer and tractography results (Fig. 4.5).

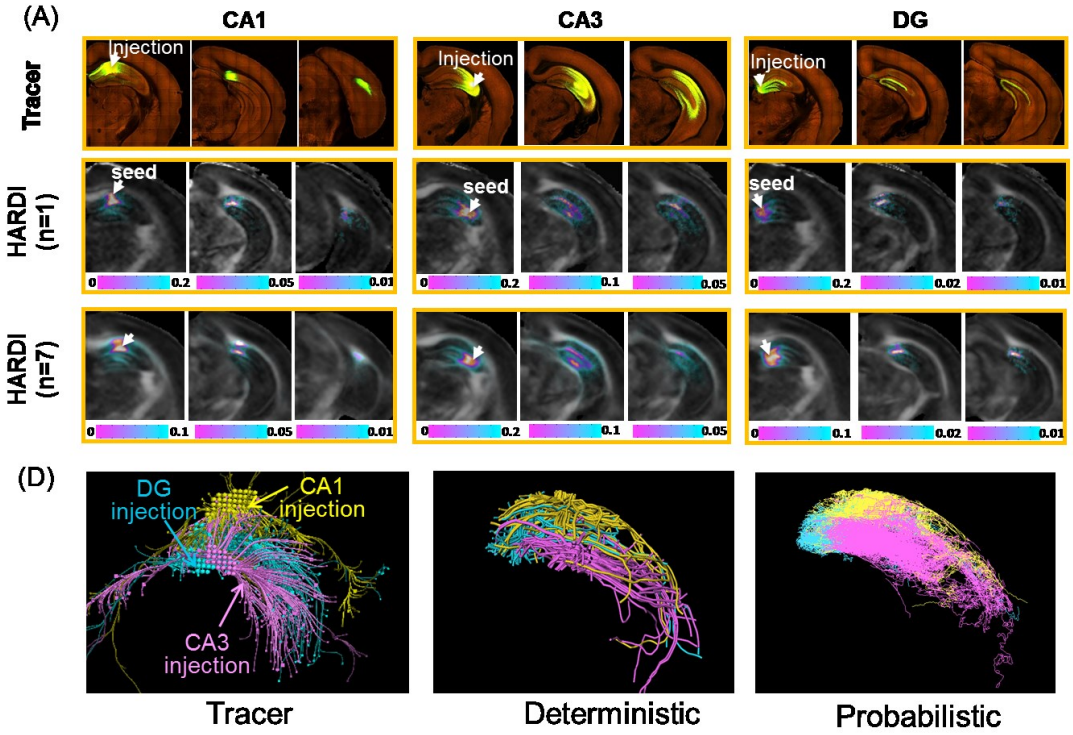

Figure 4.4: HARDI-based tractography of the mouse hippocampus. (A) Tract-density images (TDI) generated from seed regions in CA1, CA3, and dentate gyrus (DG), respectively. Top row shows the tracer projection mapping images from the Allen mouse brain connectivity atlas with injection sites in the anterior CA1, CA3, and DG (white

arrows). Both the individual subject TDIs (middle rows) and population averaged TDIs (n = 7, bottom rows) match well with the tracer projection mapping images from the Allen mouse brain connectivity atlas (top rows). The injection sites of the tracer experiments were in anterior sections of the CA1, CA3, and DG (arrows), and the corresponding TDIs were generated with fiber tracking seed regions similar to the tracer injections sites. The TDIs were overlaid on the fractional anisotropy (FA) images. (B) Three dimensional (3D) fiber tracts obtained by HARDI-based deterministic and probabilistic fiber tracking, in comparison with the tracer-based virtual tractography from the Allen mouse brain connectivity atlas. The tracer injection sites and fiber tracking seed regions were the same as that defined in (A).

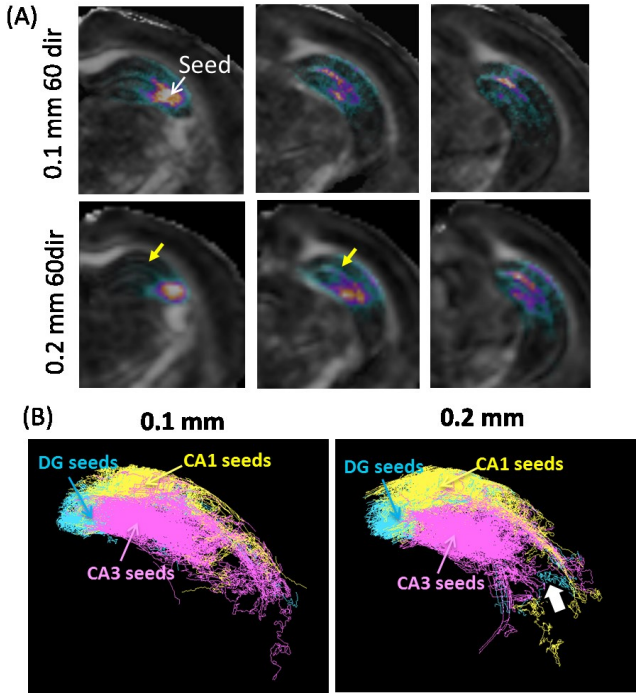

Figure 4.5: Spatial resolution of diffusion MRI is important for resolving small fiber tracts in complex microstructures. (A) TDI generated from seed region in the anterior CA3 field, using HARDI data at 0.1 mm isotropic resolution and 0.2 mm isotropic resolution, respectively. At low resolution, the connection from CA3 to CA1 is weaker (yellow arrows). (B) 3D fiber tracts reconstructed from HARDI-based probabilistic fiber tracking,

using HARDI data at 0.1 mm isotropic resolution and 0.2 mm isotropic resolution, respectively. Insufficient extension of the CA3 fiber tracts were observed at low resolution.

Fig. 4.6 displays the tractography results in sagittal planes and combines them together into the basic mouse intra-hippomcapal network. The network consists of DG fiber tracts connects the subiculum to the CA3 field in the anterior hippocampus, the CA3 fiber tracts reaching to the CA1 field, and CA1 tracts that travel posteriorly and exit through the subiculum.

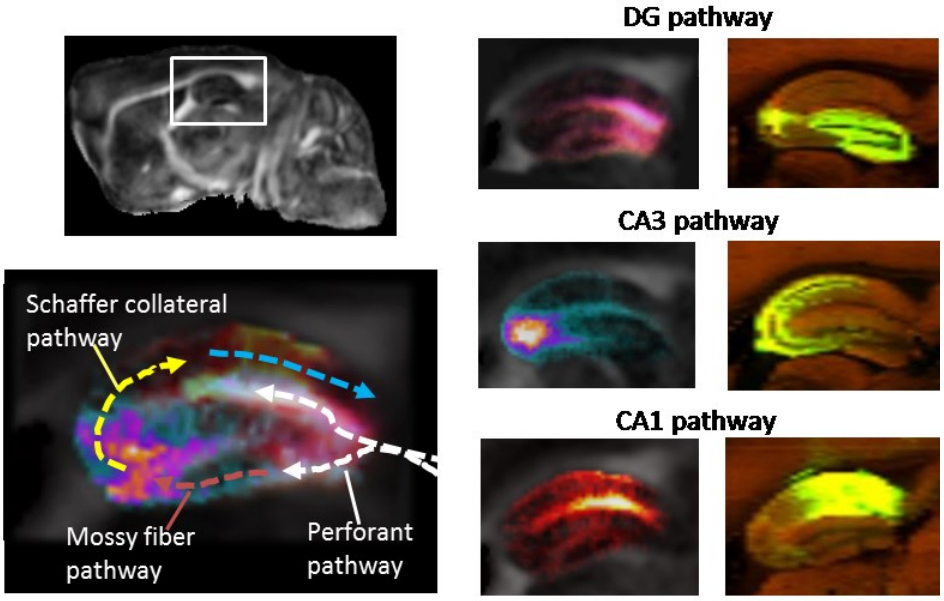

Figure 4.6: Sagittal TDI maps showing the DG pathway (pink), CA3 pathway (green) and CA1 pathway (red) and corresponding tracer projection mapping images. Integration of the three pathways revealed the classical view of hippocampal circuitry, including the perforant pathway, the Mossy fiber pathway and the Schaffer collateral pathway.

After aligning individual HARDI dataset to the Allen Mouse Brain Atlas, segmentation of hippocampal subfield defined in AMBA was transferred to the HARDI data (Fig. 4.1(D-E)) and used to examine the connectivity between different subfields based on the HARDI datasets. The similarity between the HARDI-based and tracer-based connectivity was quantitatively investigated using tractography-based projection density measure, which measures the fraction of a particular region connected to another region and was similar to the tracer-based projection density measures used by AMBA. Based on the results of eight representative tracer experiments, which had distinct injection sites across the hippocampus and injection volume within a certain range (0.3-1.3 mm^3, Table 4.1), the tractography density ($n = 5$) with tracer density showed significant correlations in all subfields ($p < 0.01$) (Fig. 4.6(A)) with the tractography results in the CA1 regions showing the strongest correlation with the tracer studies ($r^2 \geq 0.76$) and the CA3 region showing moderate correlations ($r^2 \geq 0.38$). When concatenating all the projection density data to a source / target connectivity map (Fig. 4.6(B)), we found that both tractography density and tracer density connectivity maps showed higher projection densities along the diagonals than the off-diagonals, indicating stronger connectivity between neighboring regions than distant regions. The two connectivity maps had a cross-correlation of 0.71,

but mismatches existed. For example, the spurious connection in the upper-right corner of the tractography density map indicated false positive fiber tracts.

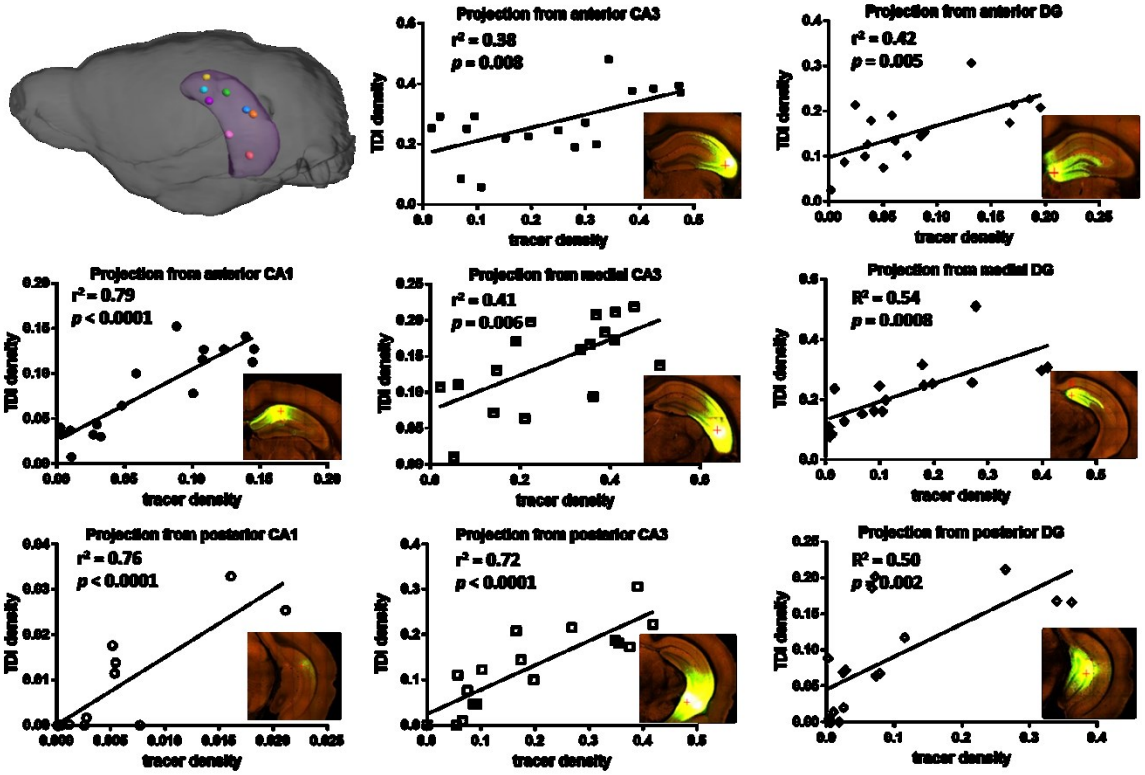

Figure 4.6: Quantitative comparisons of projection densities from the viral tracer data and the HARDI-based tractography. (A) Comparisons of eight tracer experiments with injection sites over the hippocampus and corresponding TDI datasets. In each sub-graph, the data represent projection densities in the 17 target regions of the hippocampal subfields with sources regions in the specified the injection site / seed ROI. Horizontal axis represents the projection density from TDI and the vertical axis represents the projection density from tracer data. The sources regions were chosen from eight representative sites from anterior, middle and posterior sections in CA1, CA3, and DG, which is illustrated in 3D in the upper-left inset. (B) Connectivity matrices consist of projection densities from the eight tracer data (upper panel) or TDI data (lower panel). The horizontal axis represents the target region and vertical axis represents the source region. The projection densities was normalized to 0-1 for each row. The two connectivity matrices shares similarity with

a correlation coefficient of 0.71. The dashed diagonal lines indicates strong connections along the diagonals.

Table 4.1: Usage of the Allen mouse brain connectivity atlas data. All tracer experiments with injection sites in the hippocampus are listed here. Eight representation datasets were used in this study to compare with diffusion MRI tractography. The other datasets were not used due to inappropriate injection volume or the injection sites are similar to one of the eight datasets.

ID	Injection	Coordinates	Inje	Used	Note
1001478	CA1	[7500, 1600,	0.07	Yes	
1169007	CA1	[7500, 1700,	0.16	No	Inj site
1204362	CA1	[7000, 1900,	0.12	No	Inj site
1204947	CA1	[7800, 2000,	0.01	No	Inj volume
1001484	CA1	[9100, 3300,	0.03	Yes	
2724047	CA3	[7400, 2600,	0.12	Yes	
1127450	CA3	[7100, 2500,	0.03	No	Inj volume
1139352	CA3	[8200, 4200,	0.29	No	Inj volume
1805237	CA3	[7200, 2600,	0.01	No	Inj volume
1123084	CA3	[7700, 3300,	0.09	Yes	Inj site
1144293	CA3	[7800, 3200,	0.18	No	Inj site
1276490	CA3	[8100, 4900,	0.54	Yes	
1001481	DG	[6800, 2700,	0.08	Yes	
1001412	DG	[6900, 2800,	0.13	No	Inj site
2729700	DG	[6400, 2700,	0.00	No	Inj volume
1127457	DG	[8000, 2400,	0.05	Yes	
1140082	DG	[8300, 2500,	0.06	No	Inj site
1121673	DG	[7900, 2400,	0.02	No	Inj site
1126722	DG	[8900, 4000,	0.07	Yes	
1144300	DG	[8400, 3300,	0.10	No	Inj site
1131660	DG	[8900, 4600,	0.13	No	Inj site

4.4 Discussion

Recently advances in diffusion MRI and tractography techniques have brought promise to examine brain connectivity at increasingly smaller scales. The advantages of diffusion MRI include the ability to examine multiple networks in the same brain as well as its potential to translate into the clinics. The biological relevance of diffusion tractography in major white matter fibers has been investigated with histological evidences (38,39,192). The validation is more difficulty for tractography in grey matter structures, especially with of probabilistic fiber tracts (193). The intra-hippocampal connectivity is important for us to understand the structural and functional organization of the hippocampus. Current knowledge on intra-hippocampal connectivity in the mouse was mostly obtained from extensive tracer-based studies, which offer superior image resolution and high specificity and the possibility to reconstruct the 3D trajectories (187). This extensive knowledge make it possible to study the role of intra-hippocampal connectivity in several neurological diseases that involves the hippocampal circuitry, such as the Alzheimer's disease (194,195), stroke, and hippocampal sclerosis (196). Combing the existing knowledge from tracer-based study with state-of-the-art diffusion MRI techniques

could potentially open new ways to investigate the integrity of intra-hippocampal networks, their longitudinal changes after diseases onsets and after treatments.

In this study, we use high-resolution diffusion MRI and tractography to examine intra-hippomcapl network in the mouse brain. Previous studies have stressed the importance of spatial and angular resolution. Using a localized imaging approach, we have achieved both high spatial and angular resolution (0.1 mm isotropic resolution and 60 directions in 2 hours). The high spatial and high angular resolution dMRI data acquired with this approach not only allowed delineation of the hippocampal microstructure and laminar organization (Fig. 4.3), but also facilitated image registration and improved the fiber tracking results (Fig. 4.7). Even though super-high resolution diffusion MRI data can be acquired from post-mortem brain specimen (81,197), neither the *ex vivo* imaging techniques nor the tracking results may be directly translatable to *in vivo* study. In addition to the improvement on resolution, we optimized the fiber tracking algorithms and parameters to reproduce connectivity patterns comparable to the tracer studies. HARDI-based probabilistic fiber tracking performed well in resolving the branching fibers in the grey matter layers of the hippocampus, with fine-tuned tracking parameters (data not provided).

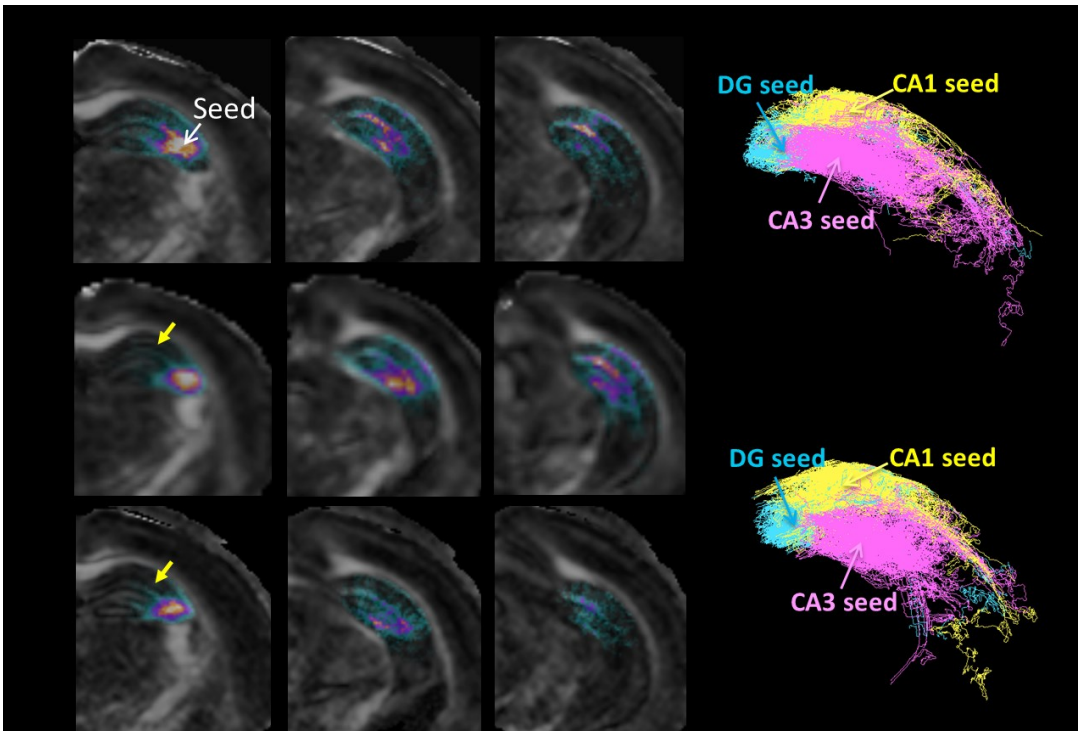

Figure 4.7: Effects of spatial and angular resolution in tractography. (A) TDI maps from a anterior CA3 seed region, generated with HARDI data acquired at 0.1 mm (top row) and 0.2 mm (middle row) isotropic resoltion and 60 diffusion directions, and 0.1 mm isotropic resolution and 30 diffusion directions (bottom row). (B) Probabilistic fiber tracts from CA1, CA3, and DG seed regions, generated with HARDI data acquired at 0.1 mm (top row) and 0.2 mm (bottom row) isotropic resoltion and 60 diffusion directions.

In order to correlate the dMRI tractography with histological evidence, we developed an image processing pipeline to compare the probabilistic tractography with the Allen mouse brain connectivity atlas. Both the visual comparisons of the 2D projection maps and 3D tractography (Fig. 4.4), and the quantitative comparison of the projection density (Fig. 4.6) demonstrated the similarity between the HARDI-based and tracer-based connectivity.

While the major pathways were successfully reconstructed, differences were also identified, e.g. the lack of CA3 to CA1 connections in anterodorsal CA1 region (Fig. 4.4(A)) and the relatively low correlation between tracer density and TDI density from the CA3 seed region (Fig. 4.6(A)). The mismatch may result from dominance of dendritic processes in CA1-sr as suggested in the MAP2 staining (Fig. 4.3), such that CA3 to CA1 Shaffer collaterals were not easily tracked. Also, false positives in the TDI connectivity map can be found between distantly connected regions, compared to the tracer connectivity map (Fig. 4.6(B)). One possible factor leading to the false positive is that the viral tracer used in the Allen connectivity atlas is an anterograde tracer that crosses single synaptic connection, whereas dMRI-based fiber tracking is bi-directional and not restricted by the number of synaptic connections.

Several important connections were closely examined (Fig. 4.5). 1) In the CA1 field, it is known that axons originated from the pyramidal cells of CA1 primarily project to the subiculum. This pathway is robustly captured. 2) The collateral fibers, arising from the CA3 pyramidal cells play an important role of distributing fibers across CA3, CA2, and CA1 fields and also innervating the polymorphic layer in DG. Majority of the CA3-to-CA3 associational connections and CA3-to-CA1 Shaffer collaterals are confined in the stratum

radiatum. Using HARDI-based probabilistic fiber tracking, we roughly traced these pathways, but the CA3-to-CA1 connection could not sufficiently extend to anterodorsal CA1. 3) The dentate gyrus receives inputs from the enterohinal cortex and send projections to the CA3 field through the mossy fibers, along with the associational fibers that transverse longitudinally (178). Our tractography results indicated the DG fibers run antero-posteriorly, and some of those fibers spread to the CA3 field. 4) The innervation patterns of the CA1, CA3 and DG fibers give rise to the trisynaptical pathway (part of the perfront pathway), namely the DG-CA3-CA1 connection. TDI maps of this pathway is fairly close to the underlying anatomy.

Although the general validity of diffusion tractography is still under investigation (198), our investigation on mouse hippocampus circuitry suggests to dMRI can be a promising tool to perform "*in vivo* histology" of the brain connectivity. As the MR technology continue to advance, e.g., high magnetic field and gradient strength in human scanners, the high-resolution dMRI as performed in this study would be readily translatable to image the human brain connectivity.

4.5 Conclusion

We proposed a localized imaging technique to obtain high-resolution dMRI of the mouse hippocampus, together with an image processing pipeline for quantitative mapping of the intrinsic hippocampal connectivity *in vivo*. The major connections in the hippocampal circuitry are reconstructed with high-fidelity to the Allen mouse brain connectivity atlas, with limitation in recovering long distance connections.

Chapter 5 *In Utero* Localized Diffusion MRI of the Embryonic Mouse Brain Microstructure and Injury

5.1 Introduction

During embryonic and fetal development, the brain undergoes rapid growth, including formation of basic functional units and critical neural circuitry. Injuries during this critical period often have profound impacts on brain structures and functions at later stages. For example, intrauterine inflammation is one of the common causes of preterm birth, with adverse neurological outcome (199). Fetal brain magnetic resonance imaging (MRI) is emerging as a promising tool to study brain development (58,59) and to detect fetal brain injury (60-63). Compared to other imaging modalities, primarily ultrasound, MRI provides rich tissue contrasts for delineation of fetal brain structures and injuries. Once abnormalities are detected by ultrasound, MRI is the technique of choice in the clinic to establish the pattern of injuries (200).

Compared to conventional T_1/T_2 MRI, diffusion MRI (dMRI), especially diffusion tensor imaging (DTI) (70,201), is well suited for characterization of the fetal brain

structures and injuries because its contrasts reflect the organization of brain microstructures and are less dependent on myelin content (70,202). Its unique ability in characterizing developing grey and white matter structures has been established by studies of postmortem fetal brain specimens (203,204) as well as preterm babies and infants (156,205). Several groups pioneered in *in utero* dMRI of the human fetal brain (206-210) to evaluate normal and abnormal fetal brain development.

To realize the full diagnostic potential of *in utero* fetal brain dMRI, it is important to understand the relationships between tissue microstructural changes and their manifestation in diagnostic markers. The laboratory mouse provides a convenient vehicle to examine these relationships as it is commonly used to study the dynamics of mammalian brain development and pathogenesis. In addition, the existence of a large repertoire of genetically modified mouse strains further facilitates the investigations of the genetic mechanisms controlling brain development and responses to injuries. MRI has been used to examine the embryonic mouse brain, but mainly in post-mortem specimens. Several groups demonstrated three-dimensional (3D) T_1- and T_2-weighted MRI of *ex vivo* embryonic mouse brains with spatial resolutions up to 20 μm (113,115,211), and *ex vivo* DTI of embryonic mouse brain with superb tissue contrasts and resolutions up to 50μm

(130,212). Despite the advances in *ex vivo* dMRI of the mouse brain, there is no substitute for *in vivo* MRI as death and chemical fixation inevitably alter tissue microstructural properties (213,214) and MR signatures of key pathological events, such as edema, may not be preserved in *ex vivo* specimens (215,216).

In utero MRI of the live mouse embryos is extremely challenging due to motions from both the embryo and maternal mice and limited signal-to-noise ratio (SNR). Moreover, high resolution in all three dimensions is often required to resolve structures within the miniature brains (< 6 mm in any dimensions). Only recently, Turnbull and colleagues demonstrated successful *in utero* embryonic mouse brain T_1-weighted MRI using advanced motion correction techniques (217,218). Compared to conventional T_1/T_2 MRI, dMRI is known to be particularly sensitive to motion, and the application of the diffusion gradients further reduces SNR. Due to these technical challenges, feasibility of *in utero* dMRI embryonic mouse brain has not been reported.

In this study, we explored the feasibility of *in utero* dMRI of the embryonic mouse brain using a localized imaging approach with spatially selective excitation pulses (219,220), which were designed based on a linear class of large tip-angle (LCLTA) pulses (221). The localized imaging strategy is advantageous because a pregnant mouse has

multiple embryos, each located within its own gestational sac inside the uterus and occupies only a small portion of the maternal body. Localization can significantly reduce the field-of-view, and therefore shorten the imaging time and reduce susceptibility to motion. Combined with a 3D fast imaging sequence and motion correction techniques, our goal was to perform *in utero* dMRI of the embryonic mouse brain and use the technique to study microstructural features during brain development and injury.

5.2 Materials and Methods

5.2.1 Animal Preparation

All experimental procedures were approved by the Animal Use and Care Committee at the Johns Hopkins University School of Medicine. Pregnant CD-1 mice (Charles River Laboratories) with an average littler size of 11 pups (19 days on full-term gestation) were used in this study. Among them, three pregnant dams were subjected to a model of intrauterine inflammatory according to previous studies (222-224). Briefly, on gestational day 10 (embryonic day 17, or E17), timed pregnant mice were placed under isoflurane anesthesia and a mini-laparotomy was performed. Lipopolysaccharide (LPS, Sigma, St. Louis, MO, Lot. 102M4017V) 50μg in a 100μl phosphate buffer solution (PBS) was

infused between 2 gestational sacs in the lower right uterine horn. Routine closure was applied and the dams were recovered in individual cages. Control mice were gestational age-matched pregnant dams without surgery.

Imaging was performed on normal pregnant mice (n = 10) and injured mice 6 hrs after injection of LPS (n = 3). During imaging, pregnant mice were anesthetized with isoflurane (1%), together with air and oxygen mixed at a 3:1 ratio, via a vaporizer. Respiration was monitored via a pressure sensor (SAII, Stony Brook, NY, USA) and maintained at 30–60 breaths per minute. Among the ten normal mice, five received gadopentetate dimeglumine (Gd-DTPA, Magnevist, Berlex Imaging, Wayne, NJ) at a dose of 0.4 mMol/kg via intraperitoneal injection (i.p.) injection at the lower abdomen at approximately 2 hrs before MRI.

5.2.2 Pulse sequences for single and multi-FOE localized MRI

Localized imaging targeting a selected mouse embryo was achieved using two-dimensional spatially selective 90° excitation pulses, calculated based on a linear class of large tip-angle (LCLTA) pulses (221) as described in Chapter 3.2.2. The pulses were designed to excite a rectangular field of excitation (FOE) in the x–y plane that covered the

target embryonic mouse brain, with a pulse duration of 3 ms and pulse amplitude of 9-10 μT. We used a 12-turn spiral-in excitation k-space (maximum gradient strength of 148 mT/m), which resulted in an excitation resolution of 1.5 × 1.5 mm. A slab-selective refocusing pulse (136) were applied to restrict the imaging slab in the z direction. The selective excitation pluses were combined with a house-made 3D diffusion-weighted gradient spin-echo sequence (DW-GRASE) (176,212) with an echo train length of 20 for fast imaging (Fig. 5.1(B)). Twin navigator echoes (225) were appended after the imaging echoes to correct phase errors due to motion and instrument instability. Respiratory triggering was not used.

This localized imaging module can be replicated for simultaneous acquisition of multiple embryonic mouse brains in an interleaved fashion. As illustrated in Fig. 5.1(A), two different selective excitation pulses and signal acquisitions were evenly spaced in each repetition time (TR). An example of multi-FOE imaging is demonstrated in Fig. 5.2(A). If the two FOEs do not overlap in the x, y, and z directions, multi-FOE imaging with 2D selective excitation pulses can be achieved with minimal interferences between them. With this approach, the idle time in TR was utilized to improve the efficiency, and a longer TR

became afforded in the 3D acquisition to enhance the SNR as well as contrast in T_2-weighted images.

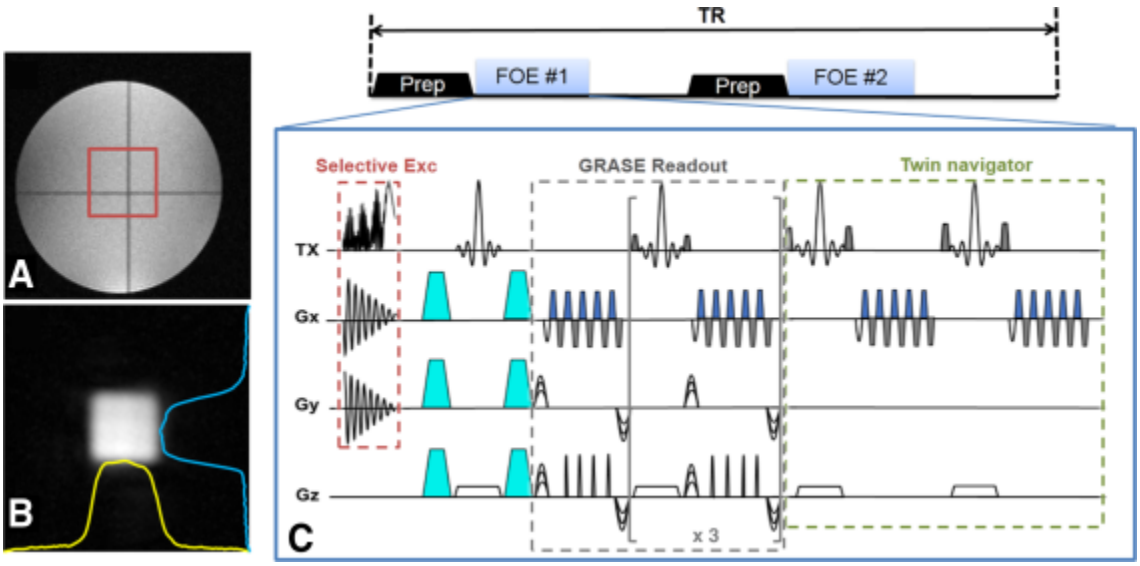

Figure 5.1: Use of selective excitation pulse and a 3D diffusion-weighted gradient spin-echo sequence (DW-GRASE) sequence for localized diffusion MRI. (A) Performance of the spatially selective excitation pulse was tested in an agarose gel phantom. The red box in the image of the phantom represents an 8 × 8 mm field of excitation. The yellow and blue curves in (B) show the excitation profile along the x-axis and y-axis, respectively. (C) A diagram of the 3D DW-GRASE sequence with spatially selective excitation pulse. The sequence can be extended to include two fields of excitation and acquisition. The diagram shows two localized imaging modules that target two separate embryos in an interleaved fashion. The localized imaging module is expanded to show the timing of the 2D selective excitation pulse together with the spiral gradient in the x–y plane, diffusion sensitization, the GRASE readout, and the twin-navigator echoes. Each GRASE readout acquires five double-sampled gradient and spin echoes and is repeated four times to achieve an acceleration factor of 20 compared to the conventional spin echo sequence.

5.2.3 Image acquisition

In vivo imaging was performed on a horizontal 11.7 Tesla MR scanner (Bruker Biospin, Billerica, MA, USA). Radio frequency (RF) pluses were transmitted through a 72 mm diameter quadrature volume coil, and signal was acquired using either an 8-channel phased array rat body coil or a 15 mm diameter planar surface receive-only coil, which was placed directly on the mouse abdomen to maximize sensitivity (Bruker Biospin, Billerica, MA, USA).

To locate the target embryo, coronal and sagittal multi-slice T_2-weighted images of full coverage were acquired (echo time (TE)/TR = 50/3000 ms, in-plane resolution = 0.16 mm x 0.16 mm, slice thickness = 1 mm, and scan time ≈ 8 min) as the reference images to define the target embryo and corresponding FOE. The 8-channel phased array rat body coil covered the entire abdomen and was used to acquire 0.2 mm isotropic resolution dMRI with TE/TR = 21/1000 ms, two non-diffusion-weighted (b0) images and six diffusion-weighted images (b = 800 s/mm^2) in 34 mins. The same parameters were used for multi-FOE imaging and imaging of the injured embryonic mice from the intrauterine inflammation model. The 15 mm planar surface coil provided limited coverage but higher sensitivity than the body coil and was used for high resolution DTI with the following

parameters: TE/TR = 21/500 ms; two signal averages; spectral width = 120 kHz; four b_0 images and 30 diffusion directions (226); b-value = 1000 s/mm^2; field of view (FOV) = 12.8 mm x 12.8 mm x 8 mm; and spatial resolution = 0.2 mm x 0.2 mm x 0.2 mm in 72 min (n = 5) (2 min per diffusion direction) or 0.16 mm x 0.16 mm x 0.16 mm in 113 min (n = 1). High resolution 3D T_2-weighted b_0 images were acquired with a TR of 1000 ms at 0.13 x 0.13 x 0.13 mm resolution in 9.6 min.

Ex vivo imaging was performed on the dissected embryonic mouse brains (n = 5) from the maternal mouse. The brain specimens were immersion fixed in 4% paraformaldehyde (PFA), and later transferred to PBS with 2 mM Gd-DTPA. Specimens were scanned using a vertical 11.7 Tesla NMR spectrometer (Bruker Biospin, Billerica, MA, USA) and a birdcage volume coil (10mm inner diameter). We used similar imaging parameters as those in the *in vivo* dMRI, except a higher b-value was used to compensate the reduced diffusivity in *ex vivo* samples (b-value = 1500 s/mm^2). Temperature was maintained at 37° during the scan.

5.2.4 Image Processing

The 3D k-space data were apodized with a tapered cosine window, zero-padded to twice of the original size, and reconstructed in Matlab (Mathworks). The twin-navigator echoes were Fourier transformed along readout direction, which were then used to align the phases of the odd- and even-numbered spin echoes from each repetition (212). The 30 diffusion-weighted images (DWI) were aligned to the mean DWI using 3D rigid transformation to correct the inter-scan motion. Diffusion tensor fitting were performed in DtiStudio (www.mristudio.org) using log-linear fitting, and fiber tracts were obtained with a FA threshold of 0.15 and maximum angle of 60^0. Spherical deconvolution of the 30 direction dMRI data was performed in MRtrix (142) with a harmonic order of six to generate the fiber orientation distribution (FOD) map. Quantitative analysis of the fractional anisotropy (FA) and apparent diffusion coefficient (ADC) was performed in ROI Studio. The SNR was calculated as the ratio of the mean of a single b0 image to the standard deviation of the subtraction image between two b0 images in a cortical region of interest (ROI) that was close to the coil. The contrast-to-noise ratio (CNR) was calculated as the difference in SNR between two ROIs.

5.2.5 Histo-pathological Examination

Following MRI acquisition, embryos were taken out and whole heads were fixed in 4% PFA at 4℃ overnight. The next day, specimens were washed with PBS extensively and immersed in 30% sucrose until saturation, followed by cryosection at 20μm thickness and histochemical staining. Routine Nissl and Hematoxylin and eosin (H&E) stainings were performed to evaluate the morphological change of the injured fetal brains. All photographs used for quantification were taken with Zeiss AxioPlan 2 Microscope System (Jena, Germany) attached to a Canon EOS Rebel Camera (Tokyo, Japan) with a 4X objective.

5.3 Results

On gestational day 17, a large portion of the abdominal space was occupied by more than ten embryos in its uterus, each located within its own gestational sac in the maternal uterus (Fig. 5.2(A)). Using an 8-channel phased array body coil, multi-slice T_2-weighted images of the entire mouse abdomen were captured to locate each individual embryos and to define fields of excitation (FOEs) for selected embryos. For example, in Fig. 5.2(A), two FOEs in the size of 10 mm x 10 mm x 8 mm (yellow and blue boxes), each containing the head of a selected embryo, were defined based on the T2-weighted images. The generated

selective excitation pulses provided uniform excitation within the FOEs and suppressed signals from tissue outside the FOEs (Fig. 5.2(B)).

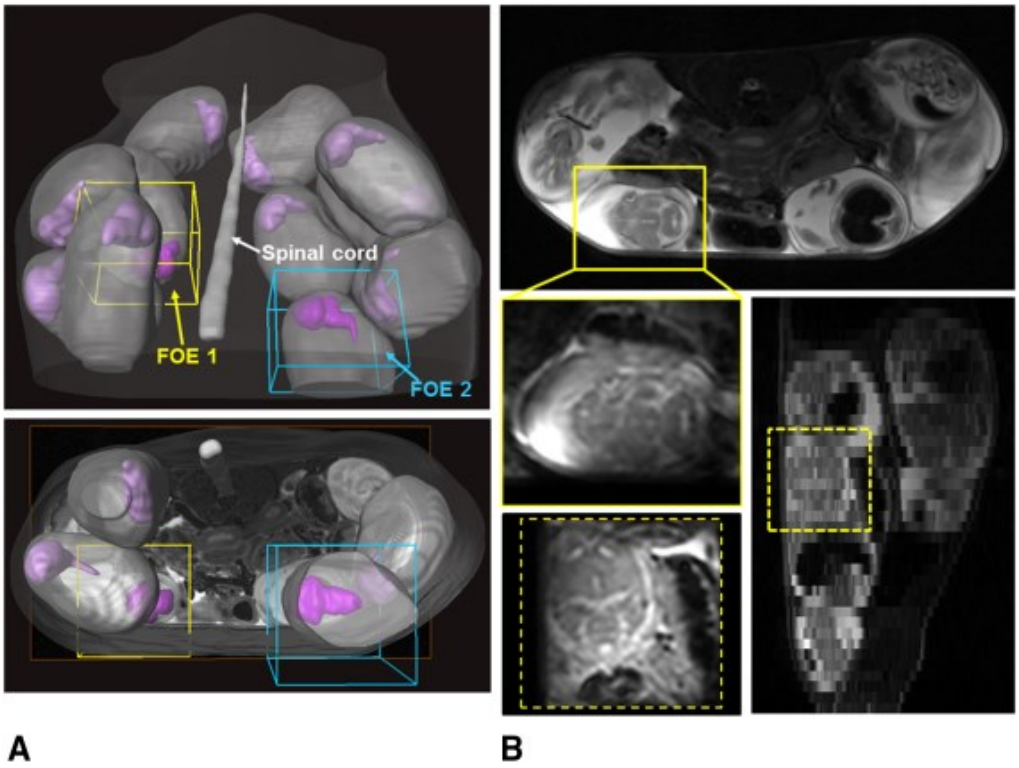

Figure 5.2: Mouse embryos in the abdomen of a pregnant CD-1 mouse on gestational day 17 localized with selective excitation pulses based on user-defined FOEs. (A) 3D rendering of 11 mouse embryos in the uterus, reconstructed based on multislice T2-weighted images. The yellow and blue boxes indicate the FOEs for two embryonic mouse brains used in twin-FOE imaging. (B) A selected embryonic mouse brain defined in coronal and sagittal multislice T2-weighted images of the mouse abdomen (corresponding to FOE1 in (A)). 3D T2-weighted images of this embryonic mouse brain acquired using the GRASE sequence with selective excitation show minimal aliasing.

With the twenty-echo DW-GRASE sequence, a single 3D diffusion weighted image at 0.2 mm isotropic resolution could be acquired in 2 minutes. Motion during the 2 minute

period could be corrected using the twin navigator echoes, which reduced the motion-induced smearing in both non-diffusion weighted (Fig. 5.3(A)) and diffusion-weighted (Fig. 5.3(B)) images. Motions between images, from both the mother and embryos, could be corrected by post-imaging registration (Fig. 5.3(C)). Based on the rigid registration results, the overall movements of the embryonic mouse brains were estimated and plotted over time (Fig. 5.3(D)). The average translational motion during a one-hour period was 0.18 ± 0.09 mm (the maximum motion was 0.60 ± 0.46 mm, n=5). Fig. 5.4 shows mean DWI and ADC maps from two mouse embryos acquired simultaneously from the two FOEs defined in Fig. 5.2.

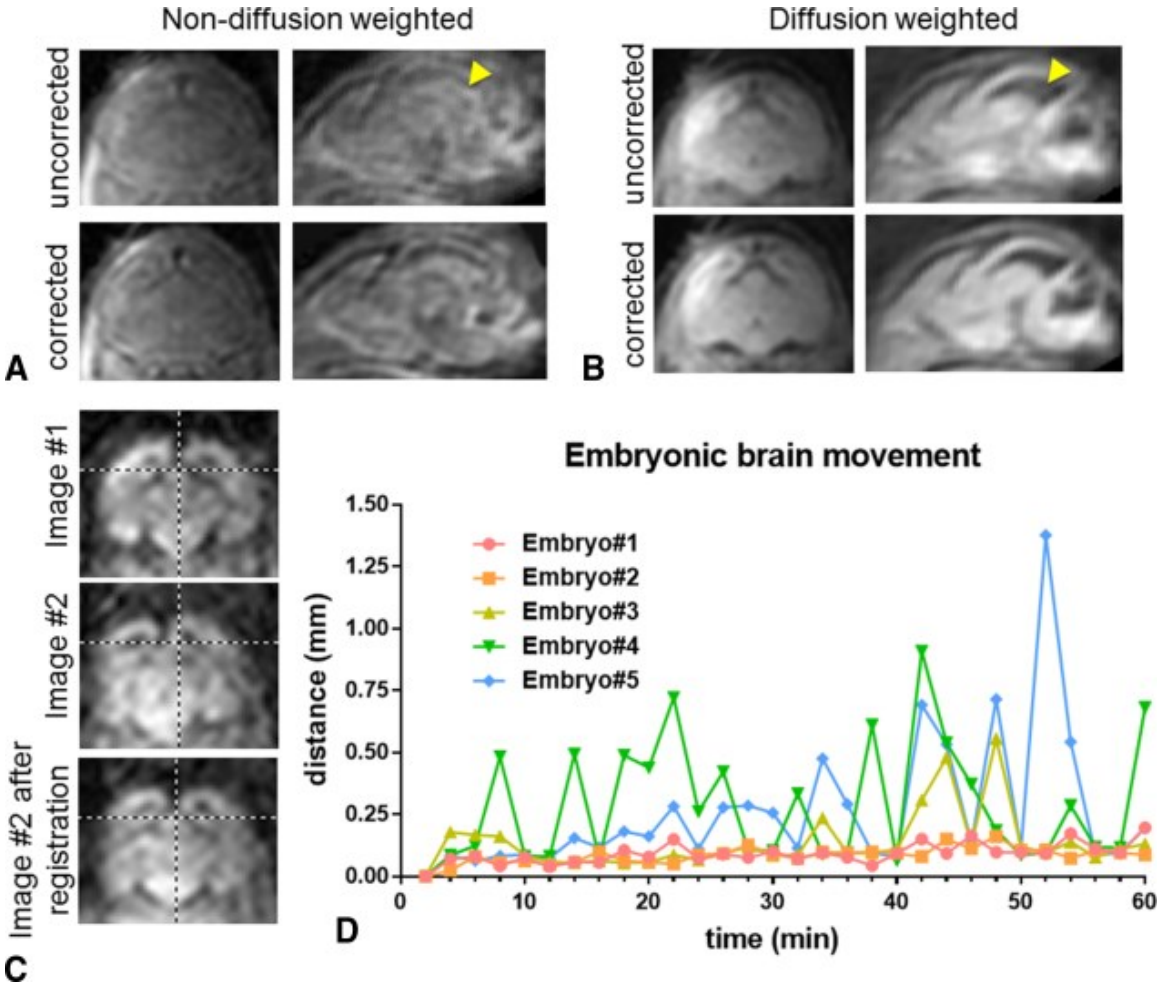

Figure 5.3: Motion correction based on twin-navigator echo phase correction and retrospective image registration. Navigator echo phase correction improves image quality by removing motion artifacts, eg, smearing of structural boundaries (indicated by the arrowheads), in both nondiffusion-weighted images (A) and diffusion-weighted images(B). Rigid image registration corrects motion-induced misalignment between images. For example, mismatch between Image #1 and Image #2 can be corrected after registration (C). (D) Translational motions of five embryonic mouse brains were estimated based on rigid transformations and plotted over a 1-hour period. Horizontal axis denotes scan time in minutes, and vertical axis denotes the translational movements in mm.

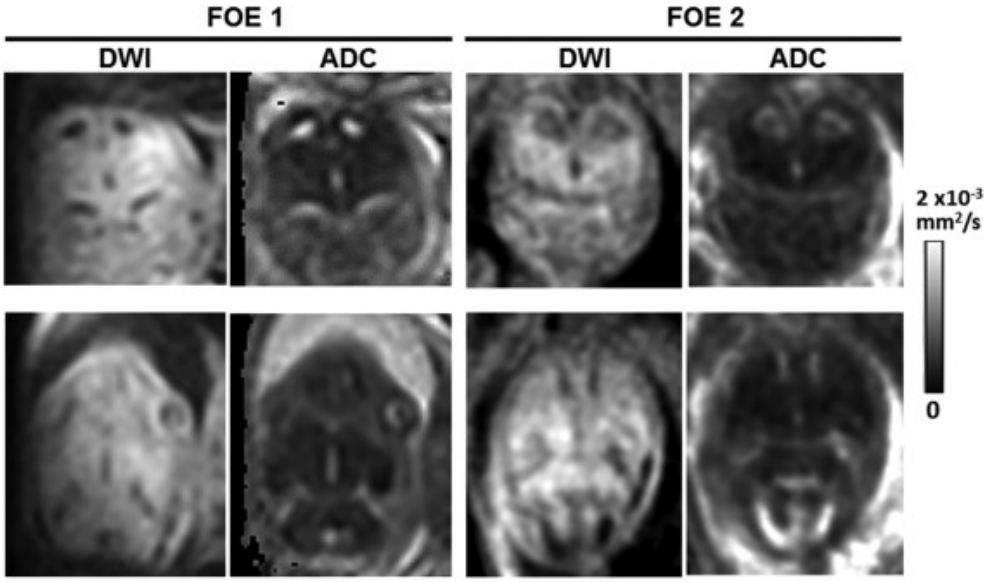

Figure 5.4: DWI and ADC maps acquired simultaneously from two embryonic mouse brains, as defined in Fig. 2A, using the multiple FOE acquisition technique.

Further improvement in image resolution and contrast was achieved by using high sensitivity planner surface coil and injection of Gd-DTPA. In our study, at two hours after i.p. injection of Gd-DTPA, signal enhancement could be observed in the mouse embryos and persist for more than two hours. With Gd-DTPA, the SNR measured in the parenchyma increased 1.7 times compared to that without Gd-DTPA (26.1 ± 4.3 (*n*=5) versus. 15.3 ± 4.4 (*n*=3)), and the contrast to noise ratio between the CSF and brain parenchyma increased 1.9 times (7.07 ± 1.31 (*n*=5) versus 3.66 ± 0.63(*n* = 3)). Taking advantage of the high SNR, T_2-weighted image of the embryonic mouse brain could be acquired at 0.13 mm isotropic resolution within 10 minutes, which was sufficient to define the overall brain morphology

in 3D. For example, the ventricular system in the embryonic mouse brain can be outlined in 3D (Fig. 5.5(A)).

Diffusion tensor data at 0.2 mm isotropic resolution and 30 diffusion encoding directions could be acquired in 72 minutes. In the FA and direction-encoded colormaps (Fig. 5.5(B)), major grey matter and white matter structures in the E17 mouse brain could be delineated. The cortical plate and intermediate zone could be separated by their unique tissue orientations. Several white matter tracts, e.g., the cerebral peduncle (cp), optical tract (opt), and fimbria (fi), could also be identified based on their high FA values and orientations. The *in vivo* DTI results were compared with *ex vivo* data acquired at the same resolution (Fig. 5.5(C)). Changes in overall brain morphology were observed between the *in vivo* and *ex vivo* embryonic brains, e.g., flatter brain shape and shrunk ventricles, but tissue contrasts remained mostly unchanged. *In vivo* ADC measured in both grey and white matter structures were significantly higher than *ex vivo* (temperature kept at 37 °C). In comparison, *in vivo* FA values in most regions, except the intermediate zone, did not show significant difference (Table 5.1). The results are consistent with the previous findings in the adult mouse brain (213,214).

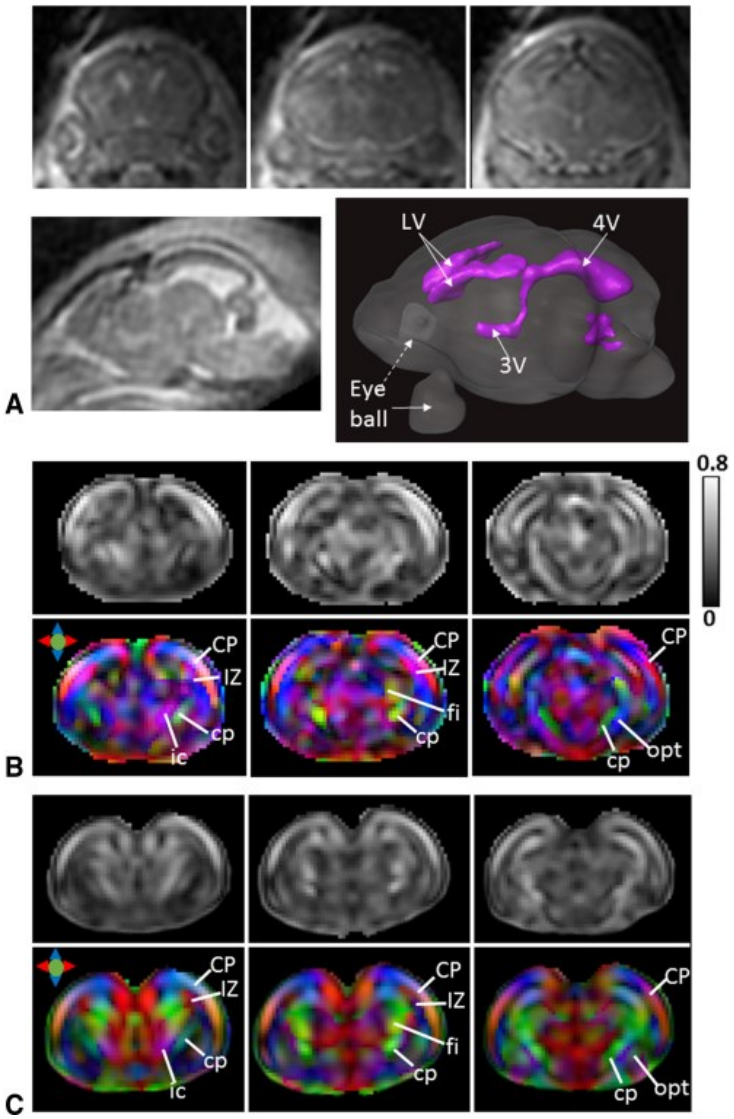

Figure 5.5: (A) T2-weighted images of an embryonic mouse brain acquired at 0.13 mm isotropic resolution. The ventricles were reconstructed in 3D based on the high-contrast T2-weighted images. (B) *In vivo* DTI of an E17 embryonic mouse brain at 0.2 mm isotropic resolution, in comparison with *ex vivo* DTI result (C) at the same resolution. Several gray and white matter structures in the E17 mouse brain can be delineated in the FA maps (top rows) and direction-encoded colormaps (bottom rows), eg, the cortical plate (CP), intermediate zone (IZ), cerebral peduncle (cp), internal capsule (ic), optic tract (opt), and fimbria (fi).

Table 5.1: Apparent diffusion coefficient (ADC) and fractional anisotropy (FA) of several grey and white structures measured from the *in vivo* and *ex vivo* E17 embryonic mouse brains (n = 5). Data is presented as mean ± standard deviation across subjects. * and ** denote that a two-tailed t-test between the *in vivo* and *ex vivo* measurements produced a p-value less than 0.01 and 0.001, respectively. Abbreviations: CP - cortical plate; IZ - intermediate zone.

Structures	ADC ($x10^{-3}$ mm^2/s)		FA	
	In vivo	*Ex vivo*	*In vivo*	*Ex vivo*
Frontal CP	0.65±0.09	0.47±0.02*	0.41±0.11	0.42±0.02
Temporal CP	0.59±0.05	0.45±0.03**	0.39±0.06	0.33±0.03
IZ	0.64±0.10	0.39±0.03**	0.44±0.07	0.24±0.02**
cerebral peduncle	0.67±0.07	0.31±0.03**	0.34±0.05	0.30±0.07
optical tract	0.77±0.10	0.33±0.03**	0.31±0.07	0.29±0.03
fimbria	0.57±0.10	0.40±0.02*	0.35±0.07	0.35±0.04
internal capsule	0.54±0.08	0.38±0.04*	0.37±0.05	0.33±0.07

Fig. 5.6 demonstrates diffusion tensor data of an E17 mouse brain acquired at 0.16 mm isotropic resolution in 2 hours. Compared to the images at lower resolution, several white matter structures, e.g. the fimbria (fi) and the cerebral peduncle (cp), could be more easily resolved. The *in vivo* DTI results were similar to *ex vivo* at the same resolution, but less sharp than the *ex vivo* DTI at 0.1 mm isotropic resolution (Fig. 5.6(C)), which was acquired in 4hrs. The microstructural organization of embryonic mouse cortex could be visualized using spherical deconvolution (142) of the 30 direction diffusion data. The cortical plate

showed dominant radial orientation, probably due to the presence of radial glial fibers, and the intermediate zone beneath it showed two fiber groups crossing each other. Major white matter tracts, e.g., the cerebral peduncle (cp), optical tract (opt), and stria terminalis (st), could be reconstructed in 3D and visualized in relation to gray matter structures, such as the cortical plate (CP), hippocampus (Hi), and thalamus (Th) (Fig. 5.6(C)).

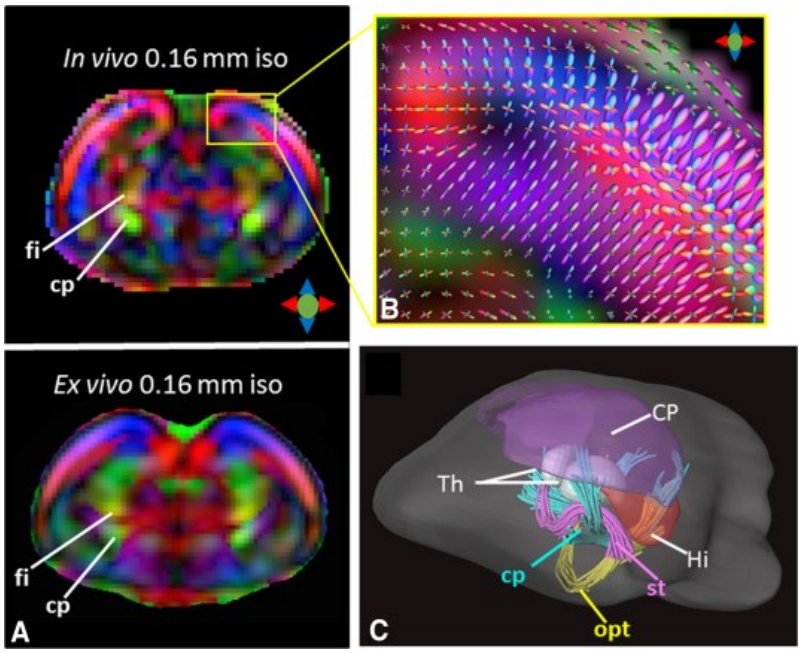

Figure 5.6: (A) *In vivo* DTI colormaps of an embryonic mouse brain acquired at 0.16 mm isotropic resolution (top row), compared with *ex vivo* DTI acquired at 0.16 mm resolution (bottom row). (B)FOD map showing microstructural organization in the cortical plate and intermediate zone, overlapped on a zoomed-in region from (A). (C) Early white matter tracts reconstructed from the *in vivo* dMRI data at 0.16 mm isotropic resolution. The 3D trajectories of the cerebral peduncle (cp), optic tract (opt), and stria terminalis (st) are rendered relative to the cortical plate (CP), hippocampus (Hi), and thalamus (Th).

The localized *in vivo* dMRI technique was used to detect embryonic brain injury in an inflammatory model of intrauterine LPS injection. Nine embryonic mouse brains from three pregnant dams were examined using the phased array body coil. As this is a model of inflammation in outbred CD1 mice, an expected range of cortical and sub-cortical injuries were found in these embryonic mice. Three representative embryonic mouse brains were demonstrated in Fig. 5.7. Reductions in T_2-weighted signal and ADC value were detected in the cortical regions (yellow arrows, ADC = $2.59 \pm 0.76 \times 10^{-4}$ mm^2/s, n = 7) in almost all the embryos, and several mice showed sub-cortical injury (blue arrows, ADC = $2.01 \pm 0.40 \times 10^{-4}$ mm^2/s, n = 4). The ADC in these affected tissues was reduced to about 1/3 of the normal cortical ADC of $0.65 \pm 0.09 \times 10^{-3}$ mm^2/s (Table 5.1), indicating acute injury, e.g. edema, may have developed within 6hrs after the LPS challenge. Nissl and H&E stained sections (Fig. 5.7(B)) at similar levels showed reduced cortical thickness (0.457 ± 0.026 mm in the LPS treated embryos versus 0.575 ± 0.021 mm in the controls, $p < 0.05$). At high magnification (Fig. 5.7(B)), shrunken neurons with enlarged intercellular space and many unstained regions in cortical area were observed. In the LPS group, the alignment of neurons was not as clear as the control group. Furthermore, the development

of neuronal processes (axon/dendrites) was disrupted and organelles became pyknotic (insets).

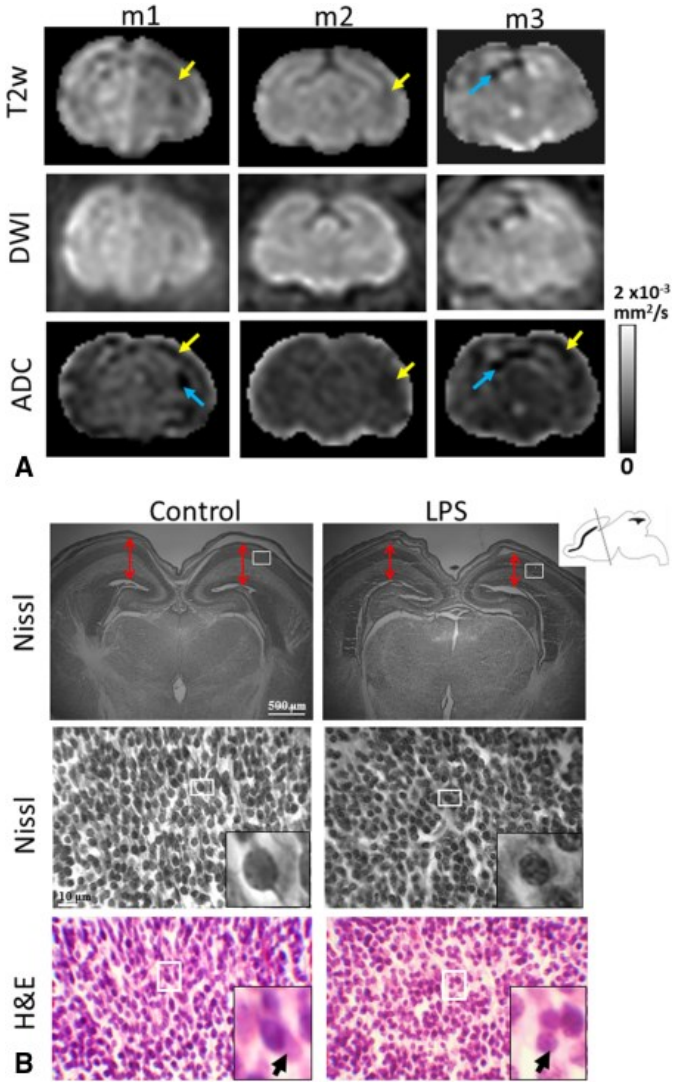

Figure 5.7: (A) *In vivo* T2-weighted images (T2w), DWI, and ADC maps of three E17 embryonic mouse brains at 6 hours after intrauterine injection of LPS. The images were acquired at 0.2 mm resolution using the localized DW-GRASE sequence. Yellow and blue arrows indicate cortical and subcortical injury (reduced T_2 intensity and ADC) in these mice, respectively. (B) Nissl and H&E-stained sections at similar levels as the MR images, from a control embryo and an LPS-treated embryo. The LPS-treated embryo showed reduced cortical thickness (red arrows, including the cortex plate, subplate, intermediate

zone, and ventricular zone) and shrunken neurons (insets), compared to the control embryo. The black arrowheads point to the normal and shrunken cytoplasm in the cortical neurons.

5.4 Discussion

In vivo dMRI of the embryonic mouse brain advances our ability to monitor the embryonic brain development under physiological conditions and in a longitudinal scale. It offers a powerful tool for developmental neuroscience for spatial-temporal mapping of normal embryonic brain development, detection of abnormality in prenatal injury models (223), and phenotype screening in genetically modified models (227). More importantly, this non-invasive technique demonstrates high translational potential for *in utero* monitoring of fetal brain in clinical practice.

The key innovation of this study is the application of spatially selective excitation (221) to perform localized imaging of individual mouse embryo. Localized imaging is ideal for imaging the live embryonic mouse brain. As individual embryos occupy a small fraction of the abdomen, reducing the field-of-view without aliasing provides immense benefit in imaging speed, which can be translated to higher imaging resolution and reduced sensitivity to motion. The reduced field-of-view technique has been used to image several internal organs, including the heart, kidney and spinal cord (219,220). The excitation

profiles of the spatially selective excitation pulses used in this study were tested in our previous study in the mouse brain at 11.7 Tesla (25) and remained satisfactory for applications in the abdomen. Using this approach, a 3D diffusion-weighted image from an embryonic mouse brain can be acquired in less than 2 minutes to acquire. The fast speed reduced the sensitivity to fetal and maternal motion. With navigator-based motion correction, artifacts due to intra-image motions were reduced, and inter-image motions could be mostly remedied by 3D image registration. With the current setup, we had an 80% success rate in acquiring satisfactory diffusion MRI data. Two out of the ten DTI data contained large inter-image motions, due to large movement of the organs in the abdomen, such as release of the bladder during imaging, which could not be fully corrected. One limitation of the current setup is the use of 2D selective excitation pulses, which restrict the selection of embryos for multi-FOE imaging (no overlap in both x-y and z). With the advances in 3D selective excitation pulses and parallel transmission hardware (219), it will be straightforward to achieve multi-FOE imaging with even higher efficiency.

High-throughput acquisition of the T_2-weighted b_0 image and ADC maps of single or multiple embryonic mouse brains was achieved using a body coil. These images can be sufficient to reveal brain morphology, including the sizes of the brain and ventricles, as

well as certain pathology, as in the case of LPS-induced inflammation model. We demonstrated in a mouse model of intrauterine inflammatory injury that cortical injury can be detected from the ADC maps. The reduction of ADC as shown *in vivo* and the shrinkage of neurons after fixation and dehydration, suggested severe edema may have developed within 6hrs exposure to inflammation. This information could be lost or confounded by chemical fixation in *ex vivo* MRI. *In vivo* detection of such abnormalities at acute stages provide critical diagnostic value to evaluation of potential long-term neurological and immune deficits (224). Longitudinal monitoring in the perinatal stages can further trace the disease progression and guide therapeutic interventions.

In this study, diffusion tensor imaging of the embryonic mouse brain, which requires high SNR, was acquired using a high sensitivity planar surface coil and after injection of Gd-DTPA. Compared to the body array coil, the planar surface coil provides higher sensitivity but only allows a limited imaging area, which often contains less than three mouse embryos and discourages the use of multi-FOE imaging. The injection of Gd-DTPA significantly increased SNR due to shortening of tissue T_1. Previous studies (228) have shown that Gd-DTPA can go through the placenta and enter the embryonic mouse brain due to the undeveloped blood-brain barrier (BBB). Gd tends to stay in the uterus for a

prolonged time because it is excreted by the embryos in the fluid and then taken up by the embryo again. This is important for DTI because it provides ample time for lengthy DTI acquisition. The effect of exposure to MRI and Gd-DTPA on the embryonic mouse development was studied in (32) and no adverse effect was found in term of weight and extremity morphology, etc.

At 0.2-0.16 mm isotropic resolution, we demonstrated *in vivo* DTI of the embryonic mouse brain for the first time. The data revealed important microstructural information in the developing mouse brain under normal physiological conditions. In the E17 embryonic mouse brain, we found high anisotropy in the developing cortical structures (e.g., CP and IZ), which had unique orientations in the colormap and FOD map (Fig. 5.6). The fiber orientations corresponded well to the radially arranged radial glial cells and the highly organized cells and axons with minimal dendrites present at early developmental stages. The high resolution also allowed us to delineate several major white matter fiber tracts and traced their trajectories (Fig. 5.5(D)), which extends our ability to trace early white matter development and abnormalities *in vivo*. Continuing development in this area, especially with higher imaging resolution, will further enhance our ability to study the brain microstructure at early developmental stages.

In conclusion, *in utero* dMRI of the normal and injured embryonic mouse brains was achieved using the localized imaging approach, which addressed the unique anatomy of the mouse uterus to accelerate the acquisition and reduce motion sensitivity. High-resolution DTI of the embryonic mouse brain revealed the major gray matter and white matter structures, and the diffusion measurements reflected normal and pathological brain development.

Chapter 6 Oscillating gradient diffusion MRI of normal and hypoxia-ischemia injured mouse brains

6.1 Introduction

Diffusion MRI (dMRI) utilizes water molecule diffusion to probe brain microstructure and is an important tool to visualize brain structures and a wide spectrum of pathologies. Information on the extent of water molecule diffusion in the labyrinth of tissue microstructures is encoded into dMRI signals by diffusion sensitizing gradients (165). By varying the orientation, strength, and timing of the diffusion sensitizing gradients, many aspects of tissue microstructural organization can be extracted from the collected dMRI signals. Advanced dMRI techniques, e.g., high angular resolution diffusion imaging (HARDI) (229,230) and diffusion spectrum imaging (DSI) (231), use sophisticated diffusion encoding schemes with multiple gradient orientations and strengths to reveal the structural organization and connectivity in the brain.

The timing of the diffusion sensitizing gradients, especially the diffusion time, can also be used to explore tissue microstructural properties. The concept of diffusion time

dependent dMRI had been introduced more than two decades ago (232), and demonstrated diffusion time dependence of dMRI signals in biological tissues (233-236). In order to overcome the limited minimum diffusion time (> 5 ms) in conventional pulsed gradient spin echo (PGSE) methods, oscillating gradient spin echo (OGSE) method was developed to achieve ultra-short diffusion times using high frequency oscillating gradient waveforms (27,237-239) (illustrated in Figure 6.1). In fact, OGSE dMRI is a unique tool to measure the so-called temporal diffusion spectrum, which is the Fourier transform of water molecule velocity autocorrelation function (232,240). The relationship between temporal diffusion spectrum and microstructural properties, such as cell size and membrane permeability, has been studied using numerical simulation (241-243) as well as in phantoms (237,244,245) and animals (27,246). Applications of OGSE dMRI to study tissue microstructure in normal (247-251) and diseased brains (252,253) showed promising results. Recently, the feasibility of performing OGSE-dMRI experiments on clinical scanners with limited gradient strengths has been demonstrated, and increased ADCs with oscillating frequency was reported in several white and gray matter structures in human brain (254,255).

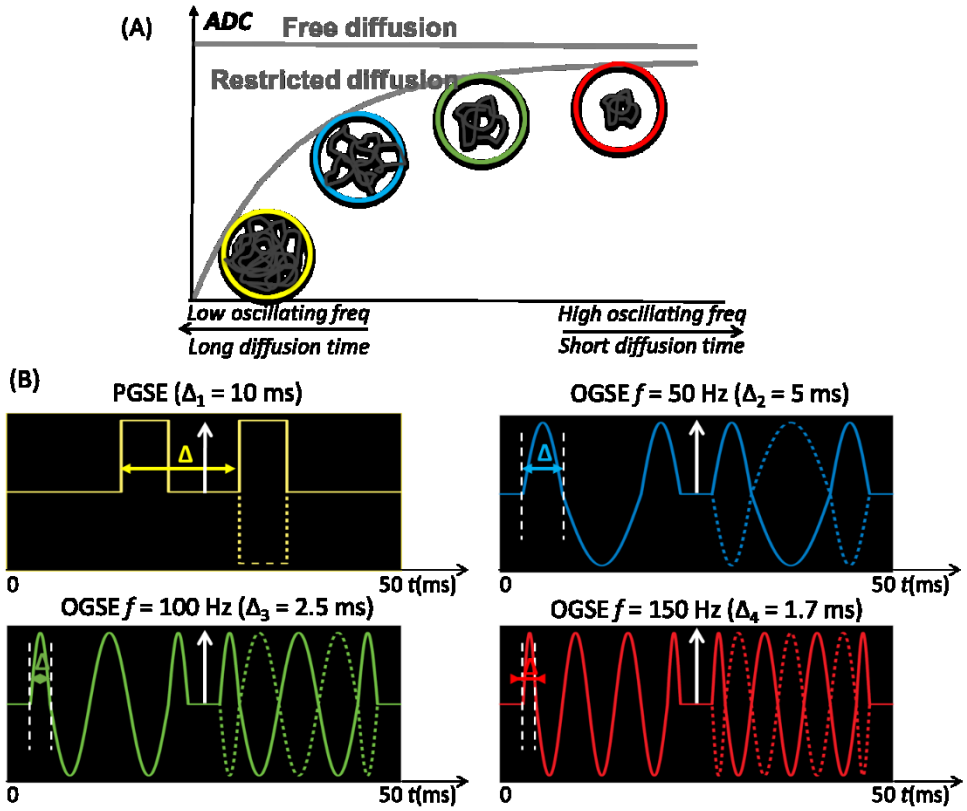

Figure 6.1: Concept of time-dependent water diffusion and measurements with OGSE. With conventional PGSE, the diffusion time is usually quite long, and the water diffusion measured at this long diffusion time (Δ_1) is restricted by the microstrutrual boundaries, such as the cell membrane. With sinusoidal OGSE, the diffusion time (Δ_2) is reduced to ¼ of the oscillating cycle, which can be further reduced within increasing oscillaiting frequency (Δ_3- Δ_4). At these short diffusion times, the water molecules displacements ($\bar{x} = 2\sqrt{2Dt}$) are in smaller ranges, and therefore, the diffusion becomes less restricted.

In this study, we further investigated whether OGSE dMRI could provide additional information on brain microstructural changes after formaldehyde fixation and after hypoxic-ischemic injury. Previous PGSE-dMRI based studies showed significant differences between *in vivo* and *ex vivo* ADC values in the brain, as death and chemical

fixation can alter tissue microstructural properties, for instance, membrane permeability and relative sizes of tissue compartments (85,86). Similarly, microstructural changes in the brain after hypoxia-ischemia, including swelling of cell bodies and processes, have also been extensively studied (256-258), and such changes may be the underling causes of the dramatic reduction in ADC after acute HI injury (259-261). Understanding how these microstructural changes affect OGSE-dMRI signals and temporal diffusion spectra will extend our knowledge on the relationships between tissue microstructures and dMRI signals.

6.2 Methods

6.2.1 Animals and experimental setup

In this study, we used five adult C57BL/6 mice (six-month old, female) and 23 postnatal day 10 (P10) C57BL/6 mouse pups (Jackson Laboratory, Bar Harbor, ME, USA). The P10 mouse pups were subjected to hypoxia ischemia using the Vannucci model adapted for neonatal mice as described previously (unilateral ligation of the right carotid artery followed by 45 minutes of hypoxia, FiO2=0.08) (262,263). After imaging experiments, mice were sacrificed via transcardially perfusion and fixation with 4%

paraformaldehyde (PFA) in phosphate buffered saline (PBS) for *ex vivo* MRI and histology. After fixation, the mouse heads were removed and immersed in 4% PFA in PBS for 24 hours, and then transferred to PBS for one week. All animal procedures were approved by the Animal Use and Care Committee at the Johns Hopkins University School of Medicine.

6.2.2 Pulse sequences

A PGSE echo planer imaging (EPI) sequence was used to acquire the baseline PGSE MRI data. For the OGSE experiments, the gradient pulses in the DWSE-EPI sequence were replaced by the apodized cosine (27) and cosine-trapezoid (255) oscillating gradient waveforms. The effective b-values of the three sequences were calculated by numerical integration of following equation.

$$b = \int \left(\int_0^t g(\tau) d\tau \right)^2 dt \qquad \text{Equation 1}$$

The calculation of effective b-values was validated using an agarose gel (4% by weight) phantom with a b-value of 600 s/mm^2. No statistical difference was found among the PGSE, apodized cosine, and cosine-trapezoid OGSE measurements at 50 to 200 Hz.

6.2.3 *In vivo* MRI of the adult mouse brain

In vivo MRI experiments were performed on a horizontal 11.7 Tesla Bruker scanner (Bruker Biospin, Billerica, MA, USA) in a triple-axis gradient system (maximum gradient strength = 740 mT/m) with a 72 mm volume transmit coil and a 15 mm planar surface receive coil to image the mouse forebrain, whereas the mouse cerebellum was imaged with a quadrature surface transmit/receive cryogenic probe in order to achieve high resolution (264).

In vivo OGSE-dMRI was acquired using the cosine-trapezoid oscillating gradient waveform and 4-segment multi-slice EPI readout with a partial Fourier factor of 1.32. Imaging parameters for OGSE of the adult mouse forebrain were: echo time (TE)/repetition time (TR) = 57.5/5000 ms; four signal average; diffusion gradient length (δ) = 20 ms; number of oscillating cycles (N) = 1, 2, 3, 4 for oscillating frequencies of 50Hz, 100Hz, 150Hz and 200Hz, respectively; b-value = 600 s/mm^2; two non-diffusion weighted images (b_0 images) and six diffusion weighted images (gradient directions: [1 1 0], [1 0 1], [0 1 1], [-1 1 0], [1 0 -1], and [0 -1 1]); 0.125 mm x 0.125 mm in-plane resolution with a field of view (FOV) of 16 mm x 16 mm and slice-thickness of 0.8 mm for eight coronal slices; scan time ≈ 11 minutes with respiration triggering for each oscillating frequency. The

mouse cerebellum was imaged with slightly different parameters: TE/TR = 44/2000 ms; eight signal average; δ = 15 ms ; N = 2, 3, 4 for oscillating frequencies of 100Hz, 150Hz and 200Hz, respectively; b-value = 600 s/mm^2; two b_0 images and ten diffusion weighted images (the six directions listed previously plus [1 1 1], [-1 1 1], [1 -1 1], and [1 1 -1]); 0.1 mm x 0.1 mm in-plane resolution with a FOV of 12.8 mm x 9.6 mm and slice-thickness of 0.6 mm for six sagittal slices; scan time ≈ 13 minutes with respiration triggering for each oscillating frequency. PGSE data were acquired using the pulse gradient with the same parameters (including TE and TR) to the corresponding OGSE data and δ/Δ = 4/20 ms. Co-registered T2-weighted images were acquired using a fast spin echo sequence with TE/TR = 50/3000 ms, two signal averages, and echo train length = 8.

6.2.4 *In vivo* MRI of the neonatal mouse brains after hypoxia-ischemia

In vivo dMRI of the HI-injured neonatal mouse brain were performed at 24 hours after injury (P11) on the 11.7 Tesla scanner using a 72 mm diameter quadrature transmit coil and a 10 mm diameter receive-only planar surface coil. Each mouse was imaged with two 4% agarose gel phantoms on both sides of the brain for calibration. Imaging parameters for the neonatal OGSE dMRI are: TE/TR = 52/2000 ms; four signal average; δ = 20 ms; N =

1, 2, 3 and 4 for oscillating frequencies of 50Hz, 100Hz, 150Hz and 200Hz, respectively; b-value = 600 s/mm^2; two b_0 images and six diffusion weighted images; 0.17 mm x 0.17 mm in-plane resolution with a field of view (FOV) of 16 mm x 16 mm and slice-thickness of 0.8 mm for eight slices along anterior-posterior; scan time ≈ 5 minutes with respiration triggering for each oscillating frequency. Co-registered PGSE dMRI data (δ/Δ = 4/20 ms) were acquired with the same parameters (including TE and TR). A high b-value PGSE scan was acquired to obtain fractional anisotropy (FA) image for anatomical definition, with TE/TR = 24/2000 ms, one signal average, δ/Δ = 4/12 ms, b-value = 1000 s/mm^2, four b_0 images and 30 diffusion weighted images, scan time ≈ 6 minutes.

6.2.5 *Ex vivo* MRI

The same mice used for *in vivo* MRI were used for *ex vivo* MRI. *Ex vivo* dMRI of the adult and P11 mouse brains was performed on a vertical 17.6 Tesla NMR spectrometer (Bruker Biospin, Billerica, MA, USA) with a Micro2.5 gradient system (maximum gradient strength = 1500 mT/m) and a 15 mm diameter transceiver volume coil. During MRI, the specimens were immersed in fomblin (Fomblin Perfluoropolyether, Solvay Solexis, Thorofare, NJ, USA) for susceptibility matching and to prevent dehydration. The

temperature of the specimens was maintained at 37 °C via the spectrometer's temperature control system. The same imaging protocol as the *in vivo* MRI was used, except that the b-value was 800 s/mm^2 for both OGSE and PGSE scans.

6.2.6 Data analysis

The k-space EPI data were zero-padded by a factor of two without apodization prior to Fourier transform. The ADC maps at each diffusion gradient were calculated by averaging the diffusion coefficients from the all diffusion directions with ADC = -ln(S/S_0)/($b-b_0$). ADC values from *in vivo* experiments were corrected based on the ADCs of an agarose gel phantom to correct for instability due to animal breathing. The rate of ADC increase with oscillating frequency (Δ_fADC) was calculated by the linear fitting in Matlab (www.mathworks.com). The regions of interest (ROIs) were manually defined based on ADC, FA, and co-registered T2-weighted images in ROIEditor (www.mristudio.org) for quantitative analysis. Statistical tests were performed using paired two-tailed Student's t-test.

6.2.7 Tissue processing and histopathology

Perfusion fixed mouse brains were removed from skulls and cryo-protected in 30% sucrose. The brains were cut serially on a sliding microtome of 60 microns. Every 10^{th} section was stained with cresyl-violet and adjacent sections were stained with hematoxylin and eosin (H&E). Near- adjacent sections were stained immune-cyto-chemically for glial fibrillary and acidic protein (GFAP). An immune-peroxidase method was used with a polyclonal rabbit antibody (Santa Cruz Biotechnology, Santa Cruz, CA, USA) to GFAP. The histological slides were imaged with a Nikon microscope (Nikon Instruments Inc., Melville, NY, USA).

6.3 Results

6.3.1 Formaldehyde fixation altered the temporal diffusion spectra in the adult mouse brain

Both *in vivo* and *ex vivo* OGSE-dMRI of the adult mouse brain showed frequency-dependent ADC changes (Fig. 6.2). In the cortex and hippocampus, the rates at which the *in vivo* ADC values increased with frequencies (Δ_fADC) were 0.33 ± 0.05 μm^2 and 0.38 ± 0.05 μm^2, respectively (Table 6.1). In comparison, *ex vivo* PGSE-ADC values measured in

the same regions were significantly reduced. With increasing frequency, the *ex vivo* OGSE-ADC values in the cortex and hippocampus increased more rapidly than the *in vivo* measurements, and the corresponding Δ_fADC values (Table 6.1) were significantly higher than the *in vivo* estimates ($p = 8.85 \times 10^{-7}$ and $p = 2.57 \times 10^{-6}$). As a result, the differences between *in vivo* and *ex vivo* OGSE-ADC values gradually decreased in the cortex (Fig. 6.2(B)) and hippocampus (Fig. 6.2(C)) with increasing frequency.

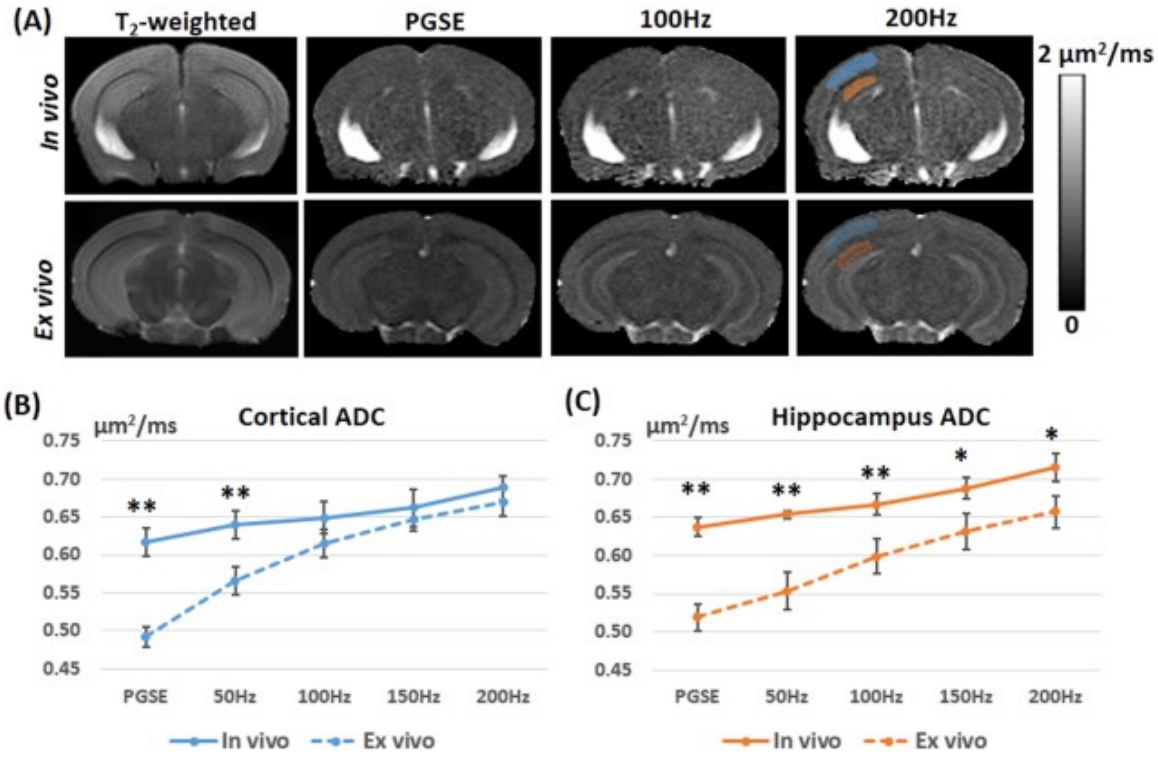

Figure 6.2: Comparisons of *in vivo* and *ex vivo* ADC maps of the adult mouse brain acquired using pulsed gradient spin echo (PGSE) and oscillating gradient spin echo (OGSE) methods. A: Axial T2-weighted, PGSE-ADC, and OGSE-ADC (at 100 and 200 Hz) images of a representative adult mouse brain. The blue and red shadings indicate the regions of interest that are manually placed to obtain ADC values in the cortex and hippocampus, respectively. B,C: Plots of *in vivo* ADC (solid lines) and *ex vivo* ADC

(dashed lines) values measured in the cortex and hippocampus at different frequencies ($n = 5$). Error bars indicate the inter-subject standard deviation. * and ** denote that a two-tailed t-test between the *in vivo* and *ex vivo* measurements produced a *P*-value less than 0.01 and 0.001, respectively.

Table 6.1: *In vivo* and *ex vivo* ADC measurements ($n = 5$) of the adult mouse cortex and hippocampus. Note: * and ** denote that a two-tailed t-test between the *in vivo* and *ex vivo* measurements produced a *p*-value less than 0.01 and 0.001, respectively.

ADC(μm^2/ms)	Cortex		Hippocampus	
	In vivo	*Ex vivo*	*In vivo*	*Ex vivo*
PGSE	0.62±0.02**	0.49±0.02	0.64±0.01**	0.52±0.02
50Hz	0.64±0.02**	0.57±0.02	0.65±0.01**	0.55±0.02
100Hz	0.65±0.02	0.61±0.02	0.67±0.01**	0.60±0.02
150Hz	0.66±0.02	0.65±0.02	0.69±0.01*	0.63±0.02
200Hz	0.69±0.02	0.67±0.02	0.72±0.02*	0.66±0.02
Δ_fADC(μm^2)	0.33±0.05**	0.87±0.07	0.38±0.05**	0.71±0.05

In the mouse cerebellum, we also found considerable differences between the *in vivo* and *ex vivo* temporal diffusion spectra. The *in vivo* ADC values in the cerebellar granule cell layer (CBGr) and cerebellar molecular layer (CBML) were significantly higher (1.5-2 times) than the *ex vivo* ADC values in PGSE and OGSE up to 200 Hz (Fig. 6.3(A-B)). The *in vivo* Δ_fADC of the CBGr (3.46 ± 0.21 μm^2) was significantly higher than the *ex vivo* values (2.21 ± 0.20 μm^2, $p = 1.11 \times 10^{-5}$) and the *in vivo* Δ_fADC of the CBML (0.55 ± 0.28 μm^2). No significant difference was found between the *in vivo* and *ex vivo* Δ_fADC values in the CBML (Fig. 6.3(C), $p = 0.32$). These differences resulted in different contrasts

between CBGr and CBML in the *in vivo* and *ex vivo* ADC maps over the 0-200Hz frequency range (Fig. 6.3(A)).

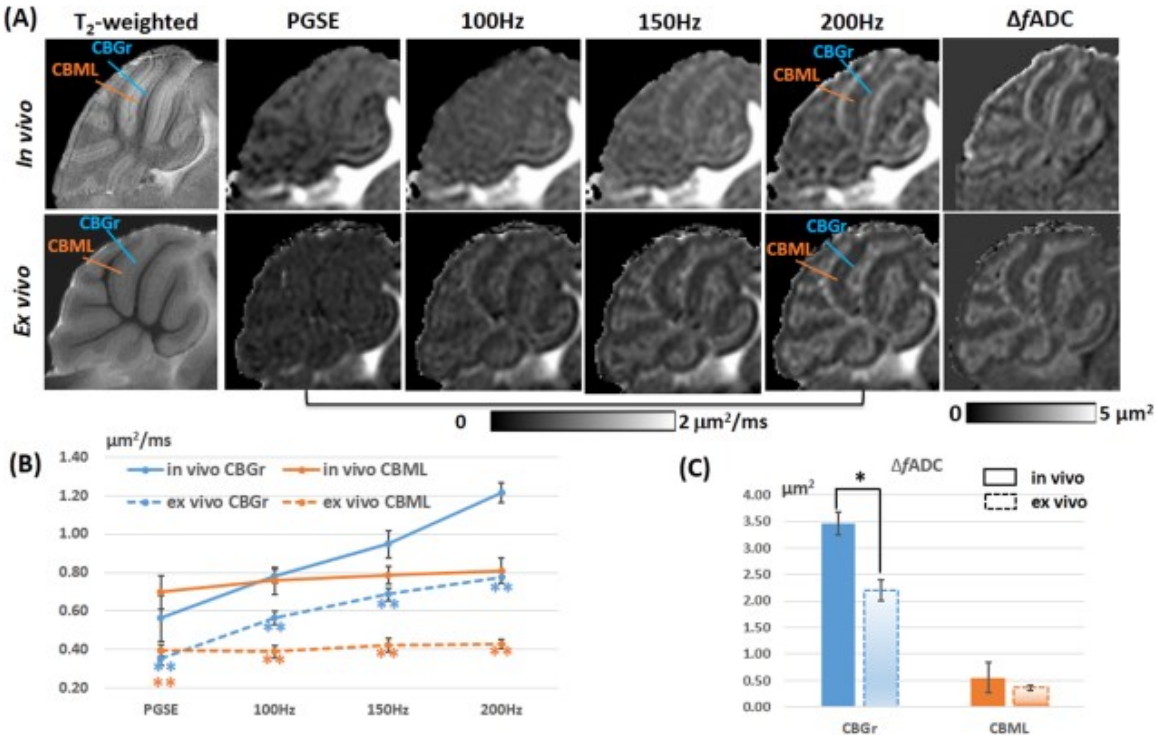

Figure 6.3: Frequency-dependent tissue contrast in the adult mouse cerebellum. A: Para-sagittal (0.6 mm off the midline) T2-weighted, PGSE-ADC, OGSE-ADC, and fitted ΔfADC images of the *in vivo* and *ex vivo* mouse cerebellum. The orange lines indicate the location of the cerebellar molecular layer (CBML), and the blue lines indicate the location of the cerebellar granule cell layer (CBGr). B: Plots of *in vivo* and *ex vivo* ADC values measured in the CBGr and CBML at different frequencies ($n = 5$). C: Comparison of the *in vivo* and *ex vivo* ΔfADC values in the CBGr and CBML ($n = 5$). Error bars indicate the inter-subject standard deviation. * and ** denote that a two-tailed t-test between the *in vivo* and *ex vivo* measurements produced a P-value less than 0.05 and 0.001, respectively.

6.3.2 Pseudo-normalization of OGSE-ADC values observed in severe edema regions after neonatal HI injury

Among the twenty-three neonatal mice that underwent right carotid artery ligation and hypoxia, six mice (three males and three females) developed extensive cortical and hippocampal edema on the right side at 24 hours after injury as indicted by reduced PGSE-ADC and hyper-intense T2 signals (Fig. 6.4). The PGSE-ADCs in the ipsilateral cortex and hippocampus were reduced by 51.9 ± 5.4% and 42.3 ± 8.7% with respect to the contralateral side, respectively (Fig. 6.5(A-B)). As frequency increases, the contrast between the edema regions and neighboring regions gradually decreased in the OGSE-ADC maps compared to the PGSE results. The pseudo-normalization of OGSE-ADC values in the edema region is the result of rapid increase in OGSE-ADC values with increasing frequency (Fig. 6.5). For example, the Δ_fADC values were elevated by 4.5 times in the ipsilateral cortex than its contralateral counterpart, and 3.7 times in hippocampus (3.7 times) (Table 6.2). At 200 Hz, the ipsilateral ADC values became statistically undistinguishable from the contralateral side (Fig. 6.5(A-B)). Within the hippocampus, two layer structures were enhanced in the OGSE-ADC maps at 100-200 Hz (yellow arrows in Fig. 6.4) and in the Δ_fADC map.

Ex vivo dMRI of the same neonatal mouse brains after 4% PFA fixation presented large variations in ADC values in the ipsilateral cortex and hippocampus, as indicated by the blue and orange arrows in Fig. 6.4. Despite the large variability in *ex vivo* ADC values, the Δ*f*ADC values measured in the ipsilateral cortical lesions remained fairly consistent (1.35 ± 0.08 μm^2), which were higher than those in the contralateral cortex (1.02 ± 0.13 μm^2, $p = 0.002$). *Ex vivo* ADC measurements in the contralateral brain were consistent (Fig. 6.5(A-C)), which also had elevated Δ*f*ADC values but at a lesser degree compared to that in the edema regions.

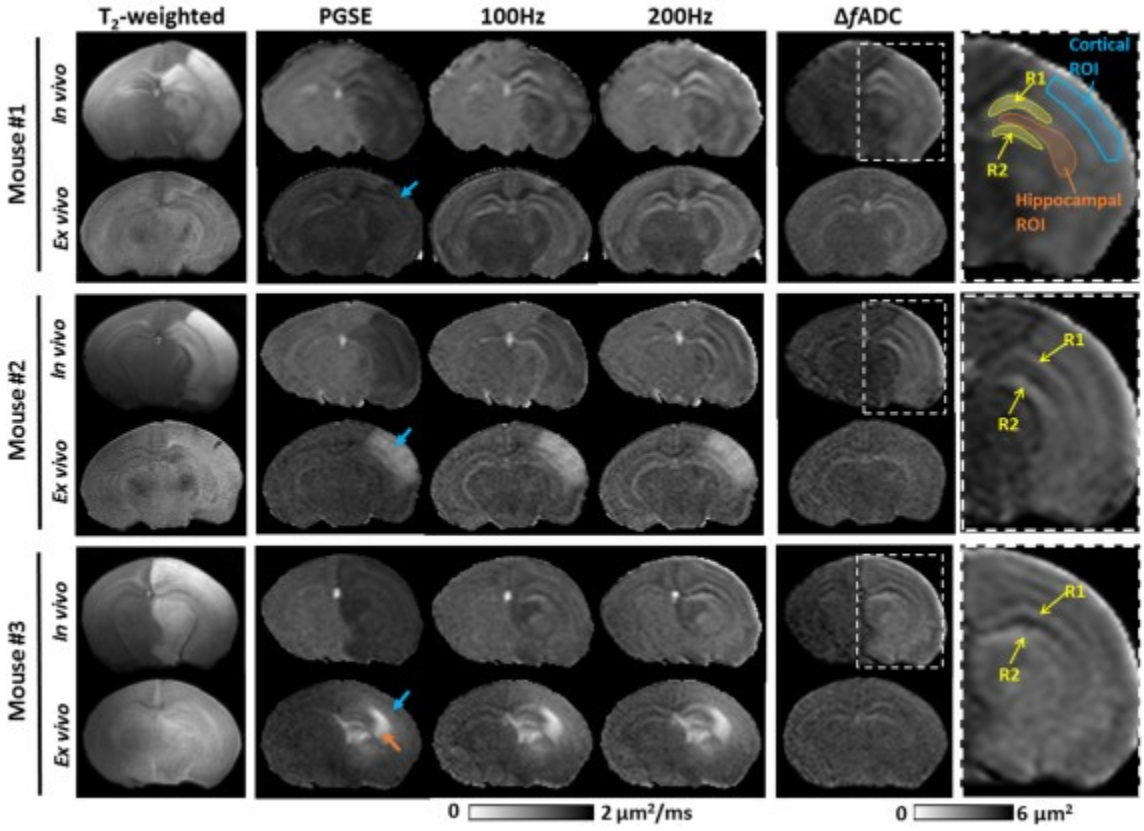

Figure 6.4: Representative MR images of three (out of six) P11 mice with severe edema in the cortex and hippocampus. Axial T2-weighted, PGSE-ADC, OGSE-ADC (at 100 and 200 Hz), and Δ*f*ADC maps were shown. Both *in vivo* and *ex vivo* MR images were displayed. The blue and orange arrows indicate high signal variations in the ipsilateral cortical and hippocampal regions of *ex vivo* specimens, respectively. The yellow arrows indicate two layers (R1/R2) in the ipsilateral hippocampus that were enhanced at 200 Hz. Definitions of the cortical, hippocampal and R1/R2 ROIs were superimposed on the enlarged Δ*f*ADC map of the injured hemisphere.

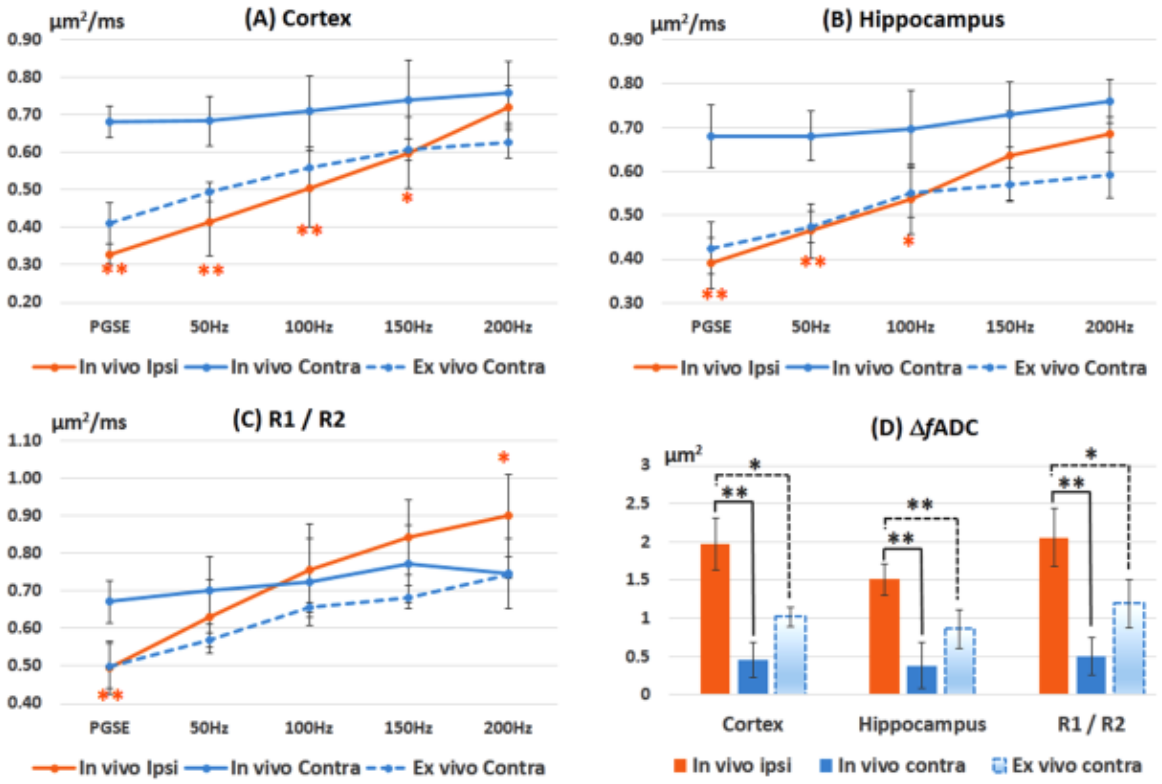

Figure 6.5: Changes in ADC with frequency in the cortex, hippocampus, and the joint regions of the R1 and R2 (R1/R2). The Δ*f*ADC values in the edema regions were significantly higher than both *in vivo* and *ex vivo* Δ*f*ADC values measured in the contralateral regions. Error bars indicate the inter-subject standard deviation. The *ex vivo* ADC values from the ipsilateral side were not included due to large variations. * and ** denote that a two-tailed t-test between the ipsilateral and contralateral measurements produced a *P*-value less than 0.01 and 0.001, respectively.

Table 6.2: *In vivo* ADC measurements measured from five P11 mice at 24 hours after hypoxia-ischemia in the cortex, hippocampus, and the two layers of the hippocampus (R1 / R2 as indicated in Fig. C) of the ipsilateral and contralateral hemispheres. Note: results of two-tailed paired t-test were denoted by ** $p \leq 0.001$, * $p \leq 0.01$

ADC ($\mu m^2/ms$)	Cortex		Hippocampus		R1/R2	
	Ipsi	Contra	Ipsi	Contra	Ipsi	Contra
PGSE	0.33±0.04 **	0.68±0.03	0.39±0.06 **	0.68±0.07	0.50±0.07 **	0.67±0.06
50Hz	0.41±0.07 **	0.68±0.09	0.46±0.06 **	0.68±0.06	0.63±0.10	0.70±0.09
100Hz	0.50±0.10 **	0.71±0.10	0.54±0.08 *	0.70±0.09	0.76±0.12	0.72±0.12
150Hz	0.60±0.11 *	0.74±0.10	0.63±0.10	0.73±0.07	0.84±0.10 *	0.77±0.10
200Hz	0.72±0.08	0.76±0.06	0.68±0.04	0.76±0.05	0.90±0.11 **	0.75±0.09
Δ_fADC(μm^2)	1.93±0.36 **	0.43±0.24	1.51±0.23 **	0.41±0.32	2.05±0.43 **	0.44±0.22

A histological survey of H&E-stained sections revealed severe tissue swelling in the hippocampus (Fig. 6.6(A-B)) and cerebral cortex (Fig. 6.6(C-D)) at 24hrs of recovery. In the hippocampus, the CA1 region in HI mice showed discrete expansion of several layers, including the stratum oriens (so), stratum radiatum (sr), and stratum lacunosum-moleculare (slm) (Fig. 6.6(A-B)). The slm appeared to have the most severe injury in hippocampus at 24hrs after HI (compare the length of the identified arrows, Fig. 6.6(A-B)). Edema was also present in somatosensory cerebral cortex. The damaged zone showed a clear pallor of staining compared to the nearby cortical parenchyma (Fig. 6.6(C-D)). Cortical swelling

was evident by comparing the width between the pial surface and the subcortical white matter (marked by black lines in Fig. 6.6(C-D)). GFAP immunostaining revealed activation of astrocytes in hippocampus at 24hrs after HI compared to controls (Fig. 6.6(E-H)). Injured astrocytic processes in HI hippocampus were swollen and appeared fragmented in some instances.

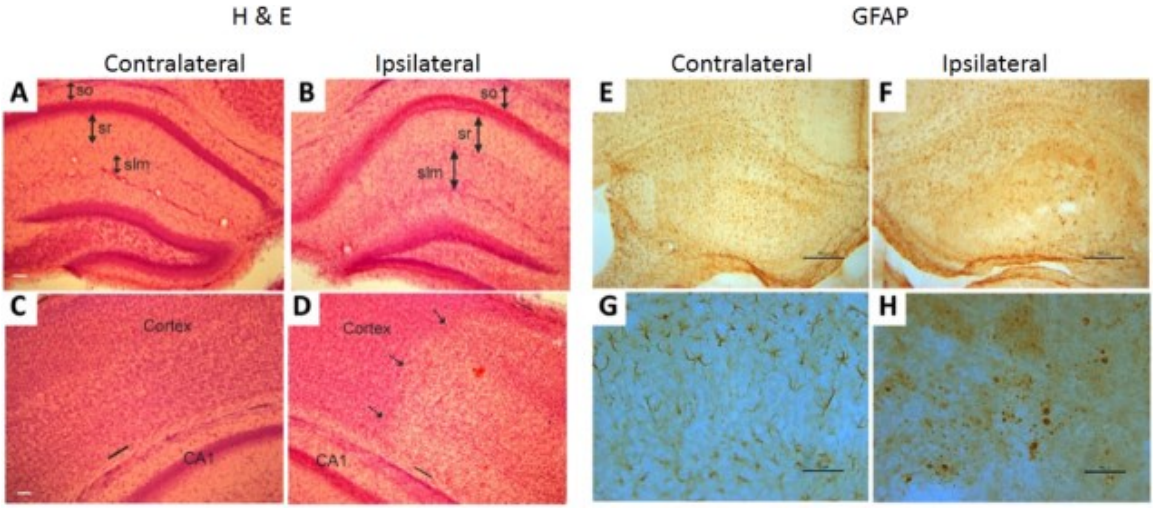

Figure 6.6: H&E and GFAP stained histological sections of the contralateral (control) and ipsilateral (HI) sides of a representative HI injured P11 mouse brain. A,B: In the HI hemisphere (B), severe tissue swelling was found in the hippocampus, with increases in the thickness of the stratum oriens (so), stratum radiatum (sr), and stratum lacunosum/moleculare (slm). Scale bar (in A) = 77 µm (same for B). C,D: Tissue swelling was evident in the cerebral cortex after HI. The dashed arrows indicate the boundary of necrotic region, and the black lines in the pial surface and subcortical white matter indicate the width of cortex. Scale bar = 77 µm in C (applies for D). E,F: Astrocytic GFAP immunoreactivity (brown staining) was diminished in the HI hippocampus (F) compared with control hippocampus (E). Scale bars = 117 µm in E,F. G,H: Higher magnification images show normal astrocytes in control hippocampus (G) and fragmented astrocytes in the hippocampus of HI brain (H). Scale bars = 50 µm.

6.4 Discussion

One of the appealing features of OGSE-dMRI is its potential to filter dMRI signals based on the sizes of underlying microstructural barriers and thereby provide an additional angle to examine tissue microstructural organization and integrity using dMRI. To better understand the capability of OGSE-dMRI, it is important to examine perturbations in temporal diffusion spectra in response to tissue microstructural changes, especially under pathological conditions. In this study, a relatively small portion of the temporal diffusion spectrum was measured in the mouse brain, from 0 Hz (PGSE) to 200 Hz with a spectral resolution of 50 Hz. We measured changes in temporal diffusion spectra using absolute ADC values and Δ_fADC, which was simply the slope of ADC increase as the frequency increased from 0 Hz to 200 Hz. The effective diffusion times in this study ranged from 20 ms (PGSE) down to 1.25 ms (OGSE at 200 Hz), during which the mean square distances of water molecule diffusion fell between 11 μm and 2.7 μm (calculated based on the free water diffusion constant of 3 x 10^{-3} mm^2/s at body temperature (265)). The range of distances is approximately at the cellular and subcellular level, e.g., the nucleus. Based on the results of previous phantom experiments (237) and simulations (242), the limited frequency span and resolution will only allow us to examine microstructures within a

certain range of spatial scales, with reduced sensitivity for microstructures outside this range. One example that illustrates this limitation is the observed temporal diffusion spectra of CBGr and CBML (Fig. 2). The CBML consists of a large number of parallel fibers with diameters around 0.2-0.3 μm (266), which is an order of magnitude smaller than the mean square distance of free water diffusion at 200 Hz. This may explain why its ADC values showed little increase from 0 to 200 Hz and little change in its Δ_fADC values after fixation. In comparison, the CBGr contains densely packed granule cells (5-10 μm in diameter) (267), and the data showed moderate increases of ADC with increasing frequency and significant differences between its Δ_fADC values measured *in vivo* and *ex vivo* (Fig. 2B-C).

The comparisons between *in vivo* and *ex vivo* OGSE dMRI data demonstrated that formaldehyde fixation could significantly alter the temporal diffusion spectra in biological tissues. The reductions in PGSE-ADCs in formaldehyde fixed mouse cortex and hippocampus are inline with previous reports (85,86). The narrowing of the gaps between *in vivo* and *ex vivo* ADCs as frequency increased and the increases in Δ_fADCs in these two regions (Fig. 6.2 and Table 6.1) are also inline with findings by Does et al. (27) in the postmortem rat brains. Structural changes that can potentially contribute to these changes

can be multifold, including changes in surface-to-volume ratio, compartment size and diffusivity, cell membrane permeability, and nuclear-to-cell ratio (241,244,245). A previous report that studied the effects of tissue fixation on diffusion properties of rat brain slices (85) showed increased intracellular apparent restriction size, likely due to cell swelling (268), after fixation with 4% formaldehyde. According to numerical simulations based on a tissue model of densely packed cells (241), an increase in cell size will decrease ADC values across a large frequency range and lead to increased Δ_fADC, which agrees with our observations in the cortex and hippocampus (Fig. 6.2 and Table 6.1). As the differences between the *in vivo* and *ex vivo* OGSE-ADC values remained significant at 200 Hz, additional microstructural changes might exist at the subcellular or lower levels. Previously, we showed that, in *ex vivo* mouse brains, the CBGr and several other regions with densely populated neuronal cell bodies had significantly higher Δ_fADC than other regions (247). In this study, high-resolution *in vivo* images of the mouse cerebellum also showed a frequency dependent contrast between CBML and CBGr (Fig. 6.3). It is not clear what caused the drop in Δ_fADC by 36% in the CBGr after death and fixation.

Microstructural changes under pathological conditions can provide additional insights into the sensitivity of OGSE-dMRI to tissue microstructures. Previous studies in cat brains

after middle cerebral artery occlusion showed no diffusion time dependence in ADC for diffusion times from 20 ms to 2 s (51). In the neonatal mouse model of unilateral hypoxic-ischemia (253,262), we found significant diffusion time dependence at diffusion times from 1.25 ms to 20 ms. The pseudo-normalization of OGSE-ADC values in the edema region agree with a recent human acute stroke study by Baron et al (269). The phenomenon suggests that the microstructural changes associated with the decrease in PGSE-ADC are mostly at the cellular or subcellular level (> 1 μm), e.g., swelling of cells, as suggested by previous reports (259) and consistent with our histological assessments. It is interesting to note that the ADCs of several metabolites also show less decrease than water molecules after stroke (270-272). For example, ADC of the N-acetyl-aspartate (with a diffusion constant of 0.78 x 10^{-3} mm^2/s) measured using PGSE decreased by 19% at 3 hours after focal cerebral ischemia, whereas the water ADC dropped by 43% (270). One possible explanation is that the mean square distances traveled by metabolites at long diffusion time are similar to that of water molecule diffusion at short diffusion time, and therefore the ADCs of the metabolites reflect microstructural changes at a scale smaller than those of water ADCs measured with the same diffusion time. As discussed above, multiple microstructural changes can lead to the change in temporal diffusion spectra in the edema

regions. It is known that, in cytotoxic edema shortly after hypoxic-ischemia, energy failure of the ion channels causes an influx of water from extracellular space to the intracellular space (273). The expansion of the affected cortex and hippocampal layers, which resulted from tissue swelling as shown in our histological data, was likely an important factor accounting for the drop in PGSE-ADC and increases in Δ_fADC. We also found severe necrosis in the ipsilateral cortex and hippocampus, including break down of the nuclei and cellular organelles, which may also explain the elevated Δ_fADC values as the intracellular environment became less restrictive. The locations of the two layer structures in the hippocampus highlighted in the 200 Hz OGSE-ADC maps (R1/R2 in Fig. 6.4) correlated with the hippocampal pyramidal cell layer, the granule cell layer in the dentate gyrus, and their extended dendritic arborization in neighboring regions. The fact that the two regions showed higher OGSE-ADC values than the contralateral side at 200 Hz suggests there were microstructural changes at subcellular or finer levels.

6.5 Conclusion

Our results demonstrate the unique ability of OGSE-dMRI in differentiating tissue microstructures at different spatial scales. We found that formaldehyde fixation can

significantly alter the temporal diffusion spectra in the mouse brain. The tissue contrast between CBGr and CBML in post-mortem mouse cerebellum could be reproduced in live animals. In the neonatal mouse brain with hypoxic ischemic injury, pseudo-normalization of OGSE-ADC in the edema regions suggest that the microstructural changes associated with the decrease in PGSE-ADC are mostly at the cellular or subcellular level.

Chapter 7 Detection of subtle hypoxic-ischemic injury by OGSE in neonatal mice

7.1 Introduction

The unique ability of oscillating gradient spin-echo (OGSE) diffusion MRI (dMRI) to examine tissue microstructure at different spatial scales has been increasingly recognized (27,241,247,254,255). While applications of the technique to neurological diseases, e.g., stroke and tumor (216,253,269), are emerging, the benefits of the additional multi-scale information are not fully explored. In the last chapter, we demonstrated that OGSE dMRI in the Vannucci model of neonatal mouse hypoxia-ischemia (HI) at 24hrs after injury, and hypothesized that the highly time-dependent ADC measurements in the severe edema region is related to cytotoxic cell swelling.

In clinical practice, a wide spectrum of varying degrees of brain injury after HI injury that are common observed, and so does the neurological outcomes in the animal models. Such variability may due to the inter-subject differences and developmental stages (262,274-277). Besides the individual susceptibility, it is found regional vulnerability is prominent in the brain. For example, the cerebral cortex, hippocampus, and striatum (278-

281) are extremely sensitivity to the HI insult and show acute changes in response to the excitotoxic damage. Delayed neurodegneration was found in the thalamus (282), and was likely apoptosis. White matter injury is also extensively studied (283,284), which is associated with the immaturity of oligodendrocyte progenitors. Various cellular and molecular mechanisms were proposed (285,286) that may contribute to the different types and timings of the injury. The role of astrocyte activation or glial swelling (281,287) was highly debated, which was thought to lead to secondary brain damage in some studies (288,289), whereas its neuroprotective values were also realized (290,291). Impairment of mitochondria is a direct consequence of the energy deficits and neurotoxicity after HI (292,293), and plays a key part in the development of apoptotic neuronal degeneration (282,294).

Diffusion MRI evidences of the region-specific injury of different severity have been discussed in many previous studies. Both severe injury and mild white matter injury were observed using T2-weighted imaging and conventional PGSE (103,289,295,296). Based on the PGSE measurements, Lodygensky et al., (296) reported reduced ADC in the hippocampal CA1 field and increased ADC in the surrounding white matter structure in neonatal mice at 24 hrs post injury. In this study, we found distinctively different degrees

of injury were developed from the same injury model, while in the mild injury group, diffusion time-dependent characteristics of the hippocampal injury and white matter injury was revealed. The key innovation of this study lies in the use of explored microstructural change in small spatial scales, which may related to subcellular structures (e.g., astrocytic processes and mitochondria). This is not possible from existing MRI studies. We attempted to detect the subtle microstructural changes at acute stages (3hrs) after the injury, and followed its progression at subacute stage (24hrs).

7.2 Methods

Neonatal C57BL/6 mice (n = 14) from four litters were subjected to unilateral ischemia, followed by 45 minutes hypoxia using the Vannucci model (262,263) at postnatal day 10 (P10). In each litter, one or two sham mice (n = 7 in total) were scanned at the same time points.

In vivo OGSE experiments were performed on an 11.7 T horizontal spectrometer with a 15 mm receive-only planner surface coil and 72 mm quadrature transmitter coil, using cosine-trapezoid oscillating gradient waveforms (255) and a four-segment EPI readout. Pulsed gradient spin echo (PGSE, δ/Δ = 4/20 ms) and OGSE (up to 300 Hz) data were

acquired TE/TR = 52/2000 ms, NA=4, 6 diffusion directions [1 1 0; 1 0 1; 0 1 1; -1 1 0; 1 0 -1; 0 -1 1], b = 600 s/mm^2, in-plane resolution = 0.17 mm x 0.17 mm, and eight slices with slice thickness of 0.80 mm. It took one hour to scan one mice, including all the scans and the setup time. For each litter of about four HI mice, the 3hr time point scan actually spanned from 2hrs to 6hrs after HI injury, and the 24hr scans were conducted from 23hrs to 26hrs.

The ADC values were calibrated using a gel phantom placed beside the mouse brains. ΔfADC was calculated by linear fitting of the ADC values with gradient frequency. Two-way analysis of variation (ANOVA) was performed in GraphPad Prism (http://www.graphpad.com/scientific-software/prism) to compare the multi-frequency ADC measurements between the ipsilateral and contralateral sides, between the 3hrs and 24 hrs scans, and between the mild injury (n=11) and sham mice(n=7). Bonferroni post-tests (297) was performed to evaluate the statistical differences at each oscillating frequencies. $p < 0.001$ was regarded highly significant, $p < 0.01$ was regarded significant. Multi-way analysis of variance (ANOVA) was also performed to analyze the interactive effects of oscillating frequency, mild and sham injury, and post-injury time.

The mice were sacrificed immediately after the 24hrs scan, perfusion fixed, and cryo-protected for histological examination. The brains were cut serially on a sliding microtome at a thickness of 80 microns. Every 10th section was stained with cresylviolet and adjacent sections were stained immunohistochemically for glial fibrillary acidic protein (GFAP). Near-adjacent sections were stained for Microtubule-associated protein 2 (MAP2) and superoxide dismutase 2 (SOD2). Another three HI injured mice from a separate litter were sacrificed after the 3hrs scan for histology.

7.3 Results

7.3.1 Microstructural changes at acute and subacute stages

Due to the intra-subject difference in response to the Vannucci model of hypoxia-ischemia, especially at neonatal stages, variations in the severity and pattern of brain injury were observed. Fig. 7.1 demonstrated two neonatal mouse from the same litter, imaged at 24hrs after HI. The characteristics of the severe injury case (Fig. 7.1(B)) was previously reported in (216). In the mild injury mice (Fig. 7.1(A)), hyperinensive T2-weighted signal was observed in the ipsilateral external capsule (EC) (yellow arrow), as well as in the thalamus (blue arrow). In the ADC maps, the PGSE showed elevated ADC in a thin layer

along EC, similar to the findings in (103,295); whereas the OGSE-ADC at 100Hz and 200Hz showed a thicker region of ADC increase, which expanded from the EC to the CA1 field of the hippocampus right beneath it (red arrow). The change of ADC in CA1 was the further highlighted from the Δ*f*ADC ADC map. It is realized that although the severe and mild injury mice had vastly different injury patterns, but the time-dependent change of ADC in the hippocampal CA1 field share the same features: low ADC in PGSE that rapidly increased with oscillating frequency.

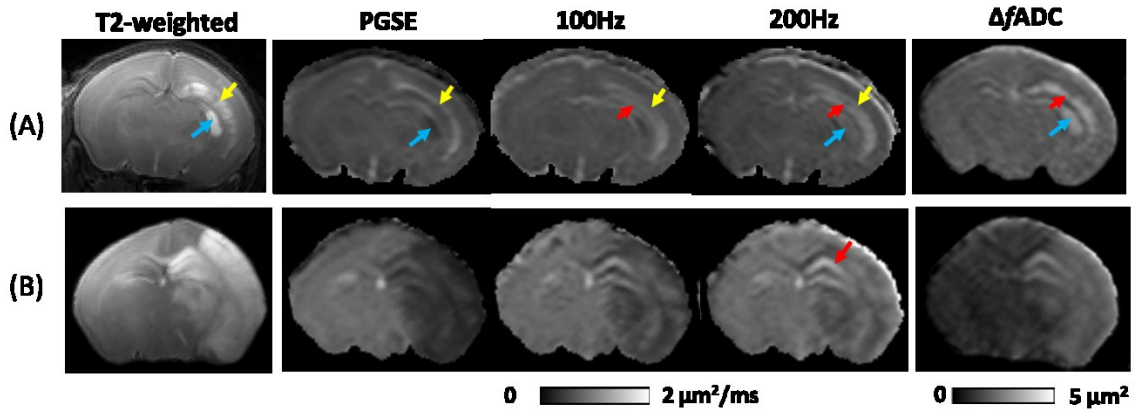

Figure 7.1: T2-weighted image, PGSE and OGSE ADC maps, and Δ*f*ADC of the neonatal mice scanned at 24hrs after the HI-injury. The two mice from the same litter showed a large diversity in their degrees of injury. Yellow arrows point to the external capsule; blue arrows point to the thalamic lesion, and the red arrows point to the leasion in hippocampal CA1-field.

In order to capture the MR signature and the pathology in the two types of injury and time-course of the injury progression, we performed a longitudinal study with relatively

large samples of mice, which were scanned at 3hrs and 24hrs after HI. Majority of the mice (n=11) developed mild injury, consistently showing T2 hyperintensity and ADC elevation in the external capsule (EC) (Fig. 7.2). The ADC difference between the ipsilateral and contralateral sides was subtle at 3hrs, but more obvious at 24hrs (yellow arrows). The abnormality in the ipsilateral CA1 was prominent in the ΔfADC since 3hrs after injury (red arrow). The others (n=3) developed severe edema in the cortex and hippocampus at 3hrs, which further progressed at 24hrs (Fig. 7.2). It is noticed that in the PGSE-ADC map, the low ADC in the ipsilateral CA1 began to pseudo-normalize at 24hrs (orange arrows).

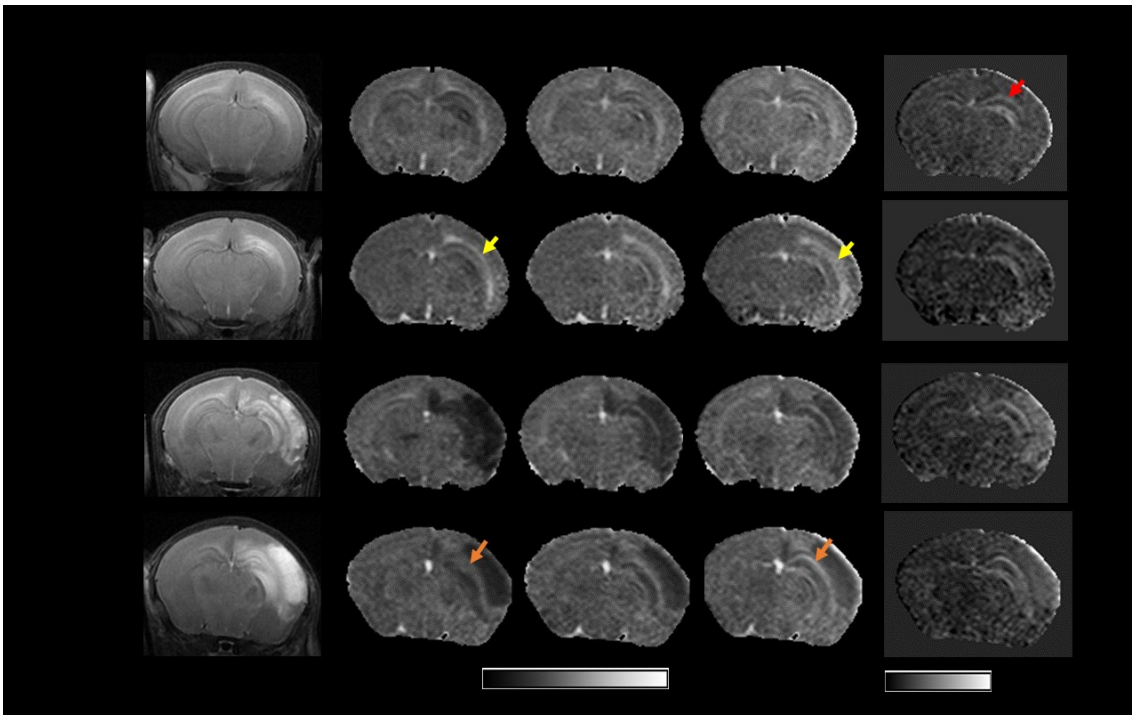

Figure 7.2: T2-weighted image, PGSE and OGSE ADC maps, and ΔfADC of the neonatal mice scanned at 3hrs and 24hrs after the HI-injury. The mice demonstrated mild injury (n = 12, top row) and severe injury (n = 3, bottom row). Yellow arrows point to the external

capsule; red arrow points to the hippocampal CA1-field in the mild injury mouse, and the orange arrows point to the CA1-field in the severe injury mice.

Further information can be obtained from the quantitative analysis in Fig. 7.3. In the mild injury group at 3hrs after injury, two-way ANOVA analysis revealed difference between the ipsilateral and contralateral ADC in EC (yellow shaded ROI). Post-hoc Bonferroni tests showed the difference was significant from OGSE measurements (50-200Hz) (Fig. 7.3(A), red stars), but was not detected from PGSE. At 24hrs, both PGSE and OGSE ADCs were significant higher in ipsilateral EC than the contralateral side (black stars). In hippocampal CA1 field (green shaded ROI), neither the two-way ANOVA nor the individual PGSE and OGSE ADC values showed differences between the ipsilateral and contralateral sides at 3hrs after injury (Fig. 7.3(B)). However, it was still noticeable that the ipsilateral ADC increased faster with oscillating frequency and ΔfADC was higher than the contralateral ADC. At 24hrs, the PGSE-ADC in ipsilateral CA1 become significantly higher in the ipsilateral CA1 ($p<0.01$), and the difference was enhanced at OGSE frequencies ($p<0.001$). The ΔfADC values were significantly higher in the ipsilateral EC and CA1 at both 3hrs and 24hrs (Fig. 7.3(C-D)). Longitudinal comparison showed that in the ipsilateral EC, OGSE-ADC (100-200Hz) increased from the 3hrs scan

to the 24hrs scan (Fig. 7.3(A) orange stars); while in the contralateral EC, all ADC decreased (blue stars). In the ipsilateral CA1, all ADC values (0-200Hz) were significantly higher at 24hrs compared to that at 3hrs, and the contralateral CA1 ADC decreased with time at high frequencies (150-200Hz). The Δ*f*ADC was mostly consistent over time, except that in the ipsilateral CA1, which increased from 3hrs to 24hrs (Fig. 7.3 (D) orange star). ADC measured in the sham mice and comparison with the mild injury mice was shown in Table 7.1. The contralateral side of the mild injury mice did not show significant differences with the sham mice, except for ADCs measured in EC at 3hrs after injury (0-50Hz). The Δ*f*ADC calculated from EC of the sham mice was in-between the ipsilateral and contralateral EC of mild injury mice.

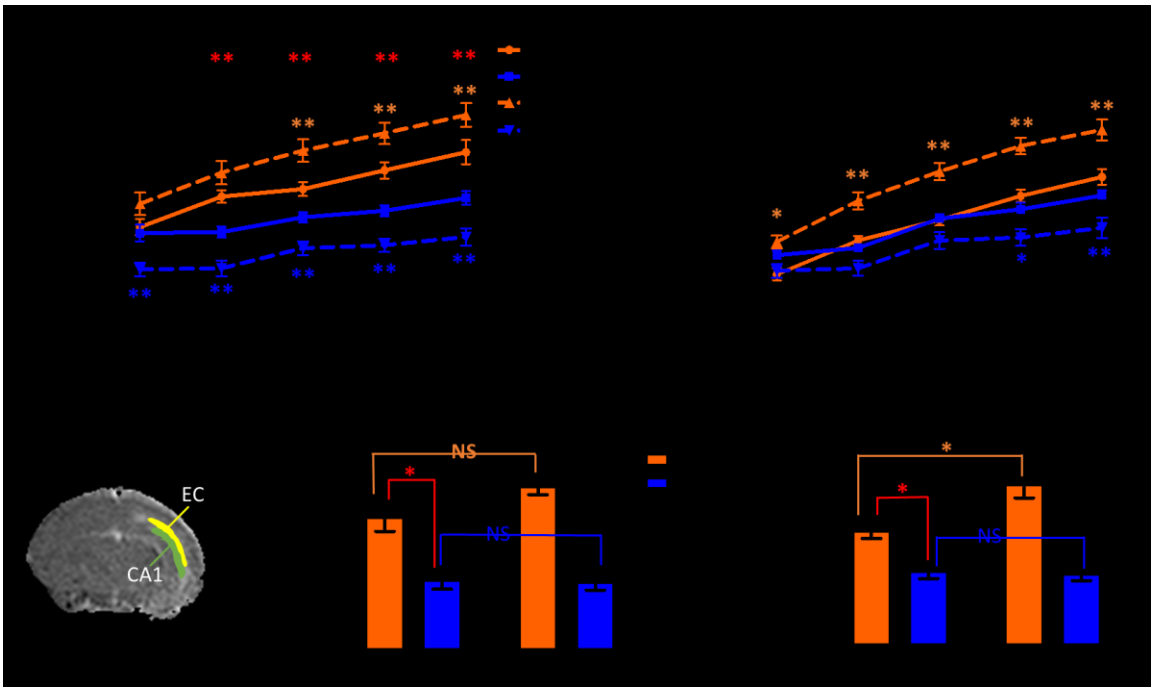

Figure 7.3: (A-B) ADC values (0-200Hz) measured at 3hrs (solid curves) and 24hrs (dashed curves) after HI in the ipsilateral (orange curves) and contralateral (blue curves) in EC (yellow shaded ROI) and CA (green shaded ROI) ROIs, respectively. Data was presented as mean value (n = 11) ± standard error of mean (SEM). Red and black stars indicate significant differences between ipsilateral and contralateral sides at 3hrs and 24hrs, respectively. Blue and red starts indicates significant differences between 3hrs and 24hrs ADC in the ipsilateral and contralateral sides, respectively. (C-D) ΔfADC measured at 3hrs (solid bars) and 24hrs (diagnal bars) after HI in the ipsilateral and contralateral in EC and CA ROIs, respectively. * p< 0.01 and ** p<0.001, and NS denotes no significant difference from post-hoc Bonferroni tests following two-way ANOVA.

Table 7.1: ADC (0-200Hz) and ΔfADC values in the external capsule and CA1, measured from the sham mice (n=7), and ipsilteral and contralateral sides of the mild injury mice (n=11) at 3hrs and 24hrs after injury. Data is presented as mean ± standard deviation. * denotes p<0.01 of post-hoc Bonferroni tests following two-way ANOVA between the sham and ipsilateral ADC, and between sham and contralateral ADC, respecitvely.

External Capsule						
ADC (10^{-3} mm^2/s)	3hrs			24hrs		
	Sham	Ipsi	Contra	Sham	Ipsi	Contra
PGSE	0.73±0.04	0.80±0.05*	0.79±0.05*	0.70±0.05	0.85±0.07*	0.73±0.04
50 Hz	0.73±.0.03	0.86±0.04*	0.80±0.04*	0.70±0.04	0.91±0.07*	0.73±0.05
100Hz	0.77±0.04	0.88±0.04*	0.82±0.03	0.72±0.03	0.95±0.07*	0.77±0.04
150Hz	0.80±0.03	0.91±0.05*	0.84±0.03	0.76±0.03	0.98±0.07*	0.77±0.04
200Hz	0.82±0.04	0.94±0.08*	0.86±0.04	0.78±0.03	1.01±0.07*	0.79±0.05
Δ*f*ADC (10^{-6} mm^2)	0.53±0.20	0.65±0.23	0.34±0.15	0.51±0.18	0.80±0.13*	0.33±0.13
CA1						
ADC (10^{-3} mm^2/s)	3hrs			24hrs		
	Sham	Ipsi	Contra	Sham	Ipsi	Contra
PGSE	0.73±0.04	0.72±0.04	0.77±0.04	0.70±0.05	0.78±0.04	0.73±0.04
50 Hz	0.73±0.03	0.78±0.03	0.77±0.04	0.70±0.05	0.86±0.05*	0.73±0.05
100Hz	0.77±0.02	0.82±0.03	0.83±0.03	0.74±0.05	0.91±0.05*	0.78±0.05
150Hz	0.80±0.03	0.86±0.04	0.84±0.04	0.78±0.04	0.96±0.05*	0.79±0.05
200Hz	0.83±0.04	0.90±0.05	0.87±0.03	0.79±0.04	0.99±0.06*	0.81±0.06
Δ*f*ADC (10^{-6} mm^2)	0.60±0.14	0.84±0.18*	0.51±0.18	0.64±0.22	1.18±0.28*	0.52±0.14

Multi-way ANOVA was used to separate the effects of multiple factors and analyze their interactions on the ADC measurements (Table 7.2). As expected, the effect of oscillating frequency and HI injury had high significances ($p \approx 0$) on ADC values measured in EC and CA1. The impact of post-injury time was significant in CA1 ($p = 0.004$) but not in EC ($p = 0.62$), indicating that the injury progressed from 3hrs to 24hrs in the CA1 field.

The interaction terms showed that there are significant correlations between oscillating frequency and HI ($p < 0.002$), and between post-injury time and HI ($p \approx 0$).

Table 7.2: Multi-way analysis of variation (ANOVA) on effects of oscillating frequency (0-200Hz), HI injury (ipsilateral, contralateral, and sham), and scan time (3hrs versus 24hrs) on the ADC measurements in external capsule and the hippocampal CA1 field.

Multi-way ANOVA	External capsule	CA1
Oscillating Freq	1.82×10^{-18}	6.84×10^{-39}
HI injury	4.19×10^{-40}	2.51×10^{-23}
Post-injury time	0.62	4.51×10^{-3}
Freq & HI	1.71×10^{-3}	6.16×10^{-7}
Freq &Time	0.88	0.96
HI & Time	4.69×10^{-16}	2.31×10^{-21}
Freq & HI & Time	0.95	0.68

7.3.2 Histological evidences of varying scales of microstructural changes

It is known that in addition to neuronal injury by acute cyctotoxic edema, astrocytes activation is also a well-known contributor to the secondary cerebral damage after HI injury (256,289,298). GFAP staining of the neonatal mice at 24hrs after injury demonstrated drastic activation of the astrocytes and their processes in the ipsilateral cortex,

hippocampus and external capsule, compared to the contralateral side (Fig. 7.4), which matched well with the OGSE-ADC maps.

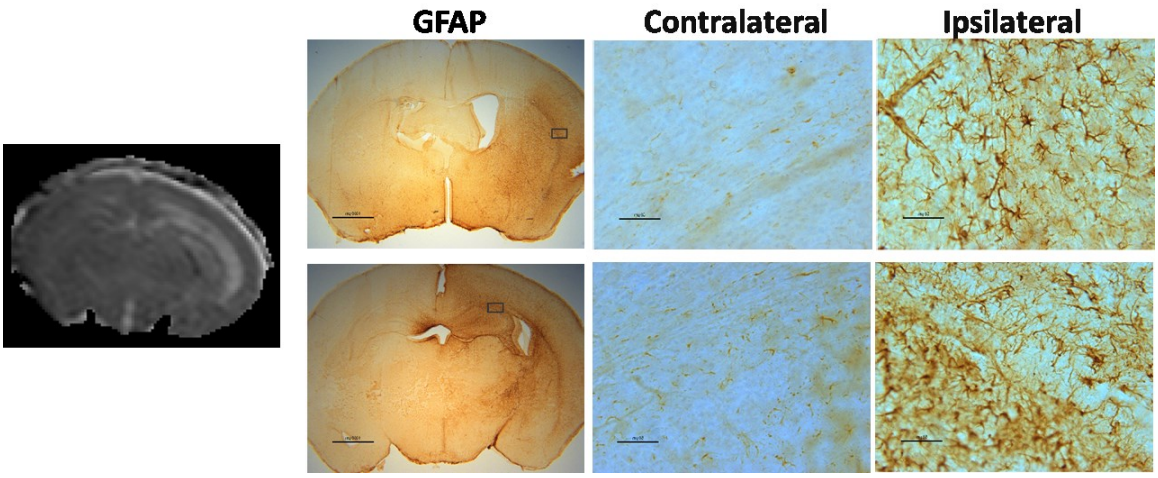

Figure 7.4: Glial fibrillary acidic protein (GFAP) stained sections from two coronal sections of a mild injury mouse at 24hrs after injury. At high magnification, drastic astrocytic swelling was found in the ipsilateral brain. Scale bars at low and high magnification is 1000 μm and 50 μm, respectively.

At a subcellular level, the organelles such as the mitochondria is highly sensitive to the energy failure and neurotoxicity after HI. Superoxide dimustase-2 (SOD2) as a mitochondrial matrix protein was used to evaluate for mitochondrial swelling. All of the 3 hour animals show mitochondrial swelling in the ipsilateral hemisphere in hippocampus CA1. In Fig. 7.5C, some of the mitochondrial have swollen to 1-2 microns and they also form swollen mitochondrial aggregates or clumps. The swelling was likely due the influx

of water and calcium brought about by mitochondrial permeability transition. Water becomes trapped and confined in mitochondria until they rupture.

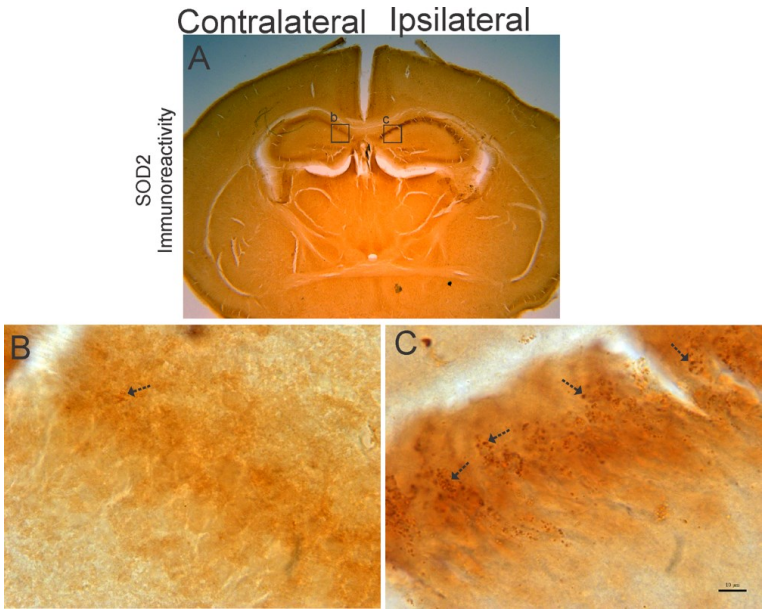

Figure 7.5: Superoxide dismutase 2 (SOD2) stained section from a mild injury mouse at 3hrs after injury. At high magnification, the mitochondria in the hippocampal CA1 field showed severe swelling, which also form swollen mitochondrial aggregates or clumps. Scale bars at high magnificaiton is 10 μm.

7.3.3 Subtle microstructural changes in the cerebral cortex

In the mild injury mice, although the lesion was most prominent in EC and CA1 areas, we found the cerebral cortex also demonstrated subtle abnormality, comparing the ipsilateral and contralateral cortices. In Fig. 7.5(A), the ADC at 200Hz was slightly higher in the ipsilateral cortex, and the difference was more prominent from the Δ*f*ADC map

(yellow arrow). Interestingly, this injury pattern agreed well with the perfusion map, measured by arterial spin labeling [ref]. Quantitative analysis (Fig. 7.5(B)) also revealed the difference between the ipsilateral and contralateral Δ*f*ADC was significantly higher in the mild injury mice (n = 12) compared to the sham mice (n = 7). The difference was not shown from conventional PGSE measurements (Fig. 7.5(C)).

The subtle injury in the cortex was also demonstrated in the MAP2 staining of the mild injury mice at 3hrs after injury (Fig. 7.6). In the ipsilateral cortex, swollen dendritic processes were identified (C, hatched arrows), and dendritic bundlingwas apparent.

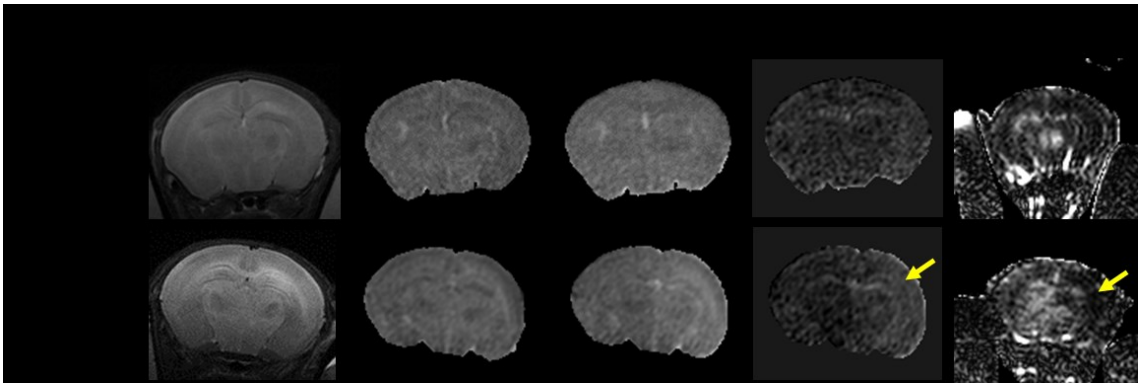

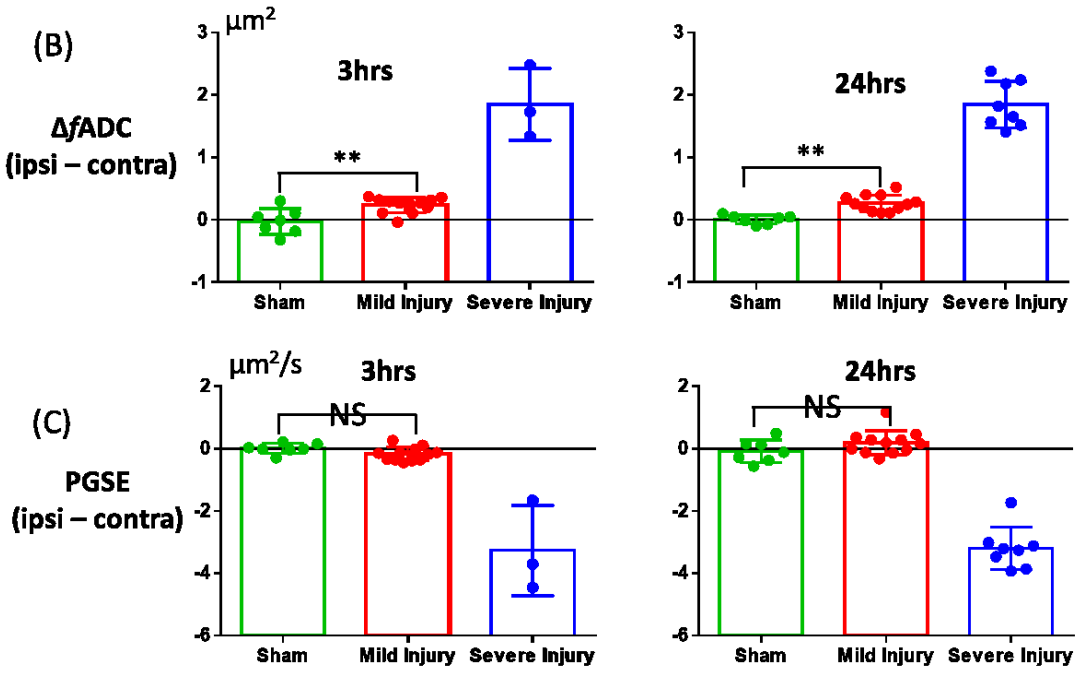

Figure 7.5: (A) T2-weighted images, PGSE and OGSE (200Hz) maps, Δ*f*ADC map, and perfusion map of a mild injury mice at 3hrs and 24hrs after injury. (B-C) Ipsilateral and contralateral differences at 3hrs and 24hrs after injury in the sham group ($n = 7$), mild injury group ($n = 7$), and severe injury group ($n = 3$), evaluated with Δ*f*ADC values and PGSE-ADC values, respectively.

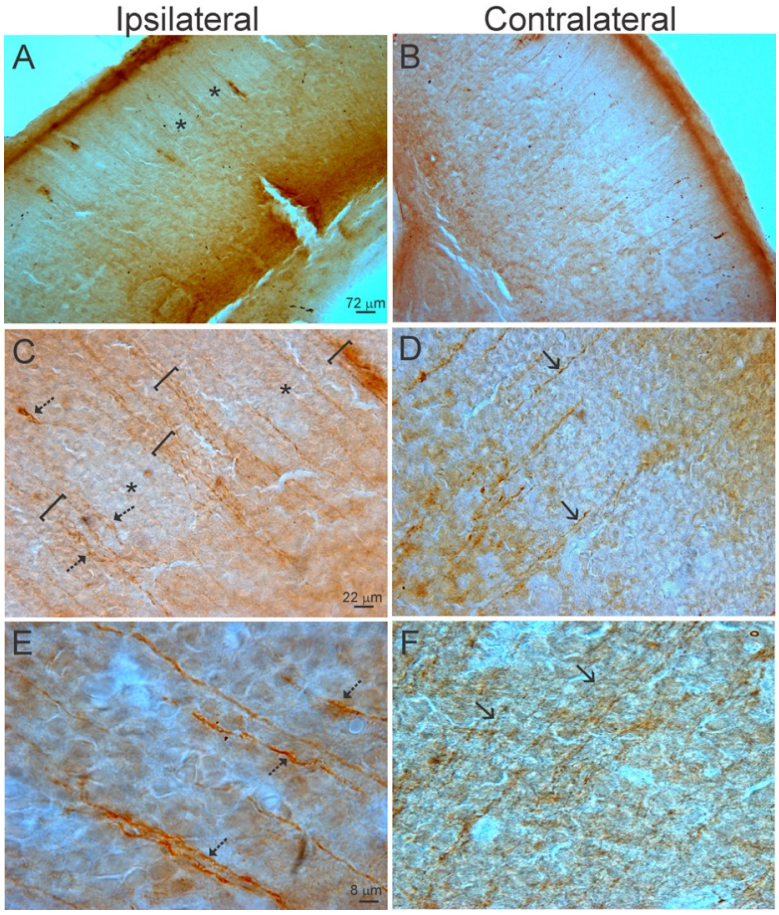

Figure 7.6: Immunoperoxidase staining for microtubule-associated protein 2 (MAP2) in ipsilateral (A,C,E) and contralateral (B,D,F) parietal cortex of a P10 HI mouse at 3 hours recovery. A patchy pattern of MAP2 immunostaining is observed in ipsilateral cortex (A) that is not apparent in contralateral cortex (B). Asterisks in A identify low-staining barrels in C. In ipsilateral cortex (C) bundles of swollen dendrites (brackets) are observed. Individual swollen dendritic profiles are identified (C, hatched arrows). In contralateral cortex (D) the dendrites are largely free of dilations (solid arrows) and dendritic bundling is less apparent. At higher magnification (E), vacuolation and bloating of single dendrites is seen in ipsilateral cortex (hatched arrows) , while in contralateral cortex (F) MAP2 staining is generally very delicate and distributed in a network within the cortical neuropil (solid arrows). Scale bars is 72 µm in (A-B), 22 µm in (A-B), and 8 µm in (A-B).

7.4 Discussion

In this study, we focused on investigating the MR signature and pathology of subtle HI injury. Our results demonstrated that OGSE measurements enhanced the sensitivity in detecting subtle edema, and unique contrast of OGSE reveals more extensive injuries compared to the conventional PGSE. For example, the microstructural changes in the hippocampal CA1 field is better characterized at high oscillating frequencies, which relates to cellular levels of injury such as the astrocytes activation and subcellular injury such as mitochondrial swelling. Because of short diffusion time accessible in OGSE, these small changes of microstructures (~2-3 microns) can be possibly probed.

We found interesting diffusion time dependent ADC changes in the CA1 and EC of the mild injury mice. Periventricular white matter injury in rodent models of mild HI injury was established in earlier studies with hyperintensive T2-weighted signal and ADC (73,103,295,299), which suggested vasogenic edema accompanying damage in the oligodendrocytes. Our data showed similar high ADC at PGSE, as well as other oscillating frequencies, which further increased from 3hrs to 24hrs in the ipsilateral EC. Interestingly, the contralateral ADC decreased from 3hrs to 24hrs, which may related to developmental change that was also observed in the sham mice. In addition, the contralateral ADC were

slightly different from the sham mice at 3hrs, which may result from the transient effect of hypoxia to the contralateral brain.

Lodygensky et al. (296) reported CA1 injury using a similar neonatal HI model in the P7 mice, where the authors found ADC reduction in CA1 at 24hrs after injury and associated it with caspase-3 activation and apoptosis (300). This study examined P10 injury at 3hrs and 24hrs after HI, using multi-frequency dMRI measurements. At 3hrs, the individual ADC measurements (0-200Hz) did not show differences, but the Δ*f*ADC revealed enhancement in the CA1 layer. At 24hrs, the ipsilateral ADC values (0-200Hz) were significantly higher than the contralateral side, and the difference was enhanced at high oscillating frequencies, leading to an extended region of hyperintensive ADC along with the surrounding white matter.

Moreover, the subtle edema in the cerebral cortex as revealed from OGSE and Δ*f*ADC measurements showed interesting injury pattern that correlates with the perfusion deficits. Dendritic dilation as evidenced in the MPA2 staining seems to support the OGSE findings.

7.5 Conclusion

We examined a wide range of brain injury in a neonatal mouse model of hypoxia-ischemia using OGSE dMRI at acute and subacute stages. The OGSE measurement is shown to be highly sensitive to small scale microstructural changes, such as swelling of astrocytic processes and mitochondria.

Chapter 8 Pseudo-diffusion suppressed hybrid pulsed and oscillating gradient diffusion MRI for clean OGSE measurement

8.1 Introduction

Oscillating gradient spin-echo (OGSE) diffusion MRI has recently drawn attentions due to its ability to distinguish tissue microstructures at varying length scales (1-5). In the last decade, it has been increasingly used to extract unique tissue contrasts and probe microstructural in healthy tissues, such as normal *in vivo* (6-8) or *ex vivo* (9-14) rodent brains; and to characterize pathological microstructural changes in disease models, such as brain tumor (15,16) and ischemia (2,8,17). However, applications of this technique in human studies (18,19) remained limited due to the relatively limited gradient strength available on current clinical MR systems (<100 mT/m). Because the diffusion attenuation factor (b-value) decreases rapidly with the increase of oscillating frequency ($b \propto 1/f^3$) for OGSE diffusion MRI, the achievable b-value is inevitably low with common clinical gradients, e.g. b = 200-300 s^2/mm for oscillating frequencies of 50-60 Hz (18,19).

At this low b-value regime, the sensitivity of OGSE diffusion MRI to tissue microstructure is reduced, and the so-called pseudo-diffusion related to tissue perfusion can no longer be ignored and may affect the apparent diffusion coefficient (ADC) measure. This is because blood flow in randomly oriented capillaries (at the voxel level) mimics a random walk ("pseudo-diffusion"), commonly known as the intravoxel incoherent motion (IVIM) (20,21). Although the IVIM can be a useful measure of microscopic perfusion (22-24) in addition to bulk perfusion, it confounds the real diffusion signal and is therefore called pseudo-diffusion. It is known that conventional pulsed gradient spin echo (PGSE) diffusion signals measured at low b values contain pseudo-diffusion, which can be separated using bi-exponential fitting (21) with a series of ADC measurements from multiple b-values. In this study, we hypothesized that OGSE measurements at low b-values are susceptible to the pseudo-diffusion effect and proposed a new sequence that combined orthogonal pulsed and oscillating gradients to suppress the contributions from pseudo-diffusion. *In vivo* experimental data from adult mouse brains were used to test the effects of pseudo-diffusion on OGSE signals at different oscillating frequencies and whether the hybrid sequence was able to achieve accurate OGSE measurements at low b-values (< 300 s^2/mm).

8.2 Methods

8.2.1 Theory

The basic idea is to superimpose a baseline pulsed gradient to the oscillating gradient (Fig. 1A), as well as to the non-diffusion weighted (b_0) scan. Since the diffusion temporal spectrum follows a Fourier relationship with the gradient integral ($|F(\omega)| = \mathcal{F}\left(\int_0^t g(\tau)d\tau\right)$), which is a linear transformation, superimposing of the pulsed and oscillating gradient leads to a linear combination of their spectra in the Fourier space. Using the baseline signal from the pulsed gradient in the b0 image, we can still obtain ADC from the oscillating gradient:

$$ADC^* = -\frac{1}{b_{hybrid} - b_{PGSE}} \log\left(\frac{S_{hybrid}}{S_{PGSE}}\right) \qquad \text{Equation 8.1}$$

With the addition of the PGSE gradient, b-value of the hybrid gradient can be significantly increased even with limited total gradients. Therefore, the contribution of the pseudo-diffusion can be suppressed due to the extra diffusion attenuation from PGSE, because

$$\left|\frac{S_{hybrid}}{S_{PGSE}}\right| = \left|\frac{f \cdot e^{-D^* \cdot (b1+b2)} + (1-f) \cdot e^{-D \cdot (b1+b2)}}{f \cdot e^{-D^* \cdot b2} + (1-f) \cdot e^{-D \cdot b2}}\right| = \left|\frac{e^{-D^* \cdot b1} + \frac{1-f}{f} e^{(D^*-D) \cdot b2 - D \cdot b1}}{1 + \frac{1-f}{f} e^{(D^*-D) \cdot b2}}\right| \approx e^{-D \cdot b1}$$

Equation 8.2

Since $\frac{1-f}{f} \gg 1$ and $e^{(D^*-D)\cdot b2} \gg 1$.

where $b1$ and $b2$ denotes the b-values from the oscillating gradient (g1) and the pulsed gradient (g2), respectively; and D and D^* denotes the diffusion coefficients of the true water diffusion and pseudo-diffusion, respecitvely.

This approach, however, will result in nonlinear relationship between the b-values of pulsed/oscillating gradients and the resulting b-value of the hybrid gradient. This is shown in the following equation:

$$b = \gamma^2 \int \left[\int_0^t g(\tau) d\tau \right]^2 dt = \gamma^2 \int \left[\int_0^t g_1(\tau) + g_2(t) d\tau \right]^2 dt$$
$$= \gamma^2 \int \left[\int_0^t g_1(\tau) d\tau \right]^2 dt + \gamma^2 \int \left[\int_0^t g_2(\tau) d\tau \right]^2 dt + \gamma^2 \int \left[\int_0^t g_1(\tau) d\tau \int_0^t g_2(\tau) d\tau \right] dt$$

Equation 8.3

Since the third term in Equation 8.2 is a non-zero entry, the b-value is not a simple summation of the b1 from the pulsed gradient and b1 from the oscillating gradient ($b \neq b1+b2$). Also the temporal diffusion power spectrum ($|F(\omega)|^2$) of the combined gradient is not a linear combination of the pulsed and oscillating gradients' integral spectra (Fig. 1A).

Our solution is to place the pulsed and oscillating gradients on orthogonal directions. In this way. The hybrid gradient waveform can be expressed as a complex number (g = g1+i*g2) (Fig. 1B). $|F(\omega)|^2$ of this hybrid gradient then becomes a linear combination of

the power spectra of the individual gradients (Fig. 1B). The b-value of the hybrid gradient waveform can be calculated based on the complex representation:

$$b = \gamma^2 \int \left[\int_0^t g(\tau) d\tau \right]^2 dt = \gamma^2 \int \left[\int_0^t g_1(\tau) + i \cdot g_2(t) d\tau \right]^2 dt$$
$$= \gamma^2 \int \left[\int_0^t g_1(\tau) d\tau \right]^2 dt + \gamma^2 \int \left[\int_0^t g_2(\tau) d\tau \right]^2 dt + \gamma^2 \int \left[i \int_0^t g_1(\tau) d\tau \int_0^t g_2(\tau) d\tau \right] dt \quad \text{Equation 8.3}$$

where the third term (imaginary part) does not contribute to diffusion attenuation, and therefore, b-values from the two orthogonal gradients are linearly addable ($b = b1+b2$).

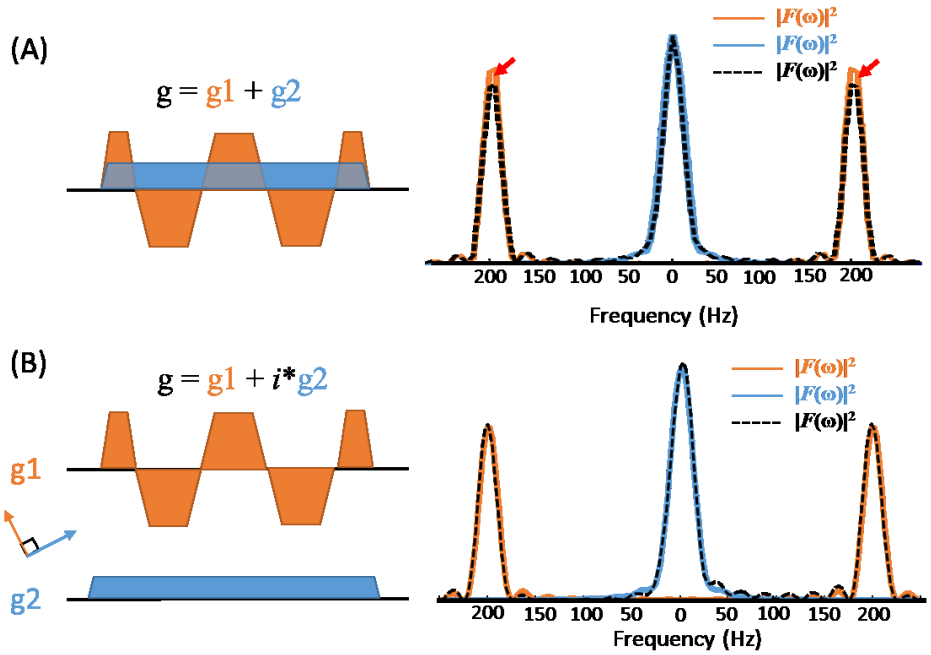

Figure 8.1: Hybrid pulsed and oscillating gradients in two schemes of combinations. (A) Direction superposition of pulsed (g1) and oscillating (g2) gradients in the same diffusion direction and the resultant temporal diffusion power spectrum ($|F(\omega)|^2$). Red arrows mismatched between the power spectrum of the hybrid gradient and the superposed spectra of the pulsed and oscillating gradient. (B) Hybrid gradient consist of orthoganally oriented pulsed and oscillating gradients. The diffusion power spectrum of this hybrid gradient overlaps with the superposed spectra of the pulsed and oscillating gradient.

8.2.2 Image Acquisition

In vivo tests of the hybrid sequence were performed on normal C57BL/6J adult mice (Male, 3 month-old, *n*=5) on an 11.7 T horizontal NMR spectrometer (maximum gradient strength = 760 mT/m) with 72 mm quadrature volume transmitter and a 10 mm diameter receive-only planner surface coil. The hybrid sequence consists of pulsed gradients according to gradient table B1 below (the three numbers in each row indicate the distribution of the gradient along the x, y, and z gradient axes), and orthogonally orientated cosine-trapezoid oscillating gradients according to gradient table B2.

$$B1 = \begin{bmatrix} 0 & 0 & 1 \\ 1 & 0 & 0 \\ 0 & 1 & 0 \\ 0 & 0 & 1 \\ 1 & 0 & 0 \\ 0 & 0 & 1 \end{bmatrix} \text{ and } B2 = \begin{bmatrix} 1 & 1 & 0 \\ 0 & 1 & 1 \\ 1 & 0 & 1 \\ 1 & 1 & 0 \\ 0 & 1 & 1 \\ 1 & 1 & 0 \end{bmatrix}$$

T2-weighted images were acquired with an echo time (TE) / repetition time (TR) = 50/2000 ms, field of view (FOV) = 16 mm x 16 mm, in-plane resolution = 0.08 mm x 0.08 mm, and fives slices with slice thickness = 1 mm (the second slice cut through the anterior commissure). High b-value PGSE images were acquired for anatomical definition: TE/TR = 21/2000 ms, four-segment EPI readout, one signal average, diffusion duration

(δ)/diffusion separation (Δ) = 4/12 ms, and 30 diffusion directions (25) with b = 1000 s/mm^2. Two sets of diffusion experiments were performed:

(A) ADC measurements at multiple b-values were acquired at TE/TR = 32/2000 ms, four-segment EPI readout, two signal average, in-plane resolution = 0.17 mm x 0.17 mm, and was later interpolated to 0.08 mm x 0.08 mm (co-registered to the T2-weighted image). Conventional PGSE was scanned with δ / Δ = 10/13.2 ms, six diffusion directions as listed in gradient table B1, and b = 50-1000 s/mm^2. Conventional OGSE (OGSE only) was scanned with diffusion duration = 10 ms, six diffusion directions as listed in gradient table B2, oscillating frequency of 100Hz (number of cycles N = 1 and b = 50-700 s/mm^2) and 200Hz (N = 2 and b = 50-300 s/mm^2). The hybrid OGSE was performed with the same parameters as the OGSE-only scans with the addition of PGSE gradient of b = 300 s/mm^2.

(B) ADC measurements at multiple oscillating frequency (0-300Hz) were acquired at TE/TR = 52/2000 ms, four signal average, and the same imaging resolution as in (A). PGSE data was scanned with δ / Δ = 20/23.2 ms, six diffusion directions, and b = 500 s/mm^2. OGSE-only data was scanned with diffusion duration = 20 ms, six diffusion directions, b = 200 s/mm^2, N = 1, 2, 3, 4, 5, 6 for oscillating frequencies of 50Hz, 100Hz, 150Hz, 200Hz,

250Hz, and 300Hz, respectively. The hybrid OGSE was performed with the same parameters as the OGSE-only scans with the addition of PGSE gradient of b = 300 s/mm^2.

8.2.3 Data analysis

The pseudo-diffusion suppressed ADCs (ADC* from Equation 8.1) were averaged over six diffusion directions to obtain isotropic diffusion weighting. The diffusion tensor can also be obtained from the hybrid diffusion data by log-linear fitting of the ADC* calculated from each diffusion direction. Fractional anisotropy (FA) map was calculated from the 30 diffusion direction high b-value diffusion data for region of interest (ROI) definition.

The signal-to-noise ratio was evaluated based on the b_0 images, calculated as the mean signal in the predefined ROI divided by the standard deviation of the background signal. The noise level in the ADC maps was evaluated using coefficient of variation (CV), which is ratio between the standard deviation of the ADC values to the mean ADC in the predefined ROIs.

Data was presented as mean value ± standard error of mean (SEM) (n = 5). Statistical analysis was performed to evaluate the effects of pseudo-diffusion (OGSE-only versus

hybrid) and b-value in Experiment A, or the effects of pseudo-diffusion and oscillating frequency in Experiment B, using two-way analysis of variation (ANOVA) with repeated measures in GraphPad Prism (http://www.graphpad.com/scientific-software/prism). Bonferroni post-tests (26) was performed to compare the statistical differences between OGSE-only and hybrid sequences at each b-value in Experiment A, or the differences at each oscillating frequency in Experiment B. $p < 0.001$ was regarded highly significant, $p < 0.01$ was regarded significant, and $p > 0.05$ was regarded non-significant (NS).

8.3 Results

We focused on the mouse cortex in this study, which has sufficient blood supply, relatively homogenous microstructures, and high SNR due to the sensitivity profile of the planner surface coil. The SNR of the b_0 images in the cortical region was 103.3 ± 16.3 (n = 5) in Experiment A when short TR was used, and 87.2 ± 17.1 in Experiment B when long TR was used. Figure 8.2(A) show coronal sections of the ADC maps acquired using the conventional OGSE sequence and the proposed hybrid OGSE sequence at different frequencies and b-values. The hybrid OGSE-ADC maps were slightly darker than that from the OGSE-only sequence at b = 200 s/mm^2. The ADC maps showed relatively low contrast-

to-noise ratio at b = 200 s/mm^2, when the signal decay was 12.7 ± 0.7 % (n = 5). The CV of ADC values measured in the cortical ROI indicated a higher noise level in the OGSE-only ADC maps, compared to that in the hybrid OGSE ADC maps ($p < 0.0001$) (Figure 8.2(B)), especially in the low b-value regime. Post-hoc Bonferroni tests showed no statistical differences in CV measured from the two sequences, except at b = 50 s/mm^2 ($p < 0.001$).

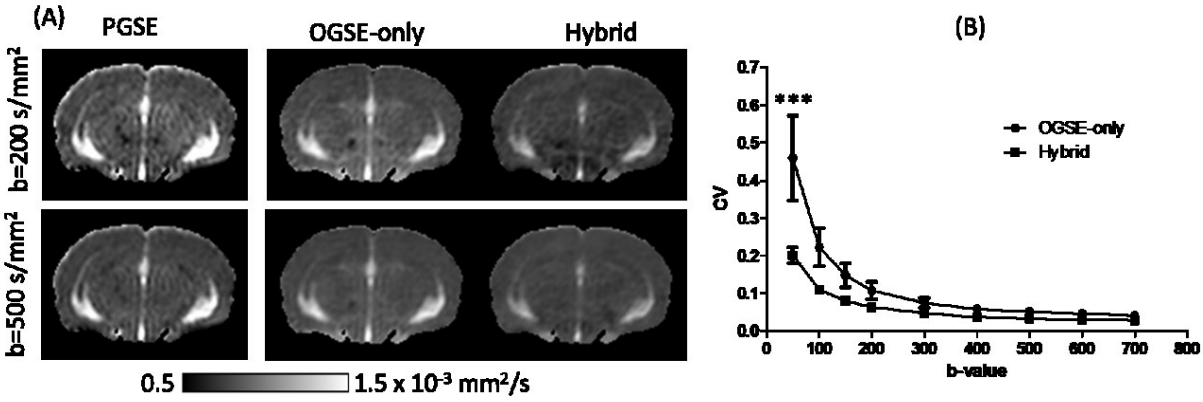

Figure 8.2: (A) PGSE and OGSE ADC maps (100Hz) of a mouse brain, acquired using convetional PGSE, OGSE sequence (OGSE-only) and the proposed hybrid OGSE sequences at b-values of 200 mm^2/s (top row) and 500 mm^2/s (bottom row). (B) Coefficient of variation (CV) calculated in the cortical region of the OGSE-only and hybrid OGSE maps, at b-values of 50-700Hz.

Effects of pseudo-diffusion were observed in both PGSE and OGSE-only measurements in the cortical region (solid lines in Figure 8.3(B), based on the ROIs defined in Figure 8.3(A)), characterized by higher ADC values at low b-values (e.g., 50 s/mm^2)

compared to those at moderate or high b-values (>300 s/mm^2). With the hybrid pulsed and oscillating gradient sequence, the pseudo-diffusion effect was suppressed (dashed lines in Fig. 8.3(B)), and the derived ADC-values (ADC*(100Hz and 200Hz)) showed no significant difference over the range of b-values (p = 0.1 and 0.7 respectively, one-way ANOVA). Two-way ANOVA analysis of the OGSE measurements at different frequencies showed significant differences between the OGSE-only measurements and the hybrid OGSE measurements ($p < 0.0001$ at both 100Hz and 200Hz). Bonferroni post-tests showed the differences were significant between ADC (100Hz) and ADC*(100Hz) over the b-value range of 50-150 mm^2/s (blue stars), and between ADC(200Hz) and ADC*(200Hz) over the b-value range of 50-100 mm^2/s (red stars). At b values greater than 200 mm^2/s, the OGSE-only measurements showed no apparent change with increasing b-values, and the OGSE* and the OGSE-only curves arrived at the same ADC values, presumably clear of the effects of pseuodiffusion. The results suggested that the hybrid sequence was able to suppress the effects of pseudo-diffusion.

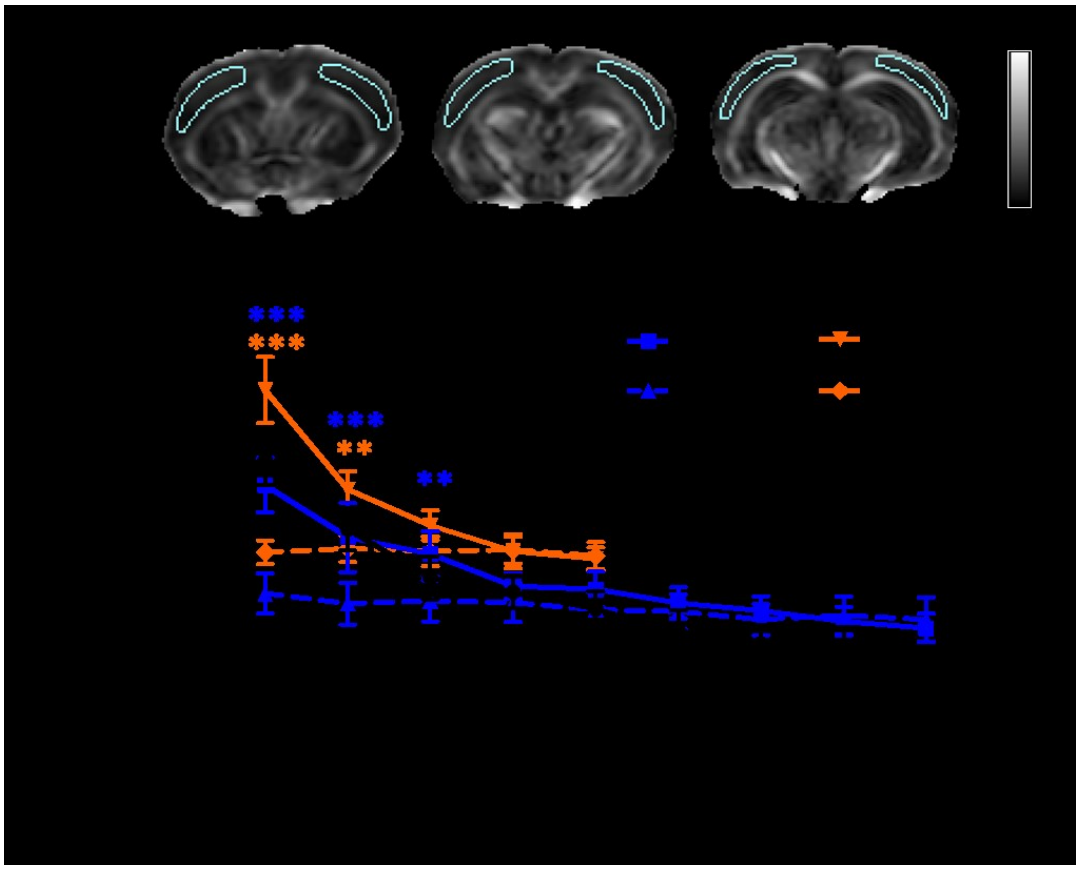

Figure 8.3: ADC measumrents from the conventional PGSE sequence, OGSE-only sequence (100 Hz and 200Hz), and the hybrid OGSE sequence (100Hz* and 200Hz*), over the b-value range of 50-700 mm^2/s. The data was presented as mean ± standard error of mean (SEM) ($n = 5$). The cortical region of interet (ROI) is defined based on the fractional anisotropy (FA) maps. Blue stars and red stars indicates the statistical significance of the differences between 100Hz and 100Hz*, and between 200Hz and 200Hz*, respectively. Note: *** denotes $p < 0.001$, ** denotes $p < 0.01$ from the Bonferroni post-tests.

The contribution from the pseudo-diffusion may alter the time-dependence of the ADC measurements, which is dictated by underlying tissue microstructure. We evaluated the ADC values measured over the oscillating frequency range of 0-300Hz, using the OGSE-only sequence and the hybrid OGSE sequence at b-value of 200 mm^2/s. Although the

pseudo-diffusion is relatively low at b-value = 200 mm^2/s, but its effect is not negligible as show in Figure 8.4(A), especially at high oscillating frequencies. Two-way ANOVA analysis of the data revealed significant difference between OGSE-only group and the hybrid OGSE group ($p < 0.0001$), and the post-hoc Bonferroni tests showed the differences were most evidential at 200 Hz and 300Hz ($p < 0.001$). It was noticed that if the ADC values were plotted against the square root of oscillating frequency, the frequency-dependent ADC changes follows a linear regression (Figure 8.4(B), $R^2 = 0.55$), according to (27,28). The slopes of the linear fitting were $11.15 \pm 1.8 \times 10^{-6}$ $mm^2 \cdot s^{-1/2}$ for the OGSE-only measurements, and $8.86 \pm 1.4 \times 10^{-6}$ $mm^2 \cdot s^{-1/2}$ ($p = 0.31$, $n = 5$).

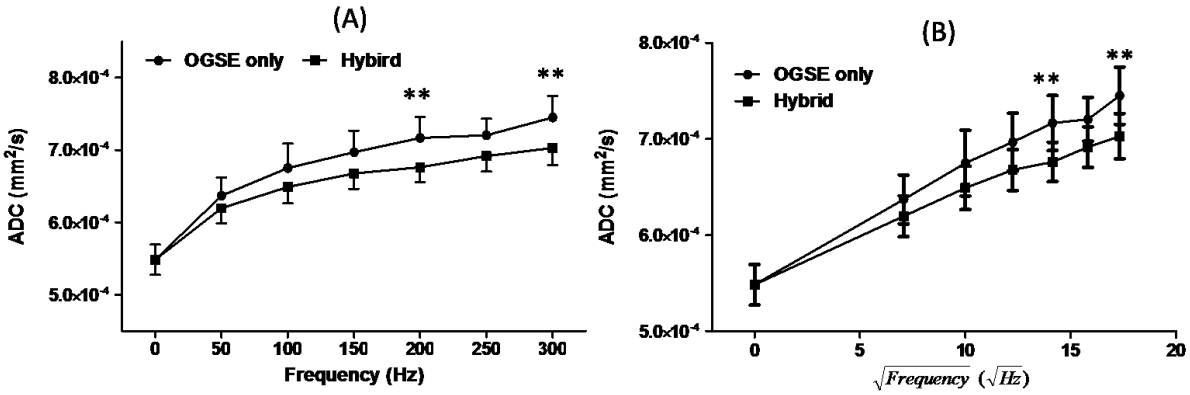

Figure 8.4: ADC values obtained from the OGSE-only sequence and the Hybrid OGSE sequence over the frequency range of 0-300Hz, and plotted against the oscillating frequncy (A) or the square root of frequency (B). Note ** denotes $p < 0.01$ from the Bonferroni post-tests.

We further demonstrated that the hybrid OGSE sequence were able to acquire diffusion tensor data by fitting the ADC* (Equation 8.4) from six or more diffusion directions. Figure 8.5 showed the direction-encoded colormaps reconstructed from the conventional OGSE and hybrid OGSE tensors at b-values of 300 mm^2/s and 600 mm^2/s. The tensors from two sequences revealed the same tissue orientational information, such as that in the cortex and white matter regions. The colormaps at low b-value major contained noise due to the low contrast-to-noise ratio, but the major white matter structures can be delineated, e.g., the corpus callosum (cc), fimbria (fi), cerebral peduncle (cp), and optic tract (opt). The ripples in the OGSE-only colormaps resulted from the imaging artifacts in the non-diffusion weighted image (e.g. insufficient crusher gradients), which was suppressed by the additional PGSE gradient in the hybrid sequence.

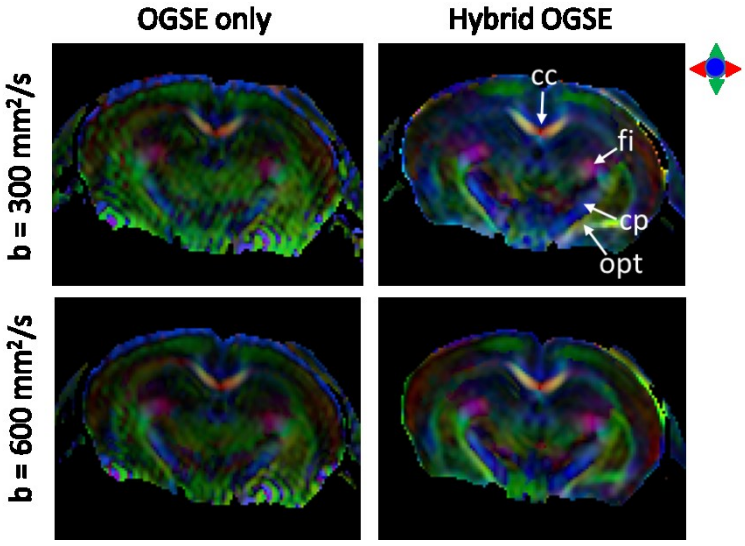

Figure 8.5: Direction-encoded colormaps reconstructed from the conventional OGSE and hybrid OGSE tensors at b-values of 300 s/mm^2 and 600 s/mm^2. Abbreviation: cc- corpus callosum, fi- fimbria, cp- cerebral peduncle, opt- optical tract.

8.4 Discussion

In this study, we first investigated the role of pseudo-diffusion on OGSE measurements in the low b-value regime, which was frequently encountered in clinical applications. In previous human brain OGSE studies (18,19), even with the trapezoid cosine gradient, low oscillating frequencies (50-60Hz), and many oscillating cycles, the highest achievable b-value was only in the range of 200-300 s/mm^2. Our experiments showed that the conventional OGSE signal was contaminated by the pseudo-diffusion at low b-values (Figure 8.2), e.g., the ADC was significantly higher than the true ADC (from high b-values). Using the hybrid OGSE sequence with orthogonally placed pulsed and oscillating gradient, we demonstrated that the contribution from pseudo-diffusion was removed and clean OGSE signal could be obtained at very low b-values. The results indicates that the proposed new sequence can be a solution to achieve accurate OGSE measurements on clinical scanners. It is valuable for *in vivo* studies on preclinical scanners, since it offer the possibility to reach higher oscillating frequency, which may offers extra

microstructural information beyond the current scope. Also, fewer oscillating cycles may be used to reduce the echo time and thus improve signal-to-noise ratio. We also realized that even though accurate OGSE-ADC can be achieved at low b-values using the hybrid OGSE, the contrast-to-noise ratio remains low, which introduced noise in the ADC measurement. Improving the SNR in the raw data can be a rescue, e.g. using high sensitivity coils.

Another important question is whether the pseudo-diffusion impacts OGSE signals of different oscillating frequency in a different manner. Our data of OGSE measurements from 0-300Hz (Figure 8.3) indicated that the pseudo-diffusion contribution is higher at high oscillating frequencies (200-300Hz), and lower at low frequencies. Therefore, pseudo-diffusion may alter time-dependence of the ADC measurements or the temporal diffusion spectrum, which is characteristic of the tissue microstructure. The slopes of linear regression of ADC against the square root of oscillating frequency was higher with pseudo-diffusion, compared to that without pseudo-diffusion. But there was no statistical difference between the two slopes, possibly due to relatively low pseudo-diffusion at b = 200 s/mm^2 and the high individual differences in cerebral perfusion. In order to know the exact fraction of pseudo-diffusion at different oscillating frequencies, bi-exponential fitting

with multiple b-value measurements is needed, which however, specially designed high gradients to reach the high b-value regime.

8.5 Conclusion

We proposed a hybrid OGSE sequence with orthogonally oriented pulsed and oscillating gradients to suppress pseudo-diffusion at low b-values. The pseudo-diffusion is present in both PGSE and OGSE measurements, and may alter the time-dependent ADC characteristics. With the hybrid sequence, accurate OGSE-ADC can be obtained in the low b-value regime, which is important for clinical applications of OGSE technique with limited gradient.

Bibliography

1. Bernstein MA, King KF, Zhou X. Handbook of MRI Pulse Sequences. Burlington, MA, USA: Elsevier Academic Press: 2004.
2. Nishimura DG. Principles of magnetic resonance imaging: Stanford Univ: 1996.
3. Edelstein WA, Hutchison JMS, Johnson G, Redpath T. Spin Warp Nmr Imaging and Applications to Human Whole-Body Imaging. Phys Med Biol 1980;25(4):751-756.
4. Lauterbur PC. Image formation by induced local interactions: examples employing nuclear magnetic resonance. Nature 1973;242(5394):190-191.
5. Lebihan D, Breton E, Lallemand D, Grenier P, Cabanis E, Lavaljeantet M. Mr Imaging of Intravoxel Incoherent Motions - Application to Diffusion and Perfusion in Neurologic Disorders. Radiology 1986;161(2):401-407.
6. Taylor DG, Bushell MC. The Spatial-Mapping of Translational Diffusion-Coefficients by the Nmr Imaging Technique. Phys Med Biol 1985;30(4):345-349.
7. Merboldt KD, Hanicke W, Frahm J. Self-Diffusion Nmr Imaging Using Stimulated Echoes. J Magn Reson 1985;64(3):479-486.
8. Beaulieu C. The basis of anisotropic water diffusion in the nervous system - a technical review. NMR in biomedicine 2002;15(7-8):435-455.
9. Torrey HC. Bloch Equations with Diffusion Terms. Phys Rev 1956;104(3):563-565.
10. Stejskal EO, Tanner JE. Spin diffusion measurements: spin echoes in the presence of a time-dependant field gradient . J Chem Phys 1965;42:288-292.
11. Derek KJ. Diffusion MRI: Theory, Methods, and Applications: Oxford University Press: 2010.
12. Tanner JE. Intracellular diffusion of water. Archives of biochemistry and biophysics 1983;224(2):416-428.
13. Basser PJ, Mattiello J, LeBihan D. Estimation of the effective self-diffusion tensor from the NMR spin echo. Journal of magnetic resonance Series B 1994;103(3):247-254.
14. Crank J. The Mathematics of Diffusion. Oxford, UK: Oxford University Press: 1975.

15. Mattiello J, Basser PJ, Lebihan D. Analytical Expressions for the b Matrix in NMR Diffusion Imaging and Spectroscopy. Journal of Magnetic Resonance, Series A 1994;108(2):131-141.
16. Song SK, Sun SW, Ramsbottom MJ, Chang C, Russell J, Cross AH. Dysmyelination revealed through MRI as increased radial (but unchanged axial) diffusion of water. Neuroimage 2002;17(3):1429-1436.
17. Beaulieu C. The basis of anisotropic water diffusion in the nervous system - a technical review. Nmr Biomed 2002;15(7-8):435-455.
18. Callaghan PT. Principles of Nuclear Magnetic Resonance Microscopy. New York: Oxford University Press: 1991.
19. Tuch DS. Q-ball imaging. Magnetic resonance in medicine : official journal of the Society of Magnetic Resonance in Medicine / Society of Magnetic Resonance in Medicine 2004;52(6):1358-1372.
20. Assaf Y, Basser PJ. Composite hindered and restricted model of diffusion (CHARMED) MR imaging of the human brain. Neuroimage 2005;27(1):48-58.
21. Assaf Y, Blumenfeld-Katzir T, Yovel Y, Basser PJ. AxCaliber: a method for measuring axon diameter distribution from diffusion MRI. Magnetic resonance in medicine : official journal of the Society of Magnetic Resonance in Medicine / Society of Magnetic Resonance in Medicine 2008;59(6):1347-1354.
22. Zhang H, Schneider T, Wheeler-Kingshott CA, Alexander DC. NODDI: practical in vivo neurite orientation dispersion and density imaging of the human brain. Neuroimage 2012;61(4):1000-1016.
23. Wang Y, Wang Q, Haldar JP, et al. Quantification of increased cellularity during inflammatory demyelination. Brain : a journal of neurology 2011;134(Pt 12):3590-3601.
24. Jensen JH, Helpern JA, Ramani A, Lu H, Kaczynski K. Diffusional kurtosis imaging: the quantification of non-gaussian water diffusion by means of magnetic resonance imaging. Magnetic resonance in medicine : official journal of the Society of Magnetic Resonance in Medicine / Society of Magnetic Resonance in Medicine 2005;53(6):1432-1440.
25. Alexander DC, Barker GJ, Arridge SR. Detection and modeling of non-Gaussian apparent diffusion coefficient profiles in human brain data. Magnetic resonance in medicine : official journal of the Society of Magnetic Resonance in Medicine / Society of Magnetic Resonance in Medicine 2002;48(2):331-340.

26. Shemesh N, Ozarslan E, Komlosh ME, Basser PJ, Cohen Y. From single-pulsed field gradient to double-pulsed field gradient MR: gleaning new microstructural information and developing new forms of contrast in MRI. Nmr Biomed 2010;23(7):757-780.
27. Does MD, Parsons EC, Gore JC. Oscillating gradient measurements of water diffusion in normal and globally ischemic rat brain. Magnetic resonance in medicine : official journal of the Society of Magnetic Resonance in Medicine / Society of Magnetic Resonance in Medicine 2003;49(2):206-215.
28. Conturo TE, Lori NF, Cull TS, et al. Tracking neuronal fiber pathways in the living human brain. P Natl Acad Sci USA 1999;96(18):10422-10427.
29. Mori S, Crain BJ, Chacko VP, van Zijl PCM. Three-dimensional tracking of axonal projections in the brain by magnetic resonance imaging. Ann Neurol 1999;45(2):265-269.
30. Behrens TEJ, Woolrich MW, Jenkinson M, et al. Characterization and propagation of uncertainty in diffusion-weighted MR imaging. Magnet Reson Med 2003;50(5):1077-1088.
31. Koch MA, Norris DG, Hund-Georgiadis M. An investigation of functional and anatomical connectivity using magnetic resonance imaging. Neuroimage 2002;16(1):241-250.
32. Parker GJM, Alexander DC. Probabilistic Monte Carlo based mapping of cerebral connections utilising whole-brain crossing fibre information. Lect Notes Comput Sc 2003;2732:684-695.
33. Tuch DS, Reese TG, Wiegell MR, Makris N, Belliveau JW, Wedeen VJ. High angular resolution diffusion imaging reveals intravoxel white matter fiber heterogeneity. Magnetic resonance in medicine : official journal of the Society of Magnetic Resonance in Medicine / Society of Magnetic Resonance in Medicine 2002;48(4):577-582.
34. Tournier JD, Calamante F, Connelly A. Robust determination of the fibre orientation distribution in diffusion MRI: Non-negativity constrained super-resolved spherical deconvolution. Neuroimage 2007;35(4):1459-1472.
35. Thomas C, Ye FQ, Irfanoglu MO, et al. Anatomical accuracy of brain connections derived from diffusion MRI tractography is inherently limited. P Natl Acad Sci USA 2014;111(46):16574-16579.

36. Van Essen DC, Smith SM, Barch DM, et al. The WU-Minn Human Connectome Project: an overview. Neuroimage 2013;80:62-79.
37. Sotiropoulos SN, Jbabdi S, Xu J, et al. Advances in diffusion MRI acquisition and processing in the Human Connectome Project. Neuroimage 2013;80:125-143.
38. Dauguet J, Peled S, Berezovskii V, et al. Comparison of fiber tracts derived from in-vivo DTI tractography with 3D histological neural tract tracer reconstruction on a macaque brain. Neuroimage 2007;37(2):530-538.
39. Leergaard TB, White NS, de Crespigny A, et al. Quantitative histological validation of diffusion MRI fiber orientation distributions in the rat brain. PloS one 2010;5(1):e8595.
40. Lawes INC, Barrick TR, Murugam V, et al. Atlas-based segmentation of white matter tracts of the human brain using diffusion tensor tractography and comparison with classical dissection. Neuroimage 2008;39(1):62-79.
41. Dyrby TB, Sogaard LV, Parker GJ, et al. Validation of in vitro probabilistic tractography. Neuroimage 2007;37(4):1267-1277.
42. Moseley ME, Cohen Y, Mintorovitch J, et al. Early Detection of Regional Cerebral-Ischemia in Cats - Comparison of Diffusion-Weighted and T2-Weighted Mri and Spectroscopy. Magnet Reson Med 1990;14(2):330-346.
43. Hjort N, Christensen S, Solling C, et al. Ischemic injury detected by diffusion imaging 11 minutes after stroke. Ann Neurol 2005;58(3):462-465.
44. Hacke W, Albers G, Al-Rawi Y, et al. The Desmoteplase In Acute Ischemic Stroke Trial (DIAS) - A phase II MRI-based 9-hour window acute stroke thrombolysis trial with intravenous desmoteplase. Stroke 2005;36(1):66-73.
45. Kidwell CS, Alger JR, Saver JL. Evolving paradigms in neuroimaging of the ischemic penumbra. Stroke 2004;35(11):2662-2665.
46. Davis SM, Donnan GA, Parsons MW, et al. Effects of alteplase beyond 3 h after stroke in the Echoplanar Imaging Thrombolytic Evaluation Trial (EPITHET): a placebo-controlled randomised trial. Lancet Neurol 2008;7(4):299-309.
47. Knight RA, Ordidge RJ, Helpern JA, Chopp M, Rodolosi LC, Peck D. Temporal Evolution of Ischemic Damage in Rat-Brain Measured by Proton Nuclear-Magnetic-Resonance Imaging. Stroke 1991;22(6):802-808.
48. Matsumoto K, Lo EH, Pierce AR, Wei HR, Garrido L, Kowall NW. Role of Vasogenic Edema and Tissue Cavitation in Ischemic Evolution on Diffusion-

Weighted Imaging - Comparison with Multiparameter Mr and Immunohistochemistry. Am J Neuroradiol 1995;16(5):1107-1115.

49. Schlaug G, Siewert B, Benfield A, Edelman RR, Warach S. Time course of the apparent diffusion coefficient (ADC) abnormality in human stroke. Neurology 1997;49(1):113-119.
50. Schwamm LH, Koroshetz WJ, Sorensen AG, et al. Time course of lesion development in patients with acute stroke: serial diffusion- and hemodynamic-weighted magnetic resonance imaging. Stroke 1998;29(11):2268-2276.
51. van Gelderen P, de Vleeschouwer MH, DesPres D, Pekar J, van Zijl PC, Moonen CT. Water diffusion and acute stroke. Magnetic resonance in medicine : official journal of the Society of Magnetic Resonance in Medicine / Society of Magnetic Resonance in Medicine 1994;31(2):154-163.
52. Duong TQ, Ackerman JJ, Ying HS, Neil JJ. Evaluation of extra- and intracellular apparent diffusion in normal and globally ischemic rat brain via 19F NMR. Magnetic resonance in medicine : official journal of the Society of Magnetic Resonance in Medicine / Society of Magnetic Resonance in Medicine 1998;40(1):1-13.
53. Neil JJ, Duong TQ, Ackerman JJ. Evaluation of intracellular diffusion in normal and globally-ischemic rat brain via 133Cs NMR. Magnetic resonance in medicine : official journal of the Society of Magnetic Resonance in Medicine / Society of Magnetic Resonance in Medicine 1996;35(3):329-335.
54. van der Toorn A, Sykova E, Dijkhuizen RM, et al. Dynamic changes in water ADC, energy metabolism, extracellular space volume, and tortuosity in neonatal rat brain during global ischemia. Magnetic resonance in medicine : official journal of the Society of Magnetic Resonance in Medicine / Society of Magnetic Resonance in Medicine 1996;36(1):52-60.
55. Mottershead JP, Schmierer K, Clemence M, et al. High field MRI correlates of myelin content and axonal density in multiple sclerosis - A post-mortem study of the spinal cord. J Neurol 2003;250(11):1293-1301.
56. Rovaris M, Gass A, Bammer R, et al. Diffusion MRI in multiple sclerosis. Neurology 2005;65(10):1526-1532.
57. Schmierer K, Wheeler-Kingshott CAM, Boulby PA, et al. Diffusion tensor imaging of post mortem multiple sclerosis brain. Neuroimage 2007;35(2):467-477.

58. Huppi PS. Cortical development in the fetus and the newborn: advanced MR techniques. Topics in magnetic resonance imaging : TMRI 2011;22(1):33-38.
59. Glenn OA, Barkovich AJ. Magnetic resonance imaging of the fetal brain and spine: an increasingly important tool in prenatal diagnosis, part 1. AJNR American journal of neuroradiology 2006;27(8):1604-1611.
60. Baldoli C, Righini A, Parazzini C, Scotti G, Triulzi F. Demonstration of acute ischemic lesions in the fetal brain by diffusion magnetic resonance imaging. Ann Neurol 2002;52(2):243-246.
61. Griffiths PD, Paley MN, Widjaja E, Taylor C, Whitby EH. In utero magnetic resonance imaging for brain and spinal abnormalities in fetuses. Bmj 2005;331(7516):562-565.
62. Clouchoux C, du Plessis AJ, Bouyssi-Kobar M, et al. Delayed cortical development in fetuses with complex congenital heart disease. Cerebral cortex 2013;23(12):2932-2943.
63. de Laveaucoupet J, Audibert F, Guis F, et al. Fetal magnetic resonance imaging (MRI) of ischemic brain injury. Prenatal diagnosis 2001;21(9):729-736.
64. Basser PJ, Mattiello J, LeBihan D. MR diffusion tensor spectroscopy and imaging. Biophysical journal 1994;66(1):259-267.
65. Le Bihan D. Looking into the functional architecture of the brain with diffusion MRI. Nat Rev Neurosci 2003;4(6):469-480.
66. Horsfield MA, Jones DK. Applications of diffusion-weighted and diffusion tensor MRI to white matter diseases - a review. Nmr Biomed 2002;15(7-8):570-577.
67. Lori NF, Akbudak E, Shimony JS, et al. Diffusion tensor fiber tracking of human brain connectivity: aquisition methods, reliability analysis and biological results. Nmr Biomed 2002;15(7-8):494-515.
68. Mori S, van Zijl PC. Fiber tracking: principles and strategies - a technical review. Nmr Biomed 2002;15(7-8):468-480.
69. Mori S, Crain BJ, Chacko VP, van Zijl PC. Three-dimensional tracking of axonal projections in the brain by magnetic resonance imaging. Ann Neurol 1999;45(2):265-269.
70. Mori S, Zhang J. Principles of diffusion tensor imaging and its applications to basic neuroscience research. Neuron 2006;51(5):527-539.

71. Mac Donald CL, Dikranian K, Bayly P, Holtzman D, Brody D. Diffusion tensor imaging reliably detects experimental traumatic axonal injury and indicates approximate time of injury. J Neurosci 2007;27(44):11869-11876.
72. Budde MD, Kim JH, Liang HF, et al. Toward accurate diagnosis of white matter pathology using diffusion tensor imaging. Magnetic resonance in medicine : official journal of the Society of Magnetic Resonance in Medicine / Society of Magnetic Resonance in Medicine 2007;57(4):688-695.
73. Wang S, Wu EX, Cai K, Lau HF, Cheung PT, Khong PL. Mild hypoxic-ischemic injury in the neonatal rat brain: longitudinal evaluation of white matter using diffusion tensor MR imaging. AJNR American journal of neuroradiology 2009;30(10):1907-1913.
74. Chahboune H, Ment LR, Stewart WB, Ma X, Rothman DL, Hyder F. Neurodevelopment of C57B/L6 mouse brain assessed by in vivo diffusion tensor imaging. Nmr Biomed 2007;20(3):375-382.
75. Baloch S, Verma R, Huang H, et al. Quantification of brain maturation and growth patterns in C57BL/6J mice via computational neuroanatomy of diffusion tensor images. Cerebral cortex 2009;19(3):675-687.
76. Ren T, Zhang J, Plachez C, Mori S, Richards LJ. Diffusion tensor magnetic resonance imaging and tract-tracing analysis of Probst bundle structure in Netrin1- and DCC-deficient mice. J Neurosci 2007;27(39):10345-10349.
77. Aggarwal M, Zhang J, Miller MI, Sidman RL, Mori S. Magnetic resonance imaging and micro-computed tomography combined atlas of developing and adult mouse brains for stereotaxic surgery. Neuroscience 2009;162(4):1339-1350.
78. Chuang N, Mori S, Yamamoto A, et al. An MRI-based atlas and database of the developing mouse brain. Neuroimage 2011;54(1):80-89.
79. Jiang Y, Johnson GA. Microscopic diffusion tensor atlas of the mouse brain. Neuroimage 2011;56(3):1235-1243.
80. Aggarwal M, Mori S, Shimogori T, Blackshaw S, Zhang J. Three-dimensional diffusion tensor microimaging for anatomical characterization of the mouse brain. Magnetic resonance in medicine : official journal of the Society of Magnetic Resonance in Medicine / Society of Magnetic Resonance in Medicine 2010;64(1):249-261.
81. Jiang Y, Johnson GA. Microscopic diffusion tensor imaging of the mouse brain. Neuroimage 2010;50(2):465-471.

82. Flint JJ, Hansen B, Fey M, et al. Cellular-level diffusion tensor microscopy and fiber tracking in mammalian nervous tissue with direct histological correlation. Neuroimage 2010;52(2):556-561.
83. Zhang J, Jones MV, McMahon MT, Mori S, Calabresi PA. In vivo and ex vivo diffusion tensor imaging of cuprizone-induced demyelination in the mouse corpus callosum. Magnetic resonance in medicine : official journal of the Society of Magnetic Resonance in Medicine / Society of Magnetic Resonance in Medicine 2011.
84. Sun SW, Liang HF, Xie M, Oyoyo U, Lee A. Fixation, not death, reduces sensitivity of DTI in detecting optic nerve damage. Neuroimage 2009;44(3):611-619.
85. Shepherd TM, Thelwall PE, Stanisz GJ, Blackband SJ. Aldehyde fixative solutions alter the water relaxation and diffusion properties of nervous tissue. Magnetic resonance in medicine : official journal of the Society of Magnetic Resonance in Medicine / Society of Magnetic Resonance in Medicine 2009;62(1):26-34.
86. Sun SW, Neil JJ, Liang HF, et al. Formalin fixation alters water diffusion coefficient magnitude but not anisotropy in infarcted brain. Magnetic resonance in medicine : official journal of the Society of Magnetic Resonance in Medicine / Society of Magnetic Resonance in Medicine 2005;53(6):1447-1451.
87. Cai Y, McMurray MS, Oguz I, et al. Use of High Resolution 3D Diffusion Tensor Imaging to Study Brain White Matter Development in Live Neonatal Rats. Front Psychiatry 2011;2:54.
88. Harsan LA, Paul D, Schnell S, et al. In vivo diffusion tensor magnetic resonance imaging and fiber tracking of the mouse brain. Nmr Biomed 2010;23(7):884-896.
89. Sun SW, Liang HF, Trinkaus K, Cross AH, Armstrong RC, Song SK. Noninvasive detection of cuprizone induced axonal damage and demyelination in the mouse corpus callosum. Magnetic resonance in medicine : official journal of the Society of Magnetic Resonance in Medicine / Society of Magnetic Resonance in Medicine 2006;55(2):302-308.
90. Baltes C, Radzwill N, Bosshard S, Marek D, Rudin M. Micro MRI of the mouse brain using a novel 400 MHz cryogenic quadrature RF probe. Nmr Biomed 2009;22(8):834-842.
91. Ratering D, Baltes C, Nordmeyer-Massner J, Marek D, Rudin M. Performance of a 200-MHz cryogenic RF probe designed for MRI and MRS of the murine brain. Magnetic resonance in medicine : official journal of the Society of Magnetic

Resonance in Medicine / Society of Magnetic Resonance in Medicine 2008;59(6):1440-1447.
92. Tannus A, Garwood M. Adiabatic pulses. Nmr Biomed 1997;10(8):423-434.
93. Mori S, van Zijl PC. A motion correction scheme by twin-echo navigation for diffusion-weighted magnetic resonance imaging with multiple RF echo acquisition. Magnetic resonance in medicine : official journal of the Society of Magnetic Resonance in Medicine / Society of Magnetic Resonance in Medicine 1998;40(4):511-516.
94. Jiang H, van Zijl PC, Kim J, Pearlson GD, Mori S. DtiStudio: resource program for diffusion tensor computation and fiber bundle tracking. Computer methods and programs in biomedicine 2006;81(2):106-116.
95. Conturo TE, Lori NF, Cull TS, et al. Tracking neuronal fiber pathways in the living human brain. Proc Natl Acad Sci USA 1999;96:10422-10427.
96. Huang H, Zhang J, van Zijl PC, Mori S. Analysis of noise effects on DTI-based tractography using the brute-force and multi-ROI approach. Magnetic resonance in medicine : official journal of the Society of Magnetic Resonance in Medicine / Society of Magnetic Resonance in Medicine 2004;52(3):559-565.
97. Kovacevic N, Henderson JT, Chan E, et al. A three-dimensional MRI atlas of the mouse brain with estimates of the average and variability. Cerebral cortex 2005;15(5):639-645.
98. Woods RP, Grafton ST, Watson JD, Sicotte NL, Mazziotta JC. Automated image registration: II. Intersubject validation of linear and nonlinear models. Journal of computer assisted tomography 1998;22(1):153-165.
99. Ceritoglu C, Oishi K, Li X, et al. Multi-contrast large deformation diffeomorphic metric mapping for diffusion tensor imaging. Neuroimage 2009;47(2):618-627.
100. Paxinos G, Franklin KBJ. The Mouse Brain in Stereotaxic Coordinates. Scan Diego: Academic Press: 2003. 120 p.
101. Paxinos G, Halliday GM, Watson C, Koutcherov Y, Wang H. Atlas of the Developing Mouse Brain at E17.5, P0 and P6. New York: Academic Press: 2006.
102. Toga AW, Thompson PM. Temporal dynamics of brain anatomy. Annual review of biomedical engineering 2003;5:119-145.
103. Wang S, Wu EX, Tam CN, Lau HF, Cheung PT, Khong PL. Characterization of white matter injury in a hypoxic-ischemic neonatal rat model by diffusion tensor MRI. Stroke 2008;39(8):2348-2353.

104. Zhang J, Richards LJ, Yarowsky P, Huang H, van Zijl PC, Mori S. Three-dimensional anatomical characterization of the developing mouse brain by diffusion tensor microimaging. Neuroimage 2003;20(3):1639-1648.
105. Lemke A, Heiler P, Stieltjes B, Neumann A, Schad L. High Resolution in Vivo DTI of the Mouse Brain: Comparison of a Cryogenic Coil with a Room Temperature Coil. The 18th annual meeting of the international society for magnetic resonance in medicine. Stockholm, Sweden; 2010. p. 1700.
106. Muller HP, Vernikouskaya I, Ludolph AC, Kassubek J, Rasche V. Fast diffusion tensor magnetic resonance imaging of the mouse brain at ultrahigh-field: aiming at cohort studies. PloS one 2012;7(12):e53389.
107. Pierpaoli C, Basser PJ. Toward a quantitative assessment of diffusion anisotropy. Magnetic resonance in medicine : official journal of the Society of Magnetic Resonance in Medicine / Society of Magnetic Resonance in Medicine 1996;36(6):893-906.
108. Farrell JA, Landman BA, Jones CK, et al. Effects of signal-to-noise ratio on the accuracy and reproducibility of diffusion tensor imaging-derived fractional anisotropy, mean diffusivity, and principal eigenvector measurements at 1.5 T. Journal of magnetic resonance imaging : JMRI 2007;26(3):756-767.
109. Badea A, Ali-Sharief AA, Johnson GA. Morphometric analysis of the C57BL/6J mouse brain. Neuroimage 2007;37(3):683-693.
110. Ma Y, Hof PR, Grant SC, et al. A three-dimensional digital atlas database of the adult C57BL/6J mouse brain by magnetic resonance microscopy. Neuroscience 2005;135(4):1203-1215.
111. Ma Y, Smith D, Hof PR, et al. In Vivo 3D Digital Atlas Database of the Adult C57BL/6J Mouse Brain by Magnetic Resonance Microscopy. Frontiers in neuroanatomy 2008;2:1.
112. Benveniste H, Kim K, Zhang L, Johnson GA. Magnetic resonance microscopy of the C57BL mouse brain. Neuroimage 2000;11(6 Pt 1):601-611.
113. Dorr AE, Lerch JP, Spring S, Kabani N, Henkelman RM. High resolution three-dimensional brain atlas using an average magnetic resonance image of 40 adult C57Bl/6J mice. Neuroimage 2008;42(1):60-69.
114. MacKenzie-Graham A, Lee EF, Dinov ID, et al. A multimodal, multidimensional atlas of the C57BL/6J mouse brain. Journal of anatomy 2004;204(2):93-102.

115. Petiet AE, Kaufman MH, Goddeeris MM, Brandenburg J, Elmore SA, Johnson GA. High-resolution magnetic resonance histology of the embryonic and neonatal mouse: a 4D atlas and morphologic database. Proc Natl Acad Sci U S A 2008;105(34):12331-12336.
116. Natt O, Watanabe T, Boretius S, Radulovic J, Frahm J, Michaelis T. High-resolution 3D MRI of mouse brain reveals small cerebral structures in vivo. Journal of neuroscience methods 2002;120(2):203-209.
117. Chan E, Kovacevic N, Ho SK, Henkelman RM, Henderson JT. Development of a high resolution three-dimensional surgical atlas of the murine head for strains 129S1/SvImJ and C57Bl/6J using magnetic resonance imaging and micro-computed tomography. Neuroscience 2007;144(2):604-615.
118. Jacobs RE, Ahrens ET, Dickinson ME, Laidlaw D. Towards a microMRI atlas of mouse development. Comput Med Imaging Graph 1999;23(1):15-24.
119. Ali AA, Dale AM, Badea A, Johnson GA. Automated segmentation of neuroanatomical structures in multispectral MR microscopy of the mouse brain. Neuroimage 2005;27(2):425-435.
120. Bock NA, Kovacevic N, Lipina TV, Roder JC, Ackerman SL, Henkelman RM. In vivo magnetic resonance imaging and semiautomated image analysis extend the brain phenotype for cdf/cdf mice. J Neurosci 2006;26(17):4455-4459.
121. Zhang J, Peng Q, Li Q, et al. Longitudinal characterization of brain atrophy of a Huntington's disease mouse model by automated morphological analyses of magnetic resonance images. Neuroimage 2010;49(3):2340-2351.
122. Lerch JP, Carroll JB, Spring S, et al. Automated deformation analysis in the YAC128 Huntington disease mouse model. Neuroimage 2008;39(1):32-39.
123. Lau JC, Lerch JP, Sled JG, Henkelman RM, Evans AC, Bedell BJ. Longitudinal neuroanatomical changes determined by deformation-based morphometry in a mouse model of Alzheimer's disease. Neuroimage 2008;42(1):19-27.
124. Sawiak SJ, Wood NI, Williams GB, Morton AJ, Carpenter TA. Voxel-based morphometry in the R6/2 transgenic mouse reveals differences between genotypes not seen with manual 2D morphometry. Neurobiol Dis 2009;33(1):20-27.
125. Tyszka JM, Readhead C, Bearer EL, Pautler RG, Jacobs RE. Statistical diffusion tensor histology reveals regional dysmyelination effects in the shiverer mouse mutant. Neuroimage 2006;29(4):1058-1065.

126. Aggarwal M, Duan W, Hou Z, et al. Spatiotemporal mapping of brain atrophy in mouse models of Huntington's disease using longitudinal in vivo magnetic resonance imaging. Neuroimage 2012;60(4):2086-2095.
127. Barazany D, Basser PJ, Assaf Y. In vivo measurement of axon diameter distribution in the corpus callosum of rat brain. Brain : a journal of neurology 2009;132(Pt 5):1210-1220.
128. Budde MD, Xie M, Cross AH, Song SK. Axial Diffusivity Is the Primary Correlate of Axonal Injury in the Experimental Autoimmune Encephalomyelitis Spinal Cord: A Quantitative Pixelwise Analysis. Journal of Neuroscience 2009;29(9):2805-2813.
129. Hansen B, Flint JJ, Heon-Lee C, et al. Diffusion tensor microscopy in human nervous tissue with quantitative correlation based on direct histological comparison. Neuroimage 2011;57(4):1458-1465.
130. Zhang JY, Aggarwal M, Mori S. Structural insights into the rodent CNS via diffusion tensor imaging. Trends Neurosci 2012;35(7):412-421.
131. Calamante F, Tournier JD, Kurniawan ND, et al. Super-resolution track-density imaging studies of mouse brain: comparison to histology. Neuroimage 2012;59(1):286-296.
132. Wu D, Xu J, McMahon MT, et al. In vivo high-resolution diffusion tensor imaging of the mouse brain. Neuroimage 2013.
133. Oshio K, Feinberg DA. Grase (Gradient-Echo and Spin-Echo) Imaging - a Novel Fast Mri Technique. Magnet Reson Med 1991;20(2):344-349.
134. Pauly J, Nishimura D, Macovski A. A linear class of large-tip-angle selective excitation pulses. Journal of Magnetic Resonance (1969) 1989;82(3):571-587.
135. Cunningham CH, Pauly JM, Nayak KS. Saturated double-angle method for rapid B1+ mapping. Magnetic resonance in medicine : official journal of the Society of Magnetic Resonance in Medicine / Society of Magnetic Resonance in Medicine 2006;55(6):1326-1333.
136. Mao J, Mareci TH, Andrew ER. Experimental-Study of Optimal Selective 180-Degrees Radiofrequency Pulses. J Magn Reson 1988;79(1):1-10.
137. Yang QX, Posse S, LeBihan D, Smith MB. Double-sampled echo-planar imaging at 3 tesla. J Magn Reson Ser B 1996;113(2):145-150.
138. van Zijl PCM, Sukumar S, Johnson MO, Webb P, Hurd RE. Optimized Shimming for High-Resolution Nmr Using 3-Dimensional Image-Based Field-Mapping. J Magn Reson Ser A 1994;111(2):203-207.

139. Schneider E, Glover G. Rapid in vivo proton shimming. Magnetic resonance in medicine : official journal of the Society of Magnetic Resonance in Medicine / Society of Magnetic Resonance in Medicine 1991;18(2):335-347.
140. Wen H, Jaffer FA. An in-Vivo Automated Shimming Method Taking into Account Shim Current Constraints. Magnet Reson Med 1995;34(6):898-904.
141. Jones DK, Horsfield MA, Simmons A. Optimal strategies for measuring diffusion in anisotropic systems by magnetic resonance imaging. Magnetic resonance in medicine : official journal of the Society of Magnetic Resonance in Medicine / Society of Magnetic Resonance in Medicine 1999;42(3):515-525.
142. Tournier JD, Calamante F, Connelly A. MRtrix: Diffusion tractography in crossing fiber regions. Int J Imag Syst Tech 2012;22(1):53-66.
143. Calamante F, Tournier JD, Heidemann RM, Anwander A, Jackson GD, Connelly A. Track density imaging (TDI): validation of super resolution property. Neuroimage 2011;56(3):1259-1266.
144. Calamante F, Tournier JD, Jackson GD, Connelly A. Track-density imaging (TDI): super-resolution white matter imaging using whole-brain track-density mapping. Neuroimage 2010;53(4):1233-1243.
145. Zhang J, van Zijl PC, Mori S. Three-dimensional diffusion tensor magnetic resonance microimaging of adult mouse brain and hippocampus. Neuroimage 2002;15(4):892-901.
146. Hiepe P, Ros C, Reichenbach JR, Herrmann KH. Diffusion Weighted ZOOM Imaging in the Lumbar Spine Based on Single-Shot STEAM. Ifmbe Proc 2009;25:670-672.
147. Jeong EK, Kim SE, Guo J, Kholmovski EG, Parker DL. High-resolution DTI with 2D interleaved multislice reduced FOV single-shot diffusion-weighted EPI (2D ss-rFOV-DWEPI). Magnetic resonance in medicine : official journal of the Society of Magnetic Resonance in Medicine / Society of Magnetic Resonance in Medicine 2005;54(6):1575-1579.
148. Finsterbusch J. Fast-spin-echo imaging of inner fields-of-view with 2D-selective RF excitations. Journal of magnetic resonance imaging : JMRI 2010;31(6):1530-1537.
149. Finsterbusch J. Functional neuroimaging of inner fields-of-view with 2D-selective RF excitations. Magnetic resonance imaging 2013.

150. Xu D, King KF, Zhu Y, McKinnon GC, Liang ZP. A noniterative method to design large-tip-angle multidimensional spatially-selective radio frequency pulses for parallel transmission. Magnetic resonance in medicine : official journal of the Society of Magnetic Resonance in Medicine / Society of Magnetic Resonance in Medicine 2007;58(2):326-334.
151. Schneider JT, Kalayciyan R, Haas M, et al. Inner-volume imaging in vivo using three-dimensional parallel spatially selective excitation. Magnetic resonance in medicine : official journal of the Society of Magnetic Resonance in Medicine / Society of Magnetic Resonance in Medicine 2012.
152. Grissom W, Yip CY, Zhang Z, Stenger VA, Fessler JA, Noll DC. Spatial domain method for the design of RF pulses in multicoil parallel excitation. Magnetic resonance in medicine : official journal of the Society of Magnetic Resonance in Medicine / Society of Magnetic Resonance in Medicine 2006;56(3):620-629.
153. Yip CY, Fessler JA, Noll DC. Iterative RF pulse design for multidimensional, small-tip-angle selective excitation. Magnetic resonance in medicine : official journal of the Society of Magnetic Resonance in Medicine / Society of Magnetic Resonance in Medicine 2005;54(4):908-917.
154. Harsan LA, David C, Reisert M, et al. Mapping remodeling of thalamocortical projections in the living reeler mouse brain by diffusion tractography. Proc Natl Acad Sci U S A 2013;110(19):E1797-1806.
155. Zhang JY, van Zijl PCM, Mori S. Image contrast using the secondary and tertiary eigenvectors in diffusion teinsor imaging. Magnet Reson Med 2006;55(2):439-449.
156. McKinstry RC, Mathur A, Miller JH, et al. Radial organization of developing preterm human cerebral cortex revealed by non-invasive water diffusion anisotropy MRI. Cerebral cortex 2002;12(12):1237-1243.
157. Heidemann RM, Porter DA, Anwander A, et al. Diffusion Imaging in Humans at 7T Using Readout-Segmented EPI and GRAPPA. Magnet Reson Med 2010;64(1):9-14.
158. McNab JA, Polimeni JR, Wang R, et al. Surface based analysis of diffusion orientation for identifying architectonic domains in the in vivo human cortex. Neuroimage 2013;69:87-100.
159. Dyrby TB, Baare WFC, Alexander DC, Jelsing J, Garde E, Sogaard LV. An Ex Vivo Imaging Pipeline for Producing High-Quality and High-Resolution Diffusion-Weighted Imaging Datasets. Hum Brain Mapp 2011;32(4):544-563.

160. Leuze CW, Anwander A, Bazin PL, et al. Layer-Specific Intracortical Connectivity Revealed with Diffusion MRI. Cerebral cortex 2012.
161. Deoni S, Jones D. Time–Series Analysis of the Diffusion Weighted Signal as a Model–Free Approach to Segmenting Tissue. ISMRM 14th Scientific Meeting & Exhibition. Seattle, Washington, USA; 2006. p. 2734.
162. Haroon HA, Binney RJ, Parker GJ. Probabilistic quantification of regional cortical microstructural complexity. Joint Annual Meeting ISMRM-ESMRMB 2010. Stockholm, Sweden; 2010.
163. Nagy Z, Alexander DC, Thomas DL, Weiskopf N, Sereno MI. Using High Angular Resolution Diffusion Imaging Data to Discriminate Cortical Regions. PloS one 2013;8(5).
164. DeFelipe J, Alonso-Nanclares L, Arellano JI. Microstructure of the neocortex: comparative aspects. Journal of neurocytology 2002;31(3-5):299-316.
165. Le Bihan D. Looking into the functional architecture of the brain with diffusion MRI. Nat Rev Neurosci 2003;4(6):469-480.
166. Basser PJ, Mattiello J, LeBihan D. MR diffusion tensor spectroscopy and imaging. Biophysical journal 1994;66(1):259-267.
167. Basser PJ, Pajevic S, Pierpaoli C, Duda J, Aldroubi A. In vivo fiber tractography using DT-MRI data. Magnet Reson Med 2000;44(4):625-632.
168. Mori S, van Zijl PCM. Fiber tracking: principles and strategies - a technical review. Nmr Biomed 2002;15(7-8):468-480.
169. Wedeen VJ, Rosene DL, Wang RP, et al. The Geometric Structure of the Brain Fiber Pathways. Science 2012;335(6076):1628-1634.
170. Toga AW, Clark KA, Thompson PM, Shattuck DW, Van Horn JD. Mapping the human connectome. Neurosurgery 2012;71(1):1-5.
171. Yassa MA, Muftuler LT, Stark CE. Ultrahigh-resolution microstructural diffusion tensor imaging reveals perforant path degradation in aged humans in vivo. Proc Natl Acad Sci U S A 2010;107(28):12687-12691.
172. Zeineh MM, Holdsworth S, Skare S, Atlas SW, Bammer R. Ultra-high resolution diffusion tensor imaging of the microscopic pathways of the medial temporal lobe. Neuroimage 2012;62(3):2065-2082.
173. Leuze CW, Anwander A, Bazin PL, et al. Layer-specific intracortical connectivity revealed with diffusion MRI. Cerebral cortex 2014;24(2):328-339.

174. Shepherd TM, Thelwall PE, Stanisz GJ, Blackband SJ. Aldehyde fixative solutions alter the water relaxation and diffusion properties of nervous tissue. Magnetic resonance in medicine : official journal of the Society of Magnetic Resonance in Medicine / Society of Magnetic Resonance in Medicine 2009;62(1):26-34.
175. Sun S-W, Liang H-F, Xie M, Oyoyo U, Lee A. Fixation, not death, reduces sensitivity of DTI in detecting optic nerve damage. Neuroimage 2009;44(3):611-619.
176. Wu D, Xu J, McMahon MT, et al. In vivo high-resolution diffusion tensor imaging of the mouse brain. NeuroImage 2013;83:18-26.
177. Eichenbaum H, Schoenbaum G, Young B, Bunsey M. Functional organization of the hippocampal memory system. Proc Natl Acad Sci U S A 1996;93(24):13500-13507.
178. Strange BA, Witter MP, Lein ES, Moser EI. Functional organization of the hippocampal longitudinal axis. Nat Rev Neurosci 2014;15(10):655-669.
179. Witter MP. Hippocampus. In: Watson C, Paxinos G, Puelles L, editors. The mouse nervous system: Academic Press; 2011. p. 112-139.
180. Tonegawa S, Nakazawa K, Wilson MA. Genetic neuroscience of mammalian learning and memory. Philosophical transactions of the Royal Society of London Series B, Biological sciences 2003;358(1432):787-795.
181. Treves A, Tashiro A, Witter MP, Moser EI. What is the mammalian dentate gyrus good for? Neuroscience 2008;154(4):1155-1172.
182. Witter MP. The perforant path: projections from the entorhinal cortex to the dentate gyrus. Progress in brain research 2007;163:43-61.
183. Witter MP. Intrinsic and extrinsic wiring of CA3: indications for connectional heterogeneity. Learning & memory 2007;14(11):705-713.
184. Witter MP, Groenewegen HJ, Lopes da Silva FH, Lohman AH. Functional organization of the extrinsic and intrinsic circuitry of the parahippocampal region. Progress in neurobiology 1989;33(3):161-253.
185. van Strien NM, Cappaert NL, Witter MP. The anatomy of memory: an interactive overview of the parahippocampal-hippocampal network. Nat Rev Neurosci 2009;10(4):272-282.
186. Squire LR, Stark CEL, Clark RE. The medial temporal lobe. Annu Rev Neurosci 2004;27:279-306.

187. Oh SW, Harris JA, Ng L, et al. A mesoscale connectome of the mouse brain. Nature 2014;508(7495):207-+.
188. Wu D, Reisinger D, Xu JD, et al. Localized diffusion magnetic resonance micro-imaging of the live mouse brain. Neuroimage 2014;91:12-20.
189. Jones DK, Knosche TR, Turner R. White matter integrity, fiber count, and other fallacies: the do's and don'ts of diffusion MRI. Neuroimage 2013;73:239-254.
190. Ragan T, Kadiri LR, Venkataraju KU, et al. Serial two-photon tomography for automated ex vivo mouse brain imaging. Nat Methods 2012;9(3):255-U248.
191. Goldowitz D. Allen Reference Atlas. A Digital Color Brain Atlas of the C57BL/6J Male Mouse - by H. W. Dong. Genes, Brain and Behavior 2010;9(1):128-128.
192. Choe AS, Stepniewska I, Colvin DC, Ding Z, Anderson AW. Validation of diffusion tensor MRI in the central nervous system using light microscopy: quantitative comparison of fiber properties. Nmr Biomed 2012;25(7):900-908.
193. Dyrby TB, Sogaard LV, Parker GJ, et al. Validation of in vitro probabilistic tractography. Neuroimage 2007;37(4):1267-1277.
194. Palop JJ, Chin J, Roberson ED, et al. Aberrant excitatory neuronal activity and compensatory remodeling of inhibitory hippocampal circuits in mouse models of Alzheimer's disease. Neuron 2007;55(5):697-711.
195. Zhang J, Yarowsky P, Gordon MN, et al. Detection of amyloid plaques in mouse models of Alzheimer's disease by magnetic resonance imaging. Magnet Reson Med 2004;51(3):452-457.
196. Riban V, Bouilleret V, Pham-Le BT, Fritschy JM, Marescaux C, Depaulis A. Evolution of hippocampal epileptic activity during the development of hippocampal sclerosis in a mouse model of temporal lobe epilepsy. Neuroscience 2002;112(1):101-111.
197. Aggarwal M, Mori S, Shimogori T, Blackshaw S, Zhang JY. Three-Dimensional Diffusion Tensor Microimaging for Anatomical Characterization of the Mouse Brain. Magnet Reson Med 2010;64(1):249-261.
198. Jbabdi S, Johansen-Berg H. Tractography: where do we go from here? Brain Connect 2011;1(3):169-183.
199. Dammann O, Leviton A. Inflammatory brain damage in preterm newborns--dry numbers, wet lab, and causal inferences. Early Hum Dev 2004;79(1):1-15.
200. Sévely A, Manelfe C. Magnetic resonance imaging of the fetal brain. In: Rutherfod M, editor. MRI of the Neonatal Brain. New York: Saunders Ltd.; 2001.

201. Basser PJ, Pierpaoli C. Microstructural and physiological features of tissues elucidated by quantitative-diffusion-tensor MRI. Journal of magnetic resonance Series B 1996;111(3):209-219.
202. Beaulieu C. The basis of anisotropic water diffusion in the nervous system - a technical review. NMR in biomedicine 2002;15(7-8):435-455.
203. Huang H, Xue R, Zhang J, et al. Anatomical characterization of human fetal brain development with diffusion tensor magnetic resonance imaging. J Neurosci 2009;29(13):4263-4273.
204. Takahashi E, Folkerth RD, Galaburda AM, Grant PE. Emerging cerebral connectivity in the human fetal brain: an MR tractography study. Cerebral cortex 2012;22(2):455-464.
205. van den Heuvel MP, Kersbergen KJ, de Reus MA, et al. The Neonatal Connectome During Preterm Brain Development. Cerebral cortex 2014.
206. Bui T, Daire JL, Chalard F, et al. Microstructural development of human brain assessed in utero by diffusion tensor imaging. Pediatric radiology 2006;36(11):1133-1140.
207. Kim DH, Chung S, Vigneron DB, Barkovich AJ, Glenn OA. Diffusion-weighted imaging of the fetal brain in vivo. Magnetic resonance in medicine : official journal of the Society of Magnetic Resonance in Medicine / Society of Magnetic Resonance in Medicine 2008;59(1):216-220.
208. Righini A, Bianchini E, Parazzini C, et al. Apparent diffusion coefficient determination in normal fetal brain: a prenatal MR imaging study. AJNR American journal of neuroradiology 2003;24(5):799-804.
209. Zanin E, Ranjeva JP, Confort-Gouny S, et al. White matter maturation of normal human fetal brain. An in vivo diffusion tensor tractography study. Brain and behavior 2011;1(2):95-108.
210. Kasprian G, Brugger PC, Weber M, et al. In utero tractography of fetal white matter development. Neuroimage 2008;43(2):213-224.
211. Dhenain M, Ruffins SW, Jacobs RE. Three-dimensional digital mouse atlas using high-resolution MRI. Dev Biol 2001;232(2):458-470.
212. Aggarwal M, Mori S, Shimogori T, Blackshaw S, Zhang J. Three-dimensional diffusion tensor microimaging for anatomical characterization of the mouse brain. Magn Reson Med 2010;64(1):249-261.

213. Shepherd TM, Thelwall PE, Stanisz GJ, Blackband SJ. Aldehyde Fixative Solutions Alter the Water Relaxation and Diffusion Properties of Nervous Tissue. Magn Reson Med 2009;62(1):26-34.
214. Sun SW, Neil JJ, Liang HF, et al. Formalin fixation alters water diffusion coefficient magnitude but not anisotropy in infarcted brain. Magnet Reson Med 2005;53(6):1447-1451.
215. Sun SW, Liang HF, Le TQ, Armstrong RC, Cross AH, Song SK. Differential sensitivity of in vivo and ex vivo diffusion tensor imaging to evolving optic nerve injury in mice with retinal ischemia. Neuroimage 2006;32(3):1195-1204.
216. Wu D, Martin LJ, Northington FJ, Zhang J. Oscillating gradient diffusion MRI reveals unique microstructural information in normal and hypoxia-ischemia injured mouse brains. Magnetic resonance in medicine : official journal of the Society of Magnetic Resonance in Medicine / Society of Magnetic Resonance in Medicine 2014.
217. Berrios-Otero CA, Nieman BJ, Parasoglou P, Turnbull DH. In utero phenotyping of mouse embryonic vasculature with MRI. Magnetic resonance in medicine : official journal of the Society of Magnetic Resonance in Medicine / Society of Magnetic Resonance in Medicine 2012;67(1):251-257.
218. Parasoglou P, Berrios-Otero CA, Nieman BJ, Turnbull DH. High-resolution MRI of early-stage mouse embryos. Nmr Biomed 2013;26(2):224-231.
219. Schneider JT, Kalayciyan R, Haas M, et al. Inner-volume imaging in vivo using three-dimensional parallel spatially selective excitation. Magnet Reson Med 2013;69(5):1367-1378.
220. Finsterbusch J. Fast-Spin-Echo Imaging of Inner Fields-of-View With 2D-Selective RF Excitations. Journal of Magnetic Resonance Imaging 2010;31(6):1530-1537.
221. Pauly J, Nishimura D, Macovski A. A Linear Class of Large-Tip-Angle Selective Excitation Pulses. J Magn Reson 1989;82(3):571-587.
222. Burd I, Bentz AI, Chai J, et al. Inflammation-induced preterm birth alters neuronal morphology in the mouse fetal brain. Journal of neuroscience research 2010;88(9):1872-1881.
223. Burd I, Balakrishnan B, Kannan S. Models of fetal brain injury, intrauterine inflammation, and preterm birth. American journal of reproductive immunology 2012;67(4):287-294.

224. Dada T, Rosenzweig JM, Al Shammary M, et al. Mouse model of intrauterine inflammation: sex-specific differences in long-term neurologic and immune sequelae. Brain, behavior, and immunity 2014;38:142-150.
225. Mori S, van Zijl PC. A motion correction scheme by twin-echo navigation for diffusion-weighted magnetic resonance imaging with multiple RF echo acquisition. Magn Reson Med 1998;40(4):511-516.
226. Jones DK, Leemans A. Diffusion Tensor Imaging. Methods Mol Biol 2011;711:127-144.
227. Andrews W, Liapi A, Plachez C, et al. Robo1 regulates the development of major axon tracts and interneuron migration in the forebrain. Development 2006;133(11):2243-2252.
228. Novak Z, Thurmond AS, Ross PL, Jones MK, Thornburg KL, Katzberg RW. Gadolinium-DTPA transplacental transfer and distribution in fetal tissue in rabbits. Investigative radiology 1993;28(9):828-830.
229. Frank LR. Anisotropy in high angular resolution diffusion-weighted MRI. Magnetic resonance in medicine : official journal of the Society of Magnetic Resonance in Medicine / Society of Magnetic Resonance in Medicine 2001;45(6):935-939.
230. Tuch DS, Reese TG, Wiegell MR, Wedeen VJ. Diffusion MRI of complex neural architecture. Neuron 2003;40(5):885-895.
231. Wedeen VJ, Hagmann P, Tseng WY, Reese TG, Weisskoff RM. Mapping complex tissue architecture with diffusion spectrum magnetic resonance imaging. Magnetic resonance in medicine : official journal of the Society of Magnetic Resonance in Medicine / Society of Magnetic Resonance in Medicine 2005;54(6):1377-1386.
232. Stepisnik J. Time-Dependent Self-Diffusion by Nmr Spin-Echo. Physica B 1993;183(4):343-350.
233. Helmer KG, Dardzinski BJ, Sotak CH. The application of porous-media theory to the investigation of time-dependent diffusion in in vivo systems. Nmr Biomed 1995;8(7-8):297-306.
234. Niendorf T, Norris DG, Leibfritz D. Detection of Apparent Restricted Diffusion in Healthy Rat-Brain at Short Diffusion Times. Magnet Reson Med 1994;32(5):672-677.
235. Moonen CTW, Pekar J, Devleeschouwer MHM, Vangelderen P, Vanzijl PCM, Despres D. Restricted and Anisotropic Displacement of Water in Healthy Cat Brain

and in Stroke Studied by Nmr Diffusion Imaging. Magnet Reson Med 1991;19(2):327-332.

236. Clark CA, Hedehus M, Moseley ME. Diffusion time dependence of the apparent diffusion tensor in healthy human brain and white matter disease. Magnet Reson Med 2001;45(6):1126-1129.
237. Parsons EC, Jr., Does MD, Gore JC. Temporal diffusion spectroscopy: theory and implementation in restricted systems using oscillating gradients. Magnetic resonance in medicine : official journal of the Society of Magnetic Resonance in Medicine / Society of Magnetic Resonance in Medicine 2006;55(1):75-84.
238. Gore JC, Xu J, Colvin DC, Yankeelov TE, Parsons EC, Does MD. Characterization of tissue structure at varying length scales using temporal diffusion spectroscopy. Nmr Biomed 2010;23(7):745-756.
239. Schachter M, Does MD, Anderson AW, Gore JC. Measurements of restricted diffusion using an oscillating gradient spin-echo sequence. J Magn Reson 2000;147(2):232-237.
240. Parsons EC, Does MD, Gore JC. Modified oscillating gradient pulses for direct sampling of the diffusion spectrum suitable for imaging sequences. Magnetic resonance imaging 2003;21(3-4):279-285.
241. Xu J, Does MD, Gore JC. Dependence of temporal diffusion spectra on microstructural properties of biological tissues. Magnetic resonance imaging 2011;29(3):380-390.
242. Xu J, Does MD, Gore JC. Quantitative characterization of tissue microstructure with temporal diffusion spectroscopy. J Magn Reson 2009;200(2):189-197.
243. Xu J, Does MD, Gore JC. Sensitivity of MR diffusion measurements to variations in intracellular structure: effects of nuclear size. Magnetic resonance in medicine : official journal of the Society of Magnetic Resonance in Medicine / Society of Magnetic Resonance in Medicine 2009;61(4):828-833.
244. Novikov DS, Kiselev VG. Surface-to-volume ratio with oscillating gradients. J Magn Reson 2011;210(1):141-145.
245. Portnoy S, Fichtner ND, Dziegielewski C, Stanisz MP, Stanisz GJ. In vitro detection of apoptosis using oscillating and pulsed gradient diffusion magnetic resonance imaging. Nmr Biomed 2014:n/a-n/a.

246. Colvin DC, Yankeelov TE, Does MD, Yue Z, Quarles C, Gore JC. New insights into tumor microstructure using temporal diffusion spectroscopy. Cancer Res 2008;68(14):5941-5947.
247. Aggarwal M, Jones MV, Calabresi PA, Mori S, Zhang J. Probing mouse brain microstructure using oscillating gradient diffusion MRI. Magnetic resonance in medicine : official journal of the Society of Magnetic Resonance in Medicine / Society of Magnetic Resonance in Medicine 2012;67(1):98-109.
248. Kershaw J, Leuze C, Aoki I, et al. Systematic changes to the apparent diffusion tensor of in vivo rat brain measured with an oscillating-gradient spin-echo sequence. Neuroimage 2013;70:10-20.
249. Portnoy S, Flint JJ, Blackband SJ, Stanisz GJ. Oscillating and pulsed gradient diffusion magnetic resonance microscopy over an extended b-value range: implications for the characterization of tissue microstructure. Magnetic resonance in medicine : official journal of the Society of Magnetic Resonance in Medicine / Society of Magnetic Resonance in Medicine 2013;69(4):1131-1145.
250. Pyatigorskaya N, Le Bihan D, Reynaud O, Ciobanu L. Relationship between the diffusion time and the diffusion MRI signal observed at 17.2 tesla in the healthy rat brain cortex. Magnet Reson Med 2013:n/a-n/a.
251. Lundell H, Sonderby CK, Dyrby TB. Diffusion weighted imaging with circularly polarized oscillating gradients. Magnetic resonance in medicine : official journal of the Society of Magnetic Resonance in Medicine / Society of Magnetic Resonance in Medicine 2014.
252. Xu J, Li K, Smith RA, et al. Characterizing tumor response to chemotherapy at various length scales using temporal diffusion spectroscopy. PloS one 2012;7(7):e41714.
253. Aggarwal M, Burnsed J, Martin LJ, Northington FJ, Zhang J. Imaging neurodegeneration in the mouse hippocampus after neonatal hypoxia-ischemia using oscillating gradient diffusion MRI. Magnetic resonance in medicine : official journal of the Society of Magnetic Resonance in Medicine / Society of Magnetic Resonance in Medicine 2013.
254. Baron CA, Beaulieu C. Oscillating Gradient Spin-Echo (OGSE) diffusion tensor imaging of the human brain. Magnetic resonance in medicine : official journal of the Society of Magnetic Resonance in Medicine / Society of Magnetic Resonance in Medicine 2013.

255. Van AT, Holdsworth SJ, Bammer R. In vivo investigation of restricted diffusion in the human brain with optimized oscillating diffusion gradient encoding. Magnetic resonance in medicine : official journal of the Society of Magnetic Resonance in Medicine / Society of Magnetic Resonance in Medicine 2013.
256. Martin LJ, Brambrink AM, Lehmann C, et al. Hypoxia-ischemia causes abnormalities in glutamate transporters and death of astroglia and neurons in newborn striatum. Ann Neurol 1997;42(3):335-348.
257. Northington FJ, Ferriero DM, Graham EM, Traystman RJ, Martin LJ. Early Neurodegeneration after Hypoxia-Ischemia in Neonatal Rat Is Necrosis while Delayed Neuronal Death Is Apoptosis. Neurobiol Dis 2001;8(2):207-219.
258. Vannucci RC, Vannucci SJ. Perinatal hypoxic-ischemic brain damage: evolution of an animal model. Developmental neuroscience 2005;27(2-4):81-86.
259. Sotak CH. The role of diffusion tensor imaging in the evaluation of ischemic brain injury - a review. Nmr Biomed 2002;15(7-8):561-569.
260. Sizonenko SV, Camm EJ, Garbow JR, et al. Developmental changes and injury induced disruption of the radial organization of the cortex in the immature rat brain revealed by in vivo diffusion tensor MRI. Cerebral cortex 2007;17(11):2609-2617.
261. Chan KC, Khong PL, Lau HF, Cheung PT, Wu EX. Late measures of microstructural alterations in severe neonatal hypoxic-ischemic encephalopathy by MR diffusion tensor imaging. International journal of developmental neuroscience : the official journal of the International Society for Developmental Neuroscience 2009;27(6):607-615.
262. Rice JE, 3rd, Vannucci RC, Brierley JB. The influence of immaturity on hypoxic-ischemic brain damage in the rat. Ann Neurol 1981;9(2):131-141.
263. Ditelberg JS, Sheldon RA, Epstein CJ, Ferriero DM. Brain injury after perinatal hypoxia-ischemia is exacerbated in copper/zinc superoxide dismutase transgenic mice. Pediatr Res 1996;39(2):204-208.
264. Baltes C, Radzwill N, Bosshard S, Marek D, Rudin M. Micro MRI of the mouse brain using a novel 400 MHz cryogenic quadrature RF probe. NMR in biomedicine 2009;22(8):834-842.
265. Simpson JH, Carr HY. Diffusion and Nuclear Spin Relaxation in Water. Phys Rev 1958;111(5):1201-1202.
266. Wyatt KD, Tanapat P, Wang SSH. Speed limits in the cerebellum: constraints from myelinated and unmyelinated parallel fibers. Eur J Neurosci 2005;21(8):2285-2290.

267. Sillitoe RV, Fu Y, Watson C. Cerebellum. In: Watson C, Paxinos G, Puelles L, editors. The Mouse Nervous System. New York: Academic Press; 2012. p. 360-397.
268. Grawford GNC, Barer R. The action of Formaldehyde on living cells as studied by phase-contrast microscopy. Quarterly Journal of Microscopical Science 1951;92(4):403-452.
269. Baron CA, Kate M, Gioia LC, et al. Oscillating Gradient Spin-Echo (OGSE) DTI Yields Mechanistic Insights in Human Stroke. Proc Intl Soc Mag Reson Med 22 (2014): 0106. Milano, Italy; 2014.
270. van der Toorn A, Dijkhuizen RM, Tulleken CA, Nicolay K. Diffusion of metabolites in normal and ischemic rat brain measured by localized 1H MRS. Magnetic resonance in medicine : official journal of the Society of Magnetic Resonance in Medicine / Society of Magnetic Resonance in Medicine 1996;36(6):914-922.
271. Wick M, Nagatomo Y, Prielmeier F, Frahm J. Alteration of intracellular metabolite diffusion in rat brain in vivo during ischemia and reperfusion. Stroke 1995;26(10):1930-1933; discussion 1934.
272. Ackerman JJH, Neil JJ. The use of MR-detectable reporter molecules and ions to evaluate diffusion in normal and ischemic brain. Nmr Biomed 2010;23(7):725-733.
273. Qiao M, Malisza KL, Del Bigio MR, Tuor UI. Transient hypoxia-ischemia in rats: changes in diffusion-sensitive MR imaging findings, extracellular space, and Na+-K+ -adenosine triphosphatase and cytochrome oxidase activity. Radiology 2002;223(1):65-75.
274. Towfighi J, Mauger D, Vannucci RC, Vannucci SJ. Influence of age on the cerebral lesions in an immature rat model of cerebral hypoxia-ischemia: A light microscopic study. Dev Brain Res 1997;100(2):149-160.
275. Scafidi J, Fagel DM, Ment LR, Vaccarino FM. Modeling premature brain injury and recovery. International journal of developmental neuroscience : the official journal of the International Society for Developmental Neuroscience 2009;27(8):863-871.
276. Charriaut-Marlangue C, Bonnin P, Leger PL, Renolleau S. Brief update on hemodynamic responses in animal models of neonatal stroke and hypoxia-ischemia. Exp Neurol 2013;248:316-320.

277. Vannucci SJ, Hagberg H. Hypoxia-ischemia in the immature brain. J Exp Biol 2004;207(18):3149-3154.
278. Dijkhuizen RM, Knollema S, van der Worp HB, et al. Dynamics of cerebral tissue injury and perfusion after temporary hypoxia-ischemia in the rat: evidence for region-specific sensitivity and delayed damage. Stroke 1998;29(3):695-704.
279. Sizonenko SV, Sirimanne E, Mayall Y, Gluckman PD, Inder T, Williams C. Selective cortical alteration after hypoxic-ischemic injury in the very immature rat brain. Pediatr Res 2003;54(2):263-269.
280. McQuillen PS, Ferriero DM. Selective vulnerability in the developing central nervous system. Pediatric neurology 2004;30(4):227-235.
281. Martin LJ, Brambrink AM, Lehmann C, et al. Hypoxia-ischemia causes abnormalities in glutamate transporters and death of astroglia and neurons in newborn striatum. Ann Neurol 1997;42(3):335-348.
282. Northington FJ, Ferriero DM, Flock DL, Martin LJ. Delayed neurodegeneration in neonatal rat thalamus after hypoxia-ischemia is apoptosis. J Neurosci 2001;21(6):1931-1938.
283. Back SA, Han BH, Luo NL, et al. Selective vulnerability of late oligodendrocyte progenitors to hypoxia-ischemia. Journal of Neuroscience 2002;22(2):455-463.
284. Ness JK, Romanko MJ, Rothstein RP, Wood TL, Levison SW. Perinatal hypoxia-ischemia induces apoptotic and excitotoxic death of periventricular white matter oligodendrocyte progenitors. Developmental neuroscience 2001;23(3):203-208.
285. Northington FJ, Chavez-Valdez R, Martin LJ. Neuronal Cell Death in Neonatal Hypoxia-Ischemia. Ann Neurol 2011;69(5):743-758.
286. Blomgren K, Hagberg H. Free radicals, mitochondria, and hypoxia–ischemia in the developing brain. Free Radical Bio Med 2006;40(3):388-397.
287. Stoll G, Jander S, Schroeter M. Inflammation and glial responses in ischemic brain lesions. Progress in neurobiology 1998;56(2):149-171.
288. Lorek A, Takei Y, Cady EB, et al. Delayed (Secondary) Cerebral Energy Failure after Acute Hypoxia-Ischemia in the Newborn Piglet - Continuous 48-Hour Studies by Phosphorus Magnetic-Resonance Spectroscopy. Pediatr Res 1994;36(6):699-706.
289. Rumpel H, Nedelcu J, Aguzzi A, Martin E. Late glial swelling after acute cerebral hypoxia-ischemia in the neonatal rat: A combined magnetic resonance and histochemical study. Pediatr Res 1997;42(1):54-59.

290. Swanson RA, Farrell K, Stein BK. Astrocyte energetics, function, and death under conditions of incomplete ischemia: A mechanism of glial death in the penumbra. Glia 1997;21(1):142-153.
291. Chen YM, Swanson RA. Astrocytes and brain injury. J Cerebr Blood F Met 2003;23(2):137-149.
292. Rosenberg AA, Parks JK, Murdaugh E, Parker WD, Jr. Mitochondrial function after asphyxia in newborn lambs. Stroke 1989;20(5):674-679.
293. Budd SL. Mechanisms of neuronal damage in brain hypoxia/ischemia: Focus on the role of mitochondrial calcium accumulation. Pharmacol Therapeut 1998;80(2):203-229.
294. Puka-Sundvall M, Wallin C, Gilland E, et al. Impairment of mitochondrial respiration after cerebral hypoxia-ischemia in immature rats: relationship to activation of caspase-3 and neuronal injury. Brain research Developmental brain research 2000;125(1-2):43-50.
295. Qiao M, Meng SZ, Scobie K, Foniok T, Tuor UI. Magnetic resonance imaging of differential gray versus white matter injury following a mild or moderate hypoxic-ischemic insult in neonatal rats. Neurosci Lett 2004;368(3):332-336.
296. Lodygensky GA, West T, Moravec MD, et al. Diffusion characteristics associated with neuronal injury and glial activation following hypoxia-ischemia in the immature brain. Magnetic resonance in medicine : official journal of the Society of Magnetic Resonance in Medicine / Society of Magnetic Resonance in Medicine 2011;66(3):839-845.
297. Dunn OJ. Multiple Comparisons Among Means. Journal of the American Statistical Association 1961;56(293):52-64.
298. Lodygensky GA, West T, Moravec MD, et al. Diffusion Characteristics Associated With Neuronal Injury and Glial Activation Following Hypoxia-Ischemia in the Immature Brain. Magnet Reson Med 2011;66(3):839-845.
299. Meng S, Qiao M, Scobie K, Tomanek B, Tuor UI. Evolution of magnetic resonance imaging changes associated with cerebral hypoxia-ischemia and a relatively selective white matter injury in neonatal rats. Pediatr Res 2006;59(4 Pt 1):554-559.
300. Han BH, Xu DG, Choi JJ, et al. Selective, reversible caspase-3 inhibitor is neuroprotective and reveals distinct pathways of cell death after neonatal hypoxic-ischemic brain injury. J Biol Chem 2002;277(33):30128-30136.

301. Siow B, Drobnjak I, Ianus A, Christie IN, Lythgoe MF, Alexander DC. Axon radius estimation with oscillating gradient spin echo (OGSE) diffusion MRI. Diffus Fundam Org 2013;18:1-6.
302. Xu JZ, Li H, Harkins KD, et al. Mapping mean axon diameter and axonal volume fraction by MRI using temporal diffusion spectroscopy. Neuroimage 2014;103:10-19.
303. Le Bihan D, Breton E, Lallemand D, Grenier P, Cabanis E, Laval-Jeantet M. MR imaging of intravoxel incoherent motions: application to diffusion and perfusion in neurologic disorders. Radiology 1986;161(2):401-407.
304. Le Bihan D, Breton E, Lallemand D, Aubin ML, Vignaud J, Laval-Jeantet M. Separation of diffusion and perfusion in intravoxel incoherent motion MR imaging. Radiology 1988;168(2):497-505.
305. Le Bihan D, Douek P, Argyropoulou M, Turner R, Patronas N, Fulham M. Diffusion and perfusion magnetic resonance imaging in brain tumors. Topics in magnetic resonance imaging : TMRI 1993;5(1):25-31.
306. Le Bihan D. Intravoxel incoherent motion perfusion MR imaging: a wake-up call. Radiology 2008;249(3):748-752.
307. Iima M, Reynaud O, Tsurugizawa T, et al. Characterization of Glioma Microcirculation and Tissue Features Using Intravoxel Incoherent Motion Magnetic Resonance Imaging in a Rat Brain Model. Investigative radiology 2014;49(7):485-490.
308. Novikov DS, Jensen JH, Helpern JA, Fieremans E. Revealing mesoscopic structural universality with diffusion. Proc Natl Acad Sci U S A 2014;111(14):5088-5093.

Curriculum Vitae

Dan Wu February 18th, 2015

Educational History

Ph.D. 2015 Biomdical Engineering Johns Hopkins University School of Medicine (Mentor: Zhang, Jiangyang PhD)

M.S. 2011 Biomdical Engineering Johns Hopkins University School of Medicine

B.S. 2009 Biomedical Engineering Zhejiang University

Other Professional Experiences

Internship 2011 Infinite Biomedical Technologies, Baltimore, MD

Teaching Assistant 2012-2013 Johns Hopkins University

Scholarships and fellowships

Howard and Hughes Medical Instituite International Student Fellowship 2014-2015

Andrew and Elvira Bozzelli Fellowship 2009-2010

Academic and other honors

2014 Hairball Award MRI division, Department of Radiology, Johns Hopkins University School of Medicine

2014 Diffusion Study Group 1st place Poster Award International society of Magnetic Resonance in Medicine

2013 Summa Cum Laude Merit Award International society of Magnetic Resonance in Medicine

2013 Diffusion MRI workshop Travel Award International society of Magnetic Resonance in Medicine

2011 Neural Engineering Travel Award IEEE Engineering in Medicine & Biology Soceity

Publications, peer reviewed

Xu J, Qin Q, **Wu D**, Jun H, Song X, MacMahon MT, Northington FJ, Zhang J, van Zijl PCM, Pekar JJ (2015). An interleaved labeling and imaging scheme for non-invasive perfusion imaging. Magnetic Resonance in Medicine.

Wu D, Lei J, Rosenzweig JM, Burd I, Zhang J (2014). In utero localized diffusion MRI of the embryonic mouse brain microstructure and injury. Journal of Magnetic Resonance Imaging.

Wu D, Martin LJ, Northington FJ, Zhang J (2014). Oscillating gradient diffusion MRI reveals unique microstructural information in the normal and hypoxia-ischemia injured mouse brains. Magnetic Resonance in Medicine 72(5):1366-74.

Wu D, Reisinger D, Xu J, Fatemi SA, van Zijl PCM, Mori S, Zhang J (2014). Localized diffusion magnetic resonance micro-imaging of the live mouse brain. Neuroimage 91:12-20.

Wu D, Xu J, McMahon MT, van Zijl PCM, Mori S, Northington FJ, Zhang J (2013). *In vivo* high-resolution diffusion tensor imaging of the mouse brain. Neuroimage 83:19-26.

Madhok J, **Wu D**, Xiong W, Geocadin R, Jia X (2012). Hypothermia amplifies somatosensory-evoked potentials in uninjured rats. Journal of Neurosurgical Anesthesiology 24(3):197-202

Wu D, Xiong W, Jia X, Geocadin R, Thakor NV (2011). Effects of hypothermia on short- and long-latency somatosensory neuronal responses following hypoxic-ischemic brain injury. Journal of Neurophysiology 107(4):1164-71

Wu D, Anastassios B, Xiong W, Madhok J, Jia X, Thakor NV (2010). Study of the origins of short- and long-latency SSEP during recovery from brain ischemia in a rat model. Neuroscience Letters 485(3):157-61

Wu D, Feng Z, Wang J (2010). A Novel Denoising Approach to Multi-channel Spike Signals Recorded by Microelectrode Array. Journal of Zhejiang University (Engineering Science) 2010-01

Conference Proceedings and Abstracts

Wu D, Gobius I, Richards LJ, Mori S, Zhang J (2014). High resolution HARDI of early embryonic mouse brain development. Joint Annual Meeting ISMRM-ESMRMB, Milan, Italy, May 2014.

Wu D, Martin LJ, Northington FJ, Zhang J (2014). *In vivo* oscillating gradient diffusion MRI provides unique microstructural information in normal and hypoxic-ischemic injured mouse brains. Joint Annual Meeting ISMRM-ESMRMB, Milan, Italy, May 2014.

Wu D, Lei J, Rosenzweig JM, Burd I, Zhang J (2014). In utero localized diffusion MRI of the embryonic mouse brain microstructure and injury. Annual Meeting of the Society of Neuroscience, Washington DC, Nov 2014.

Wu D, Martin LJ, Frances FJ, Zhang, J (2014). Microstructural insights into neonatal hypoxia-ischemia by oscillating gradient diffusion MRI. Hershey Conference on Developmental Brain Injury, Stl Michaels, MD June, 2014.

Wu D, Xu J, Mori S, Zhang J (2013). Mapping hippocampal connectivity of the live mouse brain with localized high resolution HARDI. ISMRM Workshop on Diffusion MRI, Podstrana, Croatia, Oct 2013.

Wu D, Reisinger D, Xu J, van Zijl PCM, Mori S, Zhang J (2013). Localized *in vivo* high resolution HARDI reveals complex microstructure in the mouse brain. ISMRM Annual Meeting, Salt Lake City, UT, April 2013.

Wu D, Xu J, McMahon MT, van Zijl PCM, Mori S, Zhang J (2012). *In vivo* high resolution diffusion tensor imaging of the mouse brain using a cryogenic probe at 11.7 T. ISMRM Annual Meeting, Melbrourne, Victoria, Austrailia, May 2012.

Wu D, Bezerianos A, Sherman D, Jia X, Thakor NV (2011). Causal Inferences from Thalamic and Cortical LFPs following Hypoxic-ischemic Brain Injury. IEEE/EMBS Conference on Neural Engineering, Cancun, Mexico, April 2011.

Wu D, Bezerianos A, Zhang H, Jia X, NV Thakor (2010). Exploring high-frequency oscillation as a marker of brain ischemia using S-transform. IEEE Engineering in Medicine and Biology Society (EMBC), Buenos Aires, Argentina, Sep 2010.

Wu D, Modhok J, Choi Y, **Jia X**, Thakor NV (2010). Discovery of Long-latency Somatosensory Evoked Potentials as a marker of Cardiac Arrest Induced Brain Injury. Southern Biomedical Engineering Conference (SBEC), College Park, MD, May 2010.

Service and Leadership

2014 Director of Professional Development in Extramural Development in Graduate Education (EDGE), Johns Hopkins Biomedical Engineering

2013 Director of Engagement in Extramural Development in Graduate Education (EDGE), Johns Hopkins Biomedical Engineering

2012 Committee member in Hopkins Imaging Initiative (HII), Johns Hopkins

2011 Committee member in Chinese Student and Scholar Association, Johns Hopkins